Graph Theory and Dynamic Programming Framework for Automated Segmentation of Ophthalmic Imaging Biomarkers

by

Stephanie Ja-Yi Chiu

Department of Biomedical Engineering
Duke University

Date: _____

Approved:

_____
Sina Farsiu, Supervisor

_____
Joseph A. Izatt

_____
Cynthia A. Toth

_____
Adam P. Wax

_____
Gregg E. Trahey

Dissertation submitted in partial fulfillment of the requirements for the degree of
Doctor of Philosophy in the Department of Biomedical Engineering
in the Graduate School of Duke University

2014

Abstract

Graph Theory and Dynamic Programming Framework for Automated Segmentation of Ophthalmic Imaging Biomarkers

by

Stephanie Ja-Yi Chiu

Department of Biomedical Engineering
Duke University

Date: _____

Approved:

_____
Sina Farsiu, Supervisor

_____
Joseph A. Izatt

_____
Cynthia A. Toth

_____
Adam P. Wax

_____
Gregg E. Trahey

An abstract of a dissertation submitted in partial fulfillment of the requirements for the degree of Doctor of Philosophy in the Department of Biomedical Engineering in the Graduate School of Duke University

2014

Abstract

Accurate quantification of anatomical and pathological structures in the eye is crucial for the study and diagnosis of potentially blinding diseases. Earlier and faster detection of ophthalmic imaging biomarkers also leads to optimal treatment and improved vision recovery. While modern optical imaging technologies such as optical coherence tomography (OCT) and adaptive optics (AO) have facilitated *in vivo* visualization of the eye at the cellular scale, the massive influx of data generated by these systems is often too large to be fully analyzed by ophthalmic experts without extensive time or resources. Furthermore, manual evaluation of images is inherently subjective and prone to human error.

This dissertation describes the development and validation of a framework called *graph theory and dynamic programming* (GTDP) to automatically detect and quantify ophthalmic imaging biomarkers. The GTDP framework was validated as an accurate technique for segmenting retinal layers on OCT images. The framework was then extended through the development of the *quasi-polar transform* to segment closed-contour structures including photoreceptors on AO scanning laser ophthalmoscopy images and retinal pigment epithelial cells on confocal microscopy images.

The GTDP framework was next applied in a clinical setting with pathologic images that are often lower in quality. Algorithms were developed to delineate morphological structures on OCT indicative of diseases such as age-related macular degeneration (AMD) and diabetic macular edema (DME). The AMD algorithm

was shown to be robust to poor image quality and was capable of segmenting both drusen and geographic atrophy. To account for the complex manifestations of DME, a novel kernel regression-based classification framework was developed to identify retinal layers and fluid-filled regions as a guide for GTDP segmentation.

The development of fast and accurate segmentation algorithms based on the GTDP framework has significantly reduced the time and resources necessary to conduct large-scale, multi-center clinical trials. This is one step closer towards the long-term goal of improving vision outcomes for ocular disease patients through personalized therapy.

Contents

List of Tables

List of Figures

List of Abbreviations and Symbols

Abbreviations

1D	One-dimensional
2D	Two-dimensional
3D	Three-dimensional
A2A	Age-related Eye Disease Study 2 Ancillary
AMD	Age-related macular degeneration
AO	Adaptive optics
AOSLO	Adaptive optics scanning laser ophthalmoscope
AREDS	Age-related Eye Disease Study
BM	Bruch's membrane
CI	Confidence interval
cRT	Cirrus-based retinal thickness
CSJ	Choroid-scleral junction
CV	Coefficient of variation
DARSI	Duke Advanced Research in SD-OCT Imaging
DEDUCE	Duke Enterprise Data Unified Content Explorer
DME	Diabetic macular edema
DOCTRAP	Duke's Optical Coherence Tomography Retinal Analysis Program
DR	Diabetic retinopathy

ETDRS	Early Treatment Diabetic Retinopathy Study
FN	False negative
FP	False positive
FWHM	Full width at half maximum
GA	Geographic atrophy
GCL	Ganglion cell layer
GTDP	Graph theory and dynamic programming
ICC	Intra-class correlation coefficient
ILM	Inner limiting membrane
INL	Inner nuclear layer
IPL	Inner plexiform layer
IRB	Institutional review board
IS	Inner segment
ISE	Inner segment ellipsoid
ISM	Inner segment myeloid
LoA	Limits of agreement
NEI	National Eye Institute
NFL	Nerve fiber layer
NSR	Neurosensory retina
OCT	Optical coherence tomography
ONL	Outer nuclear layer
OPL	Outer plexiform layer
OS	Outer segment
PD	Paired difference
PS-OCT	Polarization-sensitive optical coherence tomography
RPE	Retinal pigment epithelium

RPEDC	Retinal pigment epithelium and drusen complex
SD	Standard deviation
SD-OCT	Spectral domain optical coherence tomography
SE	Standard error
SFFS	Sequential forward feature selection
SNR	Signal-to-noise ratio
sRT	Spectralis-based retinal thickness
sRV	Spectralis-based retinal volume
SVP	Summed voxel projection
TP	True positive
TR	Total retina
TRT	Total retinal thickness
TRV	Total retinal volume
VEGF	Vascular endothelial growth factor

Symbols

$\circ$	Hadamard product
$\vee$	Element-wise logical OR operator
$\bigtriangledown$	Gradient operator
$\lfloor \cdot \rceil$	Nearest integer function, also denoted by nint$(\cdot)$ or round$(\cdot)$
$\boldsymbol{a}$	Set of possible weight values for a classification feature
a_k	k^{th} possible weight value for a classification feature
A	Total number of possible weights a_k
$\boldsymbol{A}$	Adjacency matrix of a graph
$\boldsymbol{b}$	Vector for kernel regression containing β_0, $\boldsymbol{\beta}_1$, and $\boldsymbol{\beta}_2$
$\hat{\boldsymbol{b}}$	Estimate of $\boldsymbol{b}$

$\boldsymbol{b}_{pk}$	k^{th} column in $\boldsymbol{B}_p$
$\boldsymbol{b}_{qk}$	k^{th} column in $\boldsymbol{B}_q$
$\boldsymbol{B}_c$	Cropped binary image in the Cartesian domain of a single pilot estimate
$\boldsymbol{B}_c^{full}$	Full binary image in the Cartesian domain containing all pilot estimates
$\boldsymbol{B}_p$	Polar transformed image of $\boldsymbol{B}_c$
$\boldsymbol{B}_q$	Quasi-polar transformed image of $\boldsymbol{B}_c$
β_0	Zeroth derivative of the kernel regression function; the noiseless image
$\hat{\beta}_0$	Estimate of β_0
$\boldsymbol{\beta}_1$	First derivative of the kernel regression function; the noiseless gradient image
$\boldsymbol{\beta}_2$	Second derivative of the kernel regression function; the noiseless second derivative image
c	True class of pixel $\boldsymbol{z}$
$\hat{c}$	Estimated class of pixel $\boldsymbol{z}$ using the classifier $\phi(\boldsymbol{z})$
c_n^{ab}	Value of the classifier boundary image between classes a and b at node n
c_t	True class of $\boldsymbol{v}_t$ and $\boldsymbol{v}_t'$
$\boldsymbol{C}$	Set of all possible classes for classification
$\boldsymbol{C}'$	Subset of classes to be evaluated using the criterion function
C_k	k^{th} class in $\boldsymbol{C}$ for classification
$\boldsymbol{C}_k$	k^{th} flattening matrix for the quasi-polar transform
$\boldsymbol{C}_k^{inv}$	k^{th} inverse flattening matrix for the inverse quasi-polar transform
d_{ab}	Euclidean distance from node a to b
$\boldsymbol{D}_{\hat{\boldsymbol{K}}}$	Diagonal matrix for kernel regression containing $\hat{\boldsymbol{K}}(\boldsymbol{z}_p - \boldsymbol{z})$
$E(\cdot)$	Criterion function to be minimized during feature selection

$\boldsymbol{E}_c^{full}$	Full binary edge image in the Cartesian domain containing all feature segmentations
$f(\boldsymbol{z})$	Local regression function at $\boldsymbol{z}$; the noiseless image intensity
$\hat{f}(\boldsymbol{z})$	Estimate of $f(\boldsymbol{z})$
$f_p[\theta]$	A discrete function specifying the boundary of the pilot estimate in $\boldsymbol{B}_p$
$f_q[\theta]$	A discrete function specifying the segmented boundary of the structure in $\boldsymbol{I}_q$
F	Height in pixels of $\boldsymbol{I}_c$ and $\boldsymbol{B}_c$
$\boldsymbol{F}_c$	Filtered image in the Cartesian domain
$\overline{\boldsymbol{F}}_c$	Mean of $\boldsymbol{F}_c$
$\boldsymbol{F}_{Ln}$	n^{th} Laws texture energy filter
$\boldsymbol{F}_{mean}$	Mean filter
g_n^{DL}	Value of $\boldsymbol{G}^{DL}$ at node n
g_n^{LD}	Value of $\boldsymbol{G}^{LD}$ at node n
G	Width in pixels of $\boldsymbol{I}_c$ and $\boldsymbol{B}_c$
$\boldsymbol{G}^{DL}$	Dark-light vertical gradient of $\boldsymbol{I}$ or $\boldsymbol{I}_q$
$\boldsymbol{G}_i$	Vertical gradient image estimate for the Gaussian steering kernel
$\boldsymbol{G}_j$	Horizontal gradient image estimate for the Gaussian steering kernel
$\boldsymbol{G}^{LD}$	Light-dark vertical gradient of $\boldsymbol{I}$ or $\boldsymbol{I}_q$
γ	Scaling parameter for the Gaussian steering kernel
h	Global smoothing parameter for the Gaussian steering kernel
h_i	Vertical smoothing parameter for the classic Gaussian kernel
h_j	Horizontal smoothing parameter for the classic Gaussian kernel
$\mathcal{H}$	Hessian matrix
$\boldsymbol{H}$	High-pass filtered image

i	i^{th} row of an image or matrix
i_n	Value of $\boldsymbol{I}$ or $\boldsymbol{I}_q$ at node n
i_p	Row of $\boldsymbol{z}_p$
i_{ref}	Row of $\boldsymbol{z}_{ref}$
$\boldsymbol{I}, \boldsymbol{I}_c^{full}, \boldsymbol{I}_c^{orig}$	Full image in the Cartesian domain containing all features to segment
$\hat{\boldsymbol{I}}$	Denoised image estimate of $\boldsymbol{I}$
$\boldsymbol{I}_c$	Cropped image in the Cartesian domain of a single feature to segment
$\boldsymbol{I}_{max}$	Maximum intensity in $\boldsymbol{I}_c$
$\boldsymbol{I}_p$	Polar transformed image of $\boldsymbol{I}_c$
$\boldsymbol{I}_q$	Quasi-polar transformed image of $\boldsymbol{I}_c$
j	j^{th} column of an image or matrix
$\boldsymbol{j}_k$	Column in $\boldsymbol{J}_k$
j_p	Column of $\boldsymbol{z}_p$
j_{ref}	Column of $\boldsymbol{z}_{ref}$
$\boldsymbol{J}_k$	k^{th} cost for calculating RPE cell segmentation weights
$\boldsymbol{J}_{total}$	Toal cost for calculating RPE cell segmentation weights
K	Total number of pixels in the pilot estimate of the feature to segment for the quasi-polar transform
K	Total number of classes for classification
$\boldsymbol{K}$	Kernel used to weight the importance of nearby points during regression analysis
$\hat{\boldsymbol{K}}$	Normalized kernel $\boldsymbol{K}$
$\boldsymbol{K}_{iGS}$	Iterative adaptive Gaussian steering kernel
$\hat{\boldsymbol{K}}_{iGS}$	Normalized iterative adaptive Gaussian steering kernel
$\boldsymbol{K}_G$	Classic Gaussian kernel

$\boldsymbol{K}_{GS}$	Adaptive Gaussian steering kernel
L	Number of features in the feature vector $\boldsymbol{v}$
L'	Number of features in the feature vector subset $\boldsymbol{v}'$
$\text{LinNorm}(\boldsymbol{x}, \alpha, \beta)$	Linear normalization of the values in $\boldsymbol{x}$ to range from α to β
λ'	Elongation regularization parameter for the Gaussian steering kernel
λ''	Scaling regularization parameter for the Gaussian steering kernel
$\boldsymbol{\Lambda}$	Elongation matrix for the Gaussian steering kernel
M	Height in pixels of $\boldsymbol{I}$, $\boldsymbol{I}_c^{full}$, and $\boldsymbol{B}_c^{full}$
$\boldsymbol{\mu}$	Set of $\boldsymbol{\mu}_k$ for all classes C_k
$\boldsymbol{\mu}_k$	Mean of the training feature vectors for class C_k
n	Pixel connectivity; the number of connected neighbors
n	Number of images in the training dataset for classification
n_p	Zero-mean independent and identically distributed noise for $\boldsymbol{z}_p$
N	Width in pixels of $\boldsymbol{I}$, $\boldsymbol{I}_c^{full}$, and $\boldsymbol{B}_c^{full}$
N_{FN}	Number of false negatives
N_{FP}	Number of false positives
N_{TN}	Number of true negatives
N_{TP}	Number of true positives
$\boldsymbol{p}_\theta$	A discrete function of the shortest path found with endpoints initialized to $r' = f_q[\theta]$
P	Number of pixels in the kernel
$\phi(\boldsymbol{z})$	Classifier which estimates the class $\hat{c}$ of a pixel $\boldsymbol{z}$
r	Distance from $\boldsymbol{z}$ to $\boldsymbol{z}_{ref}$ in the Cartesian domain, which also corresponds to the vertical axis in the polar domain
r'	Vertical axis in the quasi-polar domain
r'_n	Distance of node n from the top of $\boldsymbol{I}_q$ (ie. row value)

R	Height in pixels of $\boldsymbol{I}_p, \boldsymbol{B}_p, \boldsymbol{I}_q,$ and$\boldsymbol{B}_q$
s_1	Larger singular value
s_2	Smaller singular value
$\boldsymbol{s}_{pk}$	k^{th} column in $\boldsymbol{S}_p$
$\boldsymbol{s}_{qk}$	k^{th} column in $\boldsymbol{S}_q$
$\boldsymbol{S}$	Singular value decomposition diagonal matrix
$\boldsymbol{S}_c$	Image of $\boldsymbol{S}_q$ transformed into the Cartesian domain
$\boldsymbol{S}_p$	Image of $\boldsymbol{S}_q$ transformed into the polar domain
$\boldsymbol{S}_q$	Image of the segmentation $f_q[\theta]$ in the quasi-polar domain
σ	Elongation paramter for the Gaussian steering kernel
$\boldsymbol{\sigma}_k^{inv}$	Reciprocal of the standard deviation of the training feature vectors for class C_k
$\boldsymbol{\Sigma}$	Covariance matrix for the Gaussian steering kernel
t	Threshold value
$\boldsymbol{t}_q$	Column in $\boldsymbol{T}_q$
T	Total number of training pixels for classification
$\boldsymbol{T}_c$	Threshold image in the Cartesian domain
T_k	Number of training pixels with a true class $c = C_k$
$\boldsymbol{T}_q$	Quasi-polar transformed image of $\boldsymbol{T}_c$
θ	Angle between $\overrightarrow{\boldsymbol{z}_{ref}\boldsymbol{z}}$ and the reference axis, which also corresponds to the horizontal axis in the polar and quasi-polar domains
θ	Rotation parameter for the Gaussian steering kernel
Θ	Width in pixels of $\boldsymbol{I}_p$, $\boldsymbol{B}_p$, $\boldsymbol{I}_q$, and $\boldsymbol{B}_q$
$\boldsymbol{\Theta}$	Rotation matrix for the Gaussian steering kernel
$\boldsymbol{U}$	Singular value decomposition left rotation matrix
v	Feature in $\boldsymbol{v}$ for classification

$\boldsymbol{v}$	Feature vector for classification
$\boldsymbol{v}'$	Feature vector with reduced dimensionality from feature selection
v_n	n^{th} feature
$\boldsymbol{v}_t$	t^{th} feature vector in $\boldsymbol{V}$
$\boldsymbol{v}'_t$	t^{th} feature vector in $\boldsymbol{V}'$
$\boldsymbol{V}$	Singular value decomposition right rotation matrix
$\boldsymbol{V}$	A set of training feature vectors
$\boldsymbol{V}'$	A set of training feature vectors with reduced dimensionality from feature selection
$\hat{\boldsymbol{V}}$	A set of normalized training feature vectors
$\hat{\boldsymbol{V}}'$	A set of normalized training feature vectors with reduced dimensionality from feature selection
$\hat{\boldsymbol{V}}_A$	A set of normalized and weighted training feature vectors
$V_{between}$	Variance in measurements taken between subjects
V_{ij}	i^{th} row and j^{th} column in $\boldsymbol{V}$
$\boldsymbol{V}_k$	A set of training feature vectors with a true class $c = C_k$
$\boldsymbol{V}_l$	l^{th} column in $\boldsymbol{V}$
$\hat{\boldsymbol{V}}_l$	l^{th} column in $\hat{\boldsymbol{V}}$
V_{total}	Total variance $V_{within} + V_{between}$
V_{within}	Variance in measurements taken on the same subject
$\text{vec}(\boldsymbol{M})$	Vectorization of a matrix $\boldsymbol{M}$
$\text{vech}(\boldsymbol{M})$	Half-vectorization of a symmetric matrix $\boldsymbol{M}$
$\boldsymbol{\omega}$	Set of feature weights for classification
ω_{ab}	Weight of the edge connecting nodes a and b
ω_{end}	Weight for all edges connected to the end node
ω_l	l^{th} feature weight for classification

ω_{min}	Minimal non-zero edge weight
ω_{start}	Weight for all edges connected to the start node
$\boldsymbol{X}$	Matrix for kernel regression containing pixel distances to the second order
$\boldsymbol{y}$	Vector for kernel regression containing noisy pixel intensities y_p
y_p	Intensity of the p^{th} pixel on a noisy image
$\hat{y_p}$	Estimate of y_p
$\boldsymbol{z}$	Pixel location $[i, j]$ on an image
$\boldsymbol{z}_k$	k^{th} pixel in an image, in a pilot estimate, or on a segmentation path
$\boldsymbol{z}_p$	p^{th} pixel in a kernel
$\boldsymbol{z}_{ref}$	Reference (e.g. central) pixel location on $\boldsymbol{B}_c$ and $\boldsymbol{I}_c$ for the polar transform

Acknowledgements

I would like to thank all of my committee members, collaborators, and peers for their contributions to the work in this dissertation. I would especially like to thank my advisor and continuous advocate, Sina Farsiu, for his dedicated mentorship, expertise in the field, and guidance in life. I would also like to thank my co-advisors Joseph Izatt and Cynthia Toth for their wisdom and for making my research truly translational. Finally, I would like to thank my friends and family for their companionship and support throughout graduate school, making the past five years not only educational, but a fun and loving experience as well.

1

Introduction

1.1 Ophthalmic Imaging and Biomarkers

The retina plays an especially important role in vision, as it is responsible for the capture and transmission of light from the outside world to the brain [1]. It is structurally layered in morphology, and abnormal retinal layer thicknesses are often indicative of ocular diseases such as age-related macular degeneration (AMD) and diabetic macular edema (DME) [2]. As a result, early and accurate detection of such ocular imaging biomarkers can lead to optimal treatment and improved vision recovery [3].

Until recently, retinal layer thickness information was unavailable to ophthalmologists since the gold standards for *in vivo* imaging of the eye were color fundus photography and fluorescein angiography [4]. Both imaging modalities only provide a two-dimensional (2D) *en face* view of the eye, making it difficult for clinicians to accurately assess disease severity. With the development of novel imaging technologies such as optical coherence tomography (OCT), ophthalmologists are now able to capture three-dimensional (3D) *in vivo* images of the eye at micron-scale resolutions [5].

In particular, spectral domain OCT (SD-OCT) is a Fourier domain OCT acquisition method whose higher speed, resolution, and signal-to-noise ratio (SNR) compared to the original time domain OCT system has allowed for a more widespread and detailed monitoring of retinal and corneal layer thicknesses [6, 7].

In addition to layer thickness measurements, there are also many useful imaging biomarkers in the form of closed-contour shapes. For example, retinal cysts on OCT often appear ellipsoidal [8, 9], and retinal pigment epithelial (RPE) cells on confocal fluorescence microscopy images are hexagonal [10]. Adaptive optics (AO) is a technology whose recent integration into ophthalmic imaging systems has enabled *in vivo* visualization of individual human photoreceptors [11–25]. These structures appear circular on AO scanning laser ophthalmoscope (AOSLO) images, and with the level of resolution gains achieved by AO optical systems, researchers have begun to individually track photoreceptors since their characteristics can provide considerable insight into the pathological state of the eye for many retinal diseases including rod-cone dystrophy [26–39].

1.2 Clinical and Research Need for Automated Segmentation

As ophthalmic imaging technologies advance, the amount of data generated by these systems is often too large to be fully analyzed by experts without extensive time or resources. For example, 3D OCT imaging of the eye is achieved by capturing a raster scan of depth-resolved data (A-scans) to build a 2D cross-sectional image (B-scan); a series of adjacent B-scans are then acquired to generate a 3D volume (Figure 1.1). In clinical studies, a single volumetric retinal SD-OCT acquisition of an eye can be around 512 pixels $\times$ 1000 A-scans $\times$ 100 B-scans in size, where the number of B-scans varies based on the desired trade-off between individual B-scan resolution versus scan density.

To then quantitatively analyze specific OCT retinal layer thicknesses, an expert

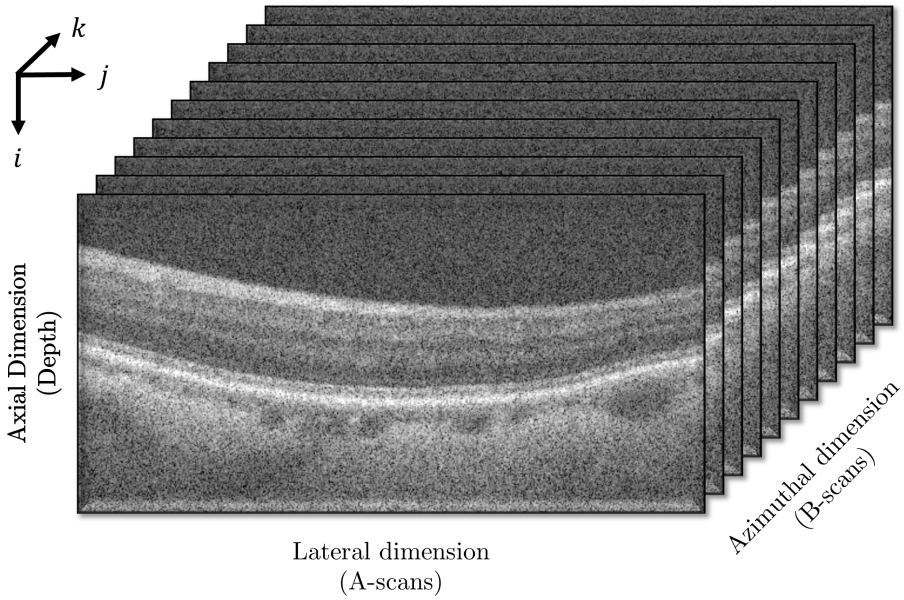

FIGURE 1.1: Dimensions of an OCT volume.

must manually mark every layer boundary on each B-scan (Figure 1.2). Moreover, the inherent subjectivity associated with manual marking leads to intra-subject and inter-subject variability. By developing robust segmentation algorithms to automatically delineate these layers boundaries, clinicians may be able to earlier detect and thus improve the vision outcomes of patients with ocular diseases.

While some commercial OCT systems are equipped with automated segmentation algorithms, they are mainly targeted at measuring the thickness of the total retina (TR) [42]. However, since clinicians need to assess individual layers for layer-specific diseases such as AMD or DME, measurements often need to be obtained manually or semi-automatically. Furthermore, segmentation errors are common in the presence of image artifacts or pathology, thus careful review is necessary to correct for such errors [43]. As a result, considerable work has been done in the past decade to automate the segmentation of ocular layered structures.

Prior to the framework developed in this dissertation, only a handful of algorithms had been developed to segment ocular layers on OCT [44–55]. Column-wise

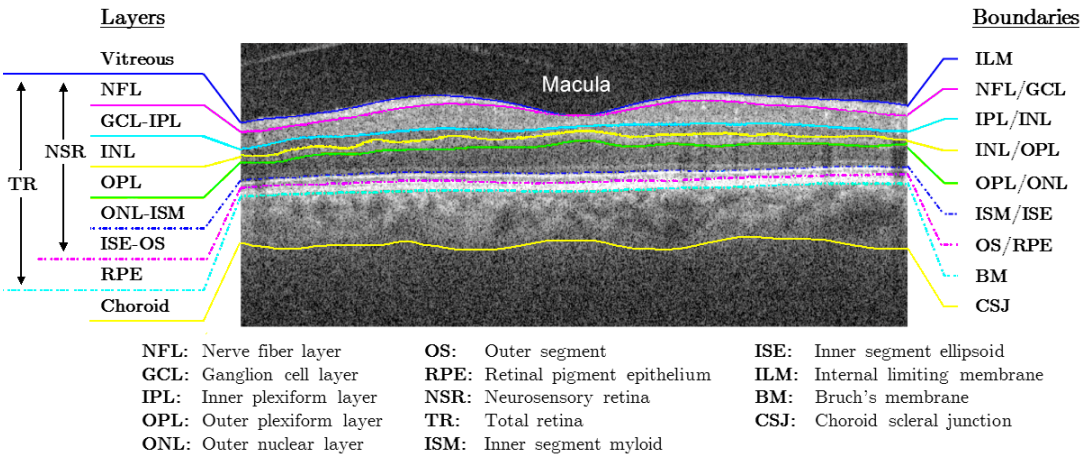

FIGURE 1.2: Manual segmentation of retinal layer boundaries on an SD-OCT B-scan of the retina centered at the macula. *Left:* Target retinal layers. *Right:* Target retinal layer boundaries. Note that the inner segment ellipsoid (ISE) was previously called the inner segment / outer segment (IS/OS) junction, however correlations of OCT to histology suggest that the hyper-reflective band is instead the ISE [40, 41].

intensity profiling was used to distinguish layer boundaries in a one-dimensional (1D) fashion, where Ishikawa *et al.* additionally implemented mean filtering techniques for de-speckling [44] and Fernández *et al.* proposed a combined structure tensor and complex diffusion filtering methodology for image denoising. Active contours were another method explored by Yazdanpanah *et al.* for layer segmentation of rodent images [50] and by Farsiu *et al.* for the segmentation of drusen [47]. Mishra *et al.* then extended the traditional active contour with a two-step kernel-based optimization scheme [54]. Finally, Haeker *et al.* and Garvin *et al.* utilized graph cuts to segment radial scans of the retina in a 3D fashion [46, 48, 53], while Lee *et al.* applied multi-scale 3D graph cuts to segment the optic nerve head [55]. In just the past few years since these works, many new algorithms have been developed to segment retinal [42, 56–73], choroidal [74–83], optic nerve [84], and corneal [85, 86] layer boundaries with now an emphasis on quantifying various disease states or validating repeatability and reproducibility metrics.

In comparison to layered structures, the quantification of closed-contour features is even more challenging since imaging systems are not equipped with the image analysis software necessary to evaluate these types of biomarkers. Furthermore, unlike retinal layers which have only a limited number of boundaries, closed-contour structures such as photoreceptors and RPE cells are seen hundreds of times within a single image. Manual analysis of such features is insurmountable for large-scale studies, thus hindering researchers from efficiently analyzing the data necessary to fully understand the pathogenesis behind many ocular diseases. As a result, algorithms have been developed in recent years to identify retinal features including fluid, detachments, and macular holes on OCT [87–96], AMD markers on fundus photographs [97–99] and OCT [47], vessel lumens [100], photoreceptors on AO images [22, 25, 87, 101–105], and corneal cells [106–110].

This dissertation presents a conceptually simple segmentation approach that is adaptable across many applications and capable of achieving accurate results. This novel method, called *graph theory and dynamic programming* (GTDP), leverages graph theory and shortest path algorithms to effectively segment both layer and closed-contour boundaries [56, 87].

2

Graph Theory and Dynamic Programming Framework

2.1 GTDP for Layer Segmentation

The segmentation of layered structures such as the retina on OCT is crucial for the diagnosis and study of ocular diseases. We therefore developed a generalized framework for segmenting layered structures called *graph theory and dynamic programming*, or GTDP [56]. Figure 2.1 outlines the core steps in our layer segmentation algorithm, and the steps are detailed in the following subsections. Applications of the GTDP layer segmentation framework can be found in Chapters 3, 5, 7, and 9.

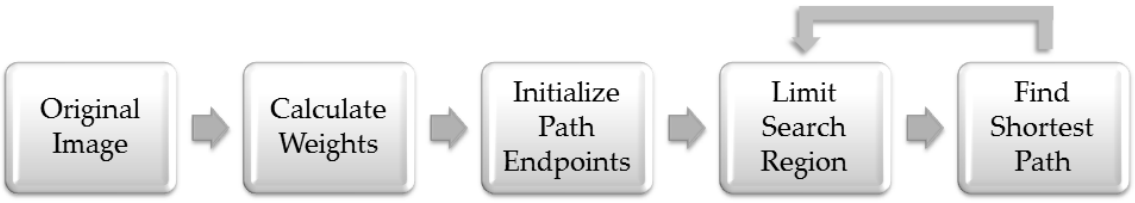

FIGURE 2.1: Flowchart of the GTDP framework for layer segmentation.

2.1.1 Graph representation and weight calculation

We represent each image (e.g. an OCT B-scan) as a graph of *nodes*, where each node corresponds to an image pixel and links connecting the nodes are called *edges* [111]. A set of connected edges then form a pathway to travel across the graph. Weights can be assigned to individual edges to create path preferences, and edge directions can limit path mobility. To travel across the graph from a start node to an end node, the preferred path is the route in which the total weight sum is at a minimum. This resulting path is the boundary which delineates one region from another. For our problem, boundaries between retinal layers correspond to the preferred paths on an OCT B-scan.

Figure 2.2A shows an example graph containing three connected nodes. Illustrated in Figure 2.2 is Node 1's preference for Node 3 due to its lower edge weight compared to Node 2. Furthermore, the arrow indicates path directionality, preventing travel from Node 3 to Node 1. Once appropriate weights are assigned to the edges, an *adjacency matrix* [111] is generated specifying the edge weight for every node pair permutation (Figure 2.2B). Computationally efficient techniques such as Dijkstra's algorithm [112] can then be used to find the shortest path from a given start to end node (See Section 2.1.4). For Dijkstra's algorithm, weights must be non-negative and a weight of zero indicates an unconnected node pair.

For an image $\boldsymbol{I} \in \mathbb{R}^{M \times N}$ (M rows by N columns in size) containing features with relatively smooth transitions between neighboring pixels, we link each node to its eight nearest neighbors (a connectivity of $n = 8$). We keep all other node pairs disconnected, resulting in a sparse adjacency matrix $\{\boldsymbol{A} \in \mathbb{R}^{MN \times MN} \mid \boldsymbol{A} \geqslant 0\}$ with MNn filled entries for a directed graph, or $MNn/2$ entries for an undirected graph since $\boldsymbol{A}$ is then symmetric and either the upper or lower triangle can be ignored.

To then accurately segment a graph, the key is to assign the appropriate edge

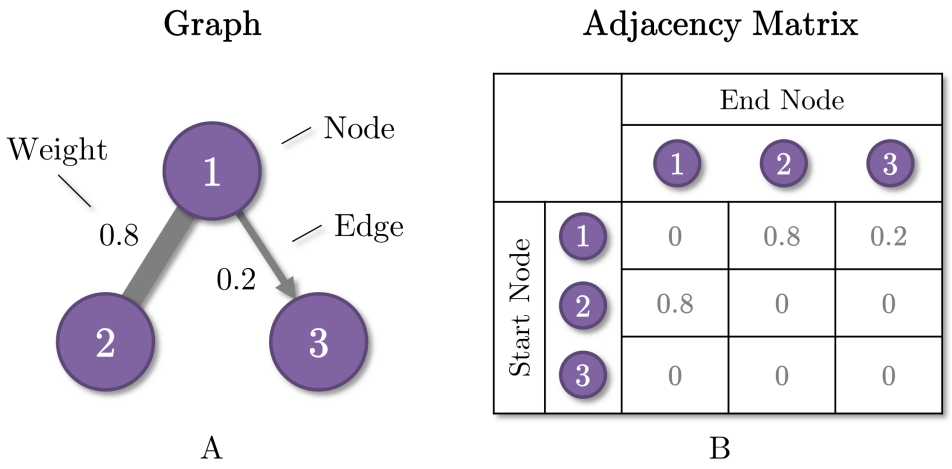

FIGURE 2.2: (A) A directional graph with three connected nodes, and (B) the adjacency matrix corresponding to A specifying edge weights.

weights. Common metrics for varying weight values include functions of distances between pixels or differences between intensity values [113]. As long as the feature to be segmented has characteristics unique to its surroundings, low weights can be assigned to the borders of that feature to distinguish it from the rest of the image.

2.1.2 Automatic endpoint initialization

Finding the shortest path of a layered structure on a graph requires knowledge of the layer's start and end nodes. While estimation of these endpoints is possible, the process is further complicated when the graph contains many layered structures (e.g. the retina). In this section, we present two automatic initialization methods that bypass the need for manual or ad hoc endpoint selection.

For the first initialization method, we generate a graph that maintains the Cartesian coordinate system. The first step is to add an additional column to either side of the image with arbitrary intensity values. Since minimum-weighted paths are preferred, the vertical edge weights in these added columns are set to a minimum value (ω_{min}), thus negating the arbitrarily assigned intensities. Note that ω_{min} should be

significantly smaller than any of the non-zero weights in the adjacency matrix of the original graph. In doing so, the nodes in the newly added columns maintain their connectivity, and the path is able to traverse in the vertical direction of these columns with minimal resistance. This allows for the start and end nodes to be assigned arbitrarily within the newly added columns, since the path will travel freely along these columns prior to moving across the image in the minimum-weighted path. Once the image is segmented, the two additional columns can be removed, leaving an accurate segmentation without endpoint initialization error.

Figure 2.3A is an example image segmented using the first automatic initialization technique. Two vertical columns are added to either side of the image with arbitrary values (here, the maximum intensity) and minimal undirected vertical edge weights (Figure 2.3B, blue). The start and end nodes are then initialized to the top left and bottom right corners, respectively (Figure 2.3A, purple). In this example, the edges are assigned weights as a function of pixel intensity, where darker pixels result in a lower weight. The pink line represents the resulting segmentation using Dijkstra's algorithm. The newly added columns can then be removed, showing an accurate segmentation despite arbitrary endpoint assignments.

The second automatic method for initialization is shown in Figure 2.3C-D and involves the addition of a single start and end node on either side of the image instead of two full columns. Directed edges (or undirected, as the result will not differ) with weights ω_{start} and ω_{end} are then used to connect the start and end nodes to each pixel on the leftmost and rightmost columns of the image, respectively. Since this method no longer conforms to the Cartesian grid and the "distance" from the added node to every pixel in the column is effectively equal, the values for ω_{start} and ω_{end} may be set arbitrarily. While this initialization method no longer has a 1:1 mapping between every pixel and node, it is simpler and slightly faster as it requires fewer nodes. Other than these difference, the edge weights and directions within the valid

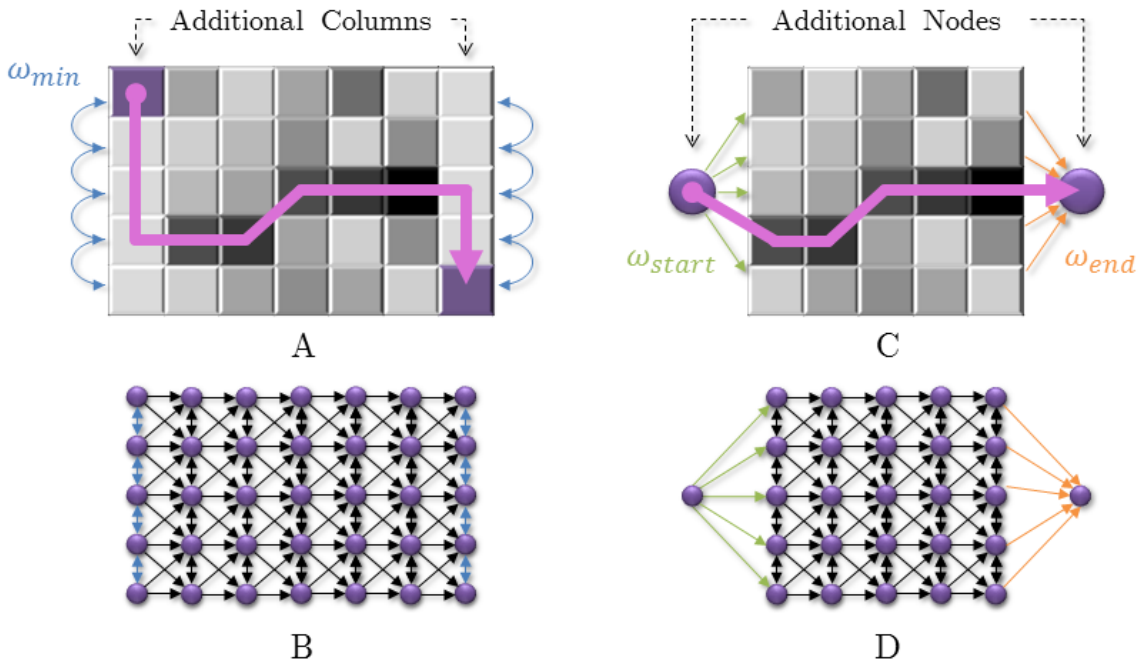

FIGURE 2.3: Two methods for automatic endpoint initialization and their resulting segmentations (pink). (A) Cartesian method where additional columns are added to either side of the image with minimal undirected vertical edge weights, and (B) an example graph of A. (C) Single node method where a node is added to either side of the graph with the same weight for every edge extending from the node, and (D) an example graph of C.

image region are equivalent (Figures 2.3B,D, black).

2.1.3 Search Region Limitation

If a graph contains extraneous structures that are similar to the feature of interest, then the incorrect feature may accidentally be segmented (e.g. the IPL and OPL layers of the retina are of similar intensity and location). To prevent the algorithm from erroneously segmenting these structures in place of the target feature, it is helpful to limit the graph to a valid search space that excludes any undesired features. This may be achieved by setting the weights of all edges within the invalid regions to zero. For example, if the IPL/INL layer boundary is already accurately segmented, then we can set the weights for all edges above the IPL/INL to zero when searching

for the OPL/ONL layer boundary. In practice, determining regions which are invalid can be complex and often relies on prior knowledge about the image and its features.

2.1.4 Finding the Minimum-Weighted Path

Given a graph with computed edge weights (Figure 2.2B), the graph can be segmented by solving the shortest path problem. In this dissertation, we utilize Dijkstra's algorithm [112] to find the minimum-weighted path, as its dynamic programming method makes it one of the fastest algorithms for finding the global minimum of an arbitrary directed graph with non-negative weights [114].

However, other optimization algorithms which utilize graph theory (e.g. the Bellman-Ford algorithm [115] or the max-flow min-cut technique [116]) may also be suitable for image segmentation. Selection of the appropriate algorithm is determined on a case by case basis. The benefits and drawbacks of each method are discussed in literature [115–119].

2.1.5 Segmenting Subsequent Structures

Once the first layer boundary is segmented on the image, other layer boundaries can be found iteratively by limiting the search space based on previous segmentations. Provided that the weights remain unchanged, the resulting effect is an iterative method in which layer boundaries are segmented by order of prominence. Alternatively, new weighting schemes may be used in subsequent iterations in order to segment different structure types.

2.2 GTDP for Closed-Contour Segmentation

Transformation of images into the polar domain has proven to be an effective tool within the medical community for segmenting circular biological structures [120–123]. This is due to the observation that circles in the Cartesian domain are represented

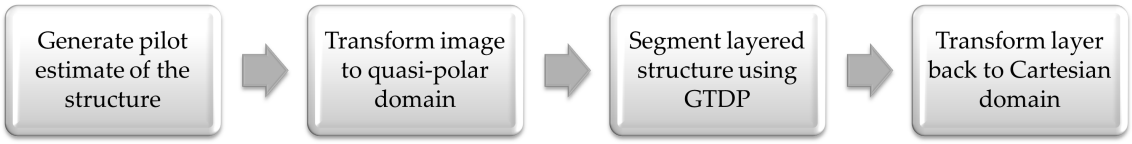

FIGURE 2.4: Flowchart of the GTDP framework for closed-contour segmentation.

as lines in the polar domain. Using this transform, the mathematical operations and manipulations required to segment the image are greatly simplified since these operations no longer need to be performed radially. However, for non-circular closed-contour structures, the polar transform is no longer adequate since oblong or convoluted features deviate from a flat path.

While algorithms have been developed to segment ophthalmic closed-contour structures [22, 25, 47, 87–110], many of the algorithms were developed for specific ophthalmic applications rather than as a general framework applicable to any closed-contour feature. Some algorithms, while generalizable, are computationally expensive or mathematically complex. Furthermore, in some cases such as with photoreceptor or corneal cell identification, cell counts or densities were achieved but the actual structure size and shape were not necessarily determined [22, 102–106, 108, 110].

This section presents an extension of our GTDP layer segmentation framework using what we call the *quasi-polar transform* to segment arbitrarily shaped closed-contour features [87]. The core steps are outlined in Figure 2.4 and detailed in the following subsections. Applications of the GTDP closed-contour segmentation framework can be found in Chapters 4 and 6.

2.2.1 Pilot Structure Estimation

The first step is to obtain pilot estimates of all closed-contour structures to segment. These estimates should contain information about both the location and shape of the

structures to segment. Feature localization prevents the algorithm from confusing the target structure with similarly-shaped features, while shape estimation results in a more accurate quasi-polar transform, as will be discussed in Section 2.2.2.

Given a grayscale image $\boldsymbol{I}_c^{full} \in \mathbb{R}^{M \times N}$ in the Cartesian domain and pixel $\boldsymbol{z} = [i, j]$ specifying the i^{th} row and j^{th} column on the image, the pilot estimates can be represented as a binary image $\boldsymbol{B}_c^{full}$, where

$$\boldsymbol{B}_c^{full}[\boldsymbol{z}] = \begin{cases} 1, & \text{if } \boldsymbol{z} \in \text{pilot estimate} \\ 0, & \text{otherwise} \end{cases}, \quad \forall\, \boldsymbol{z}. \tag{2.1}$$

Many basic techniques such as thresholding, contours, and local minima, or other methods such as the multi-scale generalized likelihood ratio test [124] can be used to obtain these estimates. To isolate a single closed-contour structure, $\boldsymbol{I}_c^{full}$ and $\boldsymbol{B}_c^{full}$ can be cropped to smaller image blocks $\boldsymbol{I}_c$ and $\boldsymbol{B}_c$, both $\in \mathbb{R}^{F \times G}$ where $F \leqslant M$ and $G \leqslant N$.

2.2.2 Quasi-Polar Transform

This section explains the quasi-polar transform in depth. In its simplest form, the quasi-polar transform can be described by a polar transform followed by a flattening step. Figure 2.5 shows an illustration where a circle, an oval, and an arbitrary shape in the Cartesian domain (Figures 2.5A-C) are transformed into the polar domain (Figures 2.5D-F). Information about the shape of the structure is then used to flatten the structure into a flat layer in the quasi-polar domain (Figure 2.5G). Once transformed into the quasi-polar domain, the structure can be segmented as a layer using the GTDP technique.

It can also be observed from Figure 2.5 that a simple polar transform is sufficient to map closed-contour shapes into layered structures. Motivation for a further transformation into the quasi-polar domain stems from the tendency for shorter geometric

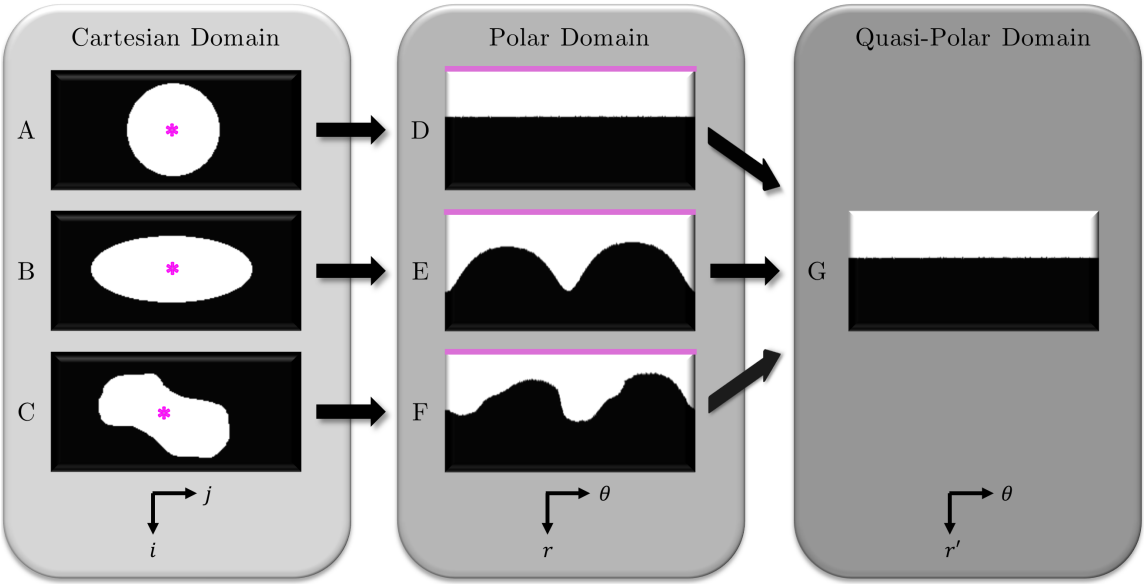

FIGURE 2.5: Schematic of the quasi-polar transform. (A-C) A circle, oval, and arbitrary shape in the Cartesian domain. (D-F) Transformation of A-C into the polar domain based on their centroids (pink asterisks in A-C). Note that the centroid in the Cartesian domain becomes a line (pink) in the polar domain. (G) Flattening of D-F in the polar domain into a flat layer in the quasi-polar domain. The result is a transformation of an arbitrary closed-contour shape in the Cartesian domain into a flat layer in the quasi-polar domain.

paths to be found when using the GTDP technique, especially in low SNR imaging scenarios. This is because fewer traversed nodes often yields a lower total weight, so the total cost to traverse along the boundary of an oblong feature in the polar domain may exceed that of a shorter geometric path. Furthermore, the likelihood of this occurring increases for images of lower quality since boundaries are even less apparent. By performing an extra flattening step, the path of the oblong structure reflects the shortest geometric distance.

The quasi-polar transform can be implemented using the following three steps:

1. Map pixels from the Cartesian domain into the polar domain based on their distance and angle from a reference pixel and axis, respectively. The reference pixel $\boldsymbol{z}_{ref}$ is any pixel where $\boldsymbol{B}_c[\boldsymbol{z}_{ref}] = 1$; however ideally $\boldsymbol{z}_{ref}$ lies at the center

of the closed-contour feature to facilitate its flatness in the polar domain. A good choice for $\boldsymbol{z}_{ref}$ is therefore the centroid of the pilot estimate, where

$$\boldsymbol{z}_{ref} = [i_{ref}, j_{ref}] = \frac{1}{K}\sum_{k=1}^{K} \boldsymbol{z}_k, \tag{2.2}$$

for the set of K pixels satisfying $\boldsymbol{B}_c[\boldsymbol{z}_k] = 1$. Example binary images ($\boldsymbol{B}_c$) are shown in Figure 2.5A-C with $\boldsymbol{z}_{ref}$ is marked as a pink asterisk.

Next, generate the polar-transformed binary images $\boldsymbol{B}_p$ (Figures 2.5D-F) and $\boldsymbol{I}_p \in \mathbb{R}^{R\times\Theta}$ following

$$\begin{aligned} \boldsymbol{B}_p[r,\theta] &= \boldsymbol{B}_c[i,j] \\ i &= \lfloor r\cdot\sin\theta + i_{ref} \rceil \\ j &= \lfloor r\cdot\cos\theta + j_{ref} \rceil, \end{aligned} \tag{2.3}$$

where the j-axis is the reference axis and the same transformation is applied to map $\boldsymbol{I}_c \rightarrow \boldsymbol{I}_p$. In Equation (2.3), $\boldsymbol{B}_p[r,\theta]$ denotes the pixel in $\boldsymbol{B}_c$ with a radius r and angle θ from the reference pixel and axis, respectively. The step sizes and ranges for the r and θ axes may be defined based on the application. Note that since $\boldsymbol{B}_c$ and $\boldsymbol{I}_c$ are rectangular, there will likely be $[r,\theta]$ combinations which are non-existent in the Cartesian domain. In these cases, the values can be left as undefined or the search space can be limited to excluded these regions.

2. Find a discrete function $r = f_p[\theta]$ $\{f_p[\theta] \in \mathbb{Z} \mid 1 \leqslant f_p[\theta] \leqslant R\}$ that best estimates the boundary between the background and the pilot estimate in $\boldsymbol{B}_p$. This can be achieved by taking the vertical gradient of the image or by using the GTDP layer segmentation technique described in Section 2.1 with weights determined by the vertical gradient of $\boldsymbol{B}_p$.

3. Generate the quasi-polar images $\boldsymbol{B}_q$ (Figure 2.5G) and $\boldsymbol{I}_q \in \mathbb{R}^{R\times\Theta}$ where for

all columns $\{\boldsymbol{b}_{pk}\}_{k=1}^{\Theta}$ in $\boldsymbol{B}_p$, the k^{th} column $\boldsymbol{b}_{qk}$ in $\boldsymbol{B}_q$ is determined by

$$\boldsymbol{b}_{qk} = \boldsymbol{C}_k \cdot \boldsymbol{b}_{pk}$$

$$\boldsymbol{C}_k[i,j] = \begin{cases} 1, & \text{if } i = \left\lfloor \frac{1}{\Theta} \sum_{\theta=1}^{\Theta} f_p[\theta] \right\rfloor - f_p[k] + j \\ 0, & \text{otherwise} \end{cases}, \quad \in \mathbb{R}^{R \times R}. \tag{2.4}$$

Use the exact transformation mapping $\boldsymbol{B}_p \rightarrow \boldsymbol{B}_q$ to then transform $\boldsymbol{I}_p$ into its quasi-polar equivalent, $\boldsymbol{I}_q$. Since this step flattens the pilot estimate instead of the structure itself, in general the structure is not perfectly flat in $\boldsymbol{I}_q$. This also implies that a pilot estimate shape closer to the actual structure shape results in a flatter layered structure in the quasi-polar domain.

2.2.3 Layer Segmentation Using GTDP

Once the image is transformed into the quasi-polar domain, $\boldsymbol{I}_q$ can be segmented using the automatic GTDP layer segmentation algorithm described in Section 2.1 with the graph and edge weights generated based on $\boldsymbol{I}_q$ instead of $\boldsymbol{I}_c$.

2.2.4 Inverse Quasi-Polar Transform

After segmenting the structure in the quasi-polar domain, the shortest path $r' = f_q[\theta]$ is transformed back into the Cartesian domain using the following three steps:

1. Create an image $\boldsymbol{S}_q \in \mathbb{R}^{R \times \Theta}$ of the segmentation $r' = f_q[\theta]$ in the quasi-polar domain where

$$\boldsymbol{S}_q[r', \theta] = \begin{cases} 1, & \text{if } r' = f_q[\theta] \\ 0, & \text{otherwise} \end{cases}, \quad \forall\ r', \theta. \tag{2.5}$$

2. Apply the inverse of the flattening step described in Equation (2.4) to transform $\boldsymbol{S}_q$ into $\boldsymbol{S}_p \in \mathbb{R}^{R \times \Theta}$ in the polar domain. In other words, for all columns $\{\boldsymbol{s}_{qk}\}_{k=1}^{\Theta}$

in $\boldsymbol{S}_q$, the k^{th} column $\boldsymbol{s}_{pk}$ in $\boldsymbol{S}_p$ is determined by

$$\boldsymbol{s}_{pk} = \boldsymbol{C}_k^{inv} \cdot \boldsymbol{s}_{qk}$$

$$\boldsymbol{C}_k^{inv}[i,j] = \begin{cases} 1, & \text{if } i = f_p[k] - \left\lfloor \frac{1}{\Theta} \sum_{\theta=1}^{\Theta} f_p[\theta] \right\rfloor + j \\ 0, & \text{otherwise} \end{cases}, \quad \in \mathbb{R}^{R \times R}. \tag{2.6}$$

3. Perform the inverse of the polar transform described in Equation (2.3) to generate an image $\boldsymbol{S}_c \in \mathbb{R}^{F \times G}$ of the segmentation in the Cartesian domain where $\boldsymbol{S}_c[i,j] = \boldsymbol{S}_p[r,\theta]$.

2.2.5 Segmenting Subsequent Structures

Subsequent structures can be segmented by repeating the steps in Sections 2.2.2 to 2.2.4 for every cropped image block $\boldsymbol{I}_c$. This can be achieved by sequential segmentation of individual features, or by parallelizing the segmentation of individual image blocks. While parallel processing is computationally faster, sequential segmentation allows for search region limitation (Section 2.1.3) based on previously segmented structures.

3

Segmentation of OCT Retinal Layers

3.1 Motivation

Accurate detection of anatomical and pathological structures in SD-OCT images is important for the diagnosis and study of ocular diseases. Until recently, ophthalmic studies obtained quantitative data by manually segmenting the features of interest. Manual segmentation is not only demanding for expert graders, but is also extremely time-consuming for clinical use and for large scale, multi-center trials. Furthermore, the inherent variability between graders yields subjective results.

3.2 GTDP Retinal Layer Segmentation Algorithm

We developed an algorithm to automatically segment eight retinal layer boundaries on unaveraged macular SD-OCT images of normal eyes and validated the algorithm for accuracy and reproducibility [56]. We based the algorithm on the GTDP layer segmentation framework described in Section 2.1 with the assumption that the B-scans were located in the macular region without the optic nerve head present. Further information about the image sizes and resolutions can be found in Section 3.3.

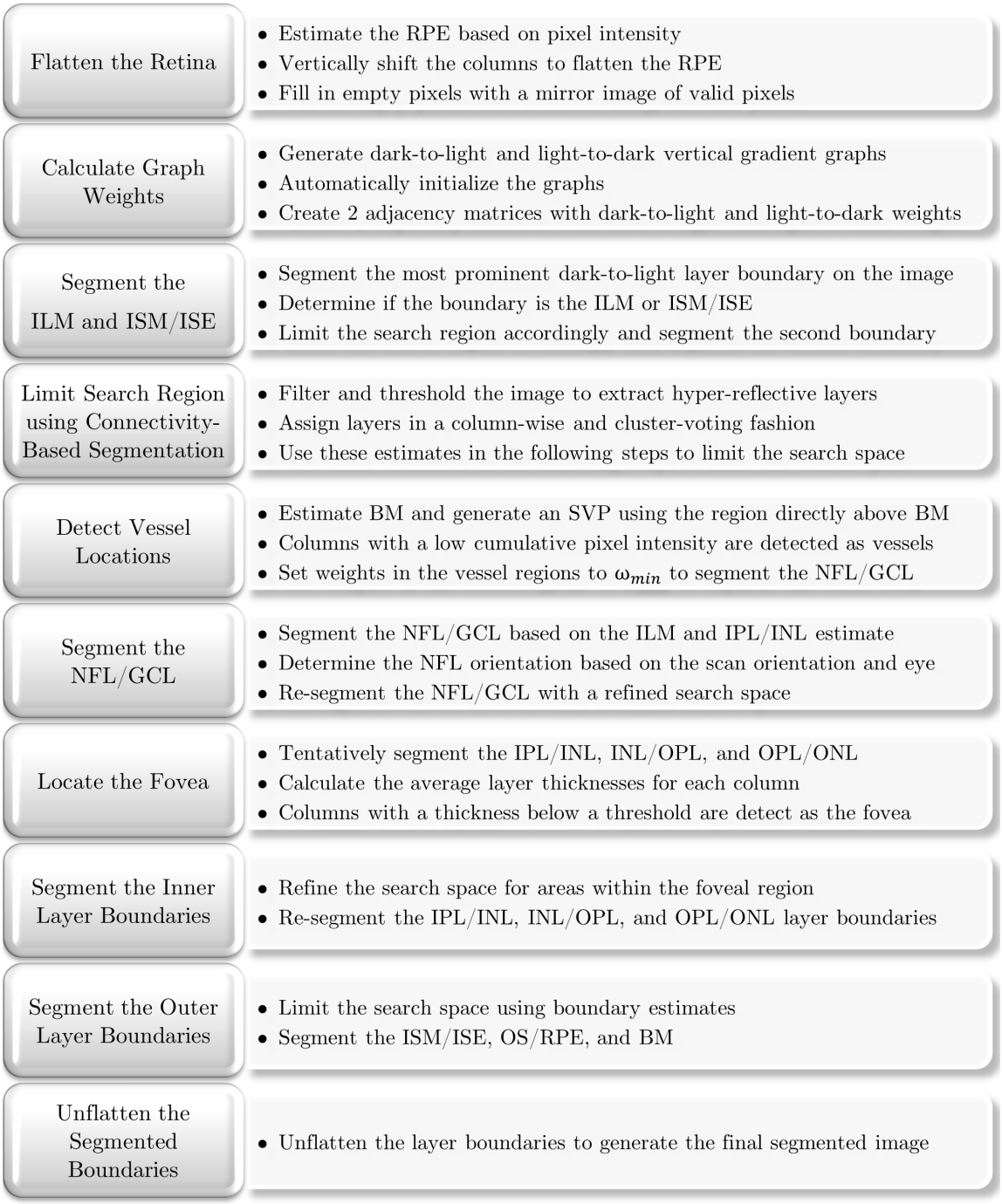

FIGURE 3.1: Outline for segmenting eight retinal layer boundaries on SD-OCT images of normal retina.

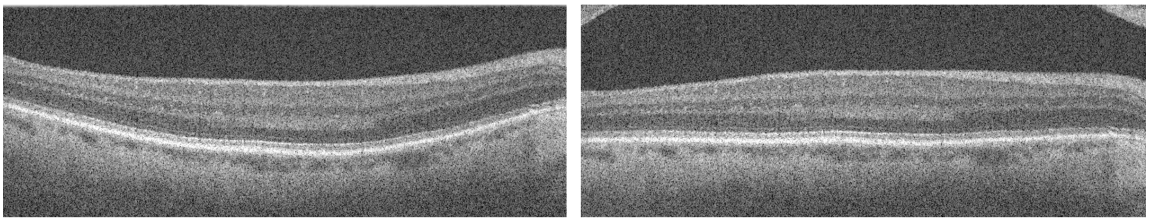

A B

FIGURE 3.2: Retinal flattening. (A) The original retinal SD-OCT image, and (B) the image after flattening the retina.

Figure 3.1 shows an outline of the algorithm, and the following subsections discuss each of the outlined steps in detail. While this section describes the methods for one possible implementation, newer techniques (see Section 8.3) may be utilized to improve segmentation results.

3.2.1 Flattening the Retina

Since the GTDP framework segments layer boundaries by computing the minimum-weighted path from a start node to an end node, inherent in this method is the tendency for the shortest geometric path to be found since fewer traversed nodes results in a lower total weight. As a result, features with strong curvatures or other irregularities are disadvantaged since their paths do not reflect the shortest geometric distance. A natural solution is to therefore transform the image such that the desired path is shortened.

To account for the natural retinal curvature seen in SD-OCT images, we flatten the retina to avoid inaccurate shortcuts across the layers when segmenting. Figure 3.2 demonstrates retinal flattening, where Figure 3.2B is the flattened version of the original image shown in Figure 3.2A. The retina is flattened by using an estimate of the RPE as a guideline. Since the RPE is one of the most hyper-reflective layers on SD-OCT images, we estimate the RPE by Gaussian-filtering the image and tentatively assigning the RPE as the brightest pixel in each column. We then locate

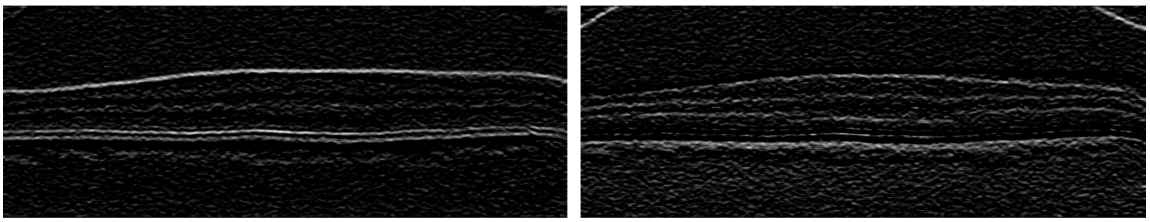

A B

FIGURE 3.3: Vertical gradient images used to calculate edge weights. (A) A dark-to-light gradient image for segmenting a darker layer above a lighter layer, and (B) a light-to-dark gradient image for segmenting a lighter layer above a darker layer.

outliers (often associated with the nerve fiber layer (NFL)) by searching for discontinuities greater than 161.5 µm in the RPE estimate. These outliers are removed from the RPE estimate along with pixels lying in columns with a significantly lower SNR. We fit a second order polynomial to the remaining valid RPE points, and shift each column up or down such that the RPE points lie on a flat line (see Equation (2.4)). Regions on the newly flattened image that are outside the original field-of-view are extrapolated from the mirror image of the valid pixels. This avoids border artifacts when later filtering the image.

3.2.2 Weight Calculation

Graph weights in literature [113] often include two terms representing the geometric distance and intensity difference between graph nodes. In SD-OCT images, retinal layers are primarily horizontal structures distinguishable by a dark-to-light or light-to-dark change in pixel intensity in the vertical direction [53]. Complementary gradient images $\boldsymbol{G}^{DL}$ and $\boldsymbol{G}^{LD}$ (Figure 3.3) can therefore be generated to highlight these boundaries following

$$\boldsymbol{G}^{DL} = \boldsymbol{I} * \begin{bmatrix} 1 \\ -1 \end{bmatrix}, \quad \boldsymbol{G}^{LD} = \boldsymbol{I} * \begin{bmatrix} -1 \\ 1 \end{bmatrix}. \tag{3.1}$$

To segment the dark-to-light retinal boundaries including the inner limiting mem-

brane (ILM), inner nuclear layer (INL) / outer plexiform layer (OPL), inner segment myeloid (ISM) / ISE, and OS/RPE, as well as the light-to-dark boundaries including the NFL / ganglion cell layer (GCL), inner plexiform layer (IPL) / INL, OPL / outer nuclear layer (ONL), and Bruch's Membrane (BM), we create two undirected adjacency matrices with the following weights, respectively, following

$$\omega_{ab} = \text{LinNorm}\left(-g_a^{DL} - g_b^{DL},\ 0,\ 1\right) + \omega_{min} \tag{3.2}$$

$$\omega_{ab} = \text{LinNorm}\left(-g_a^{LD} - g_b^{LD},\ 0,\ 1\right) + \omega_{min}, \tag{3.3}$$

where ω_{ab} is the weight of the edge connecting nodes a and b, g_n^{DL} and g_n^{LD} are the values of $\boldsymbol{G}^{DL}$ and $\boldsymbol{G}^{LD}$ at node n, ω_{min} is the minimal non-zero weight set to 1×10^{-5} in our implementation, and $\text{LinNorm}(\boldsymbol{x}, \alpha, \beta)$ denotes a linear normalization of the values in $\boldsymbol{x}$ to range from α to β where

$$\hat{\boldsymbol{x}} = \text{LinNorm}(\boldsymbol{x}, \alpha, \beta) = \left(\frac{\boldsymbol{x} - \min(\boldsymbol{x})}{\max(\boldsymbol{x}) - \min(\boldsymbol{x})}\right)(\beta - \alpha) + \alpha. \tag{3.4}$$

Finally, for automatic endpoint initialization as discussed in Section 2.1.2, the end columns are duplicated and added to either side of the image with vertical edge weights equal to ω_{min}.

3.2.3 ILM and ISM/ISE Segmentation

We implement the segmentation of multiple layers in an iterative process, where layer boundaries are segmented by order of prominence. The ILM and ISM/ISE are the two most prominent layer boundaries in an SD-OCT retinal image due to their high contrast in pixel intensity. Using the dark-to-light weights in Equation (3.2) and Dijkstra's algorithm, we find the shortest path with start and end points initialized to the upper left and bottom right nodes on the graph. Due to the prominence of the ILM and ISM/ISE, the resulting segmentation corresponds to one of the two boundaries.

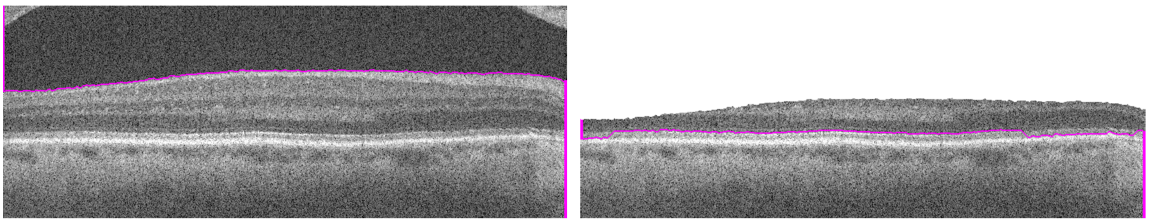

A B

FIGURE 3.4: GTDP segmentation of the ILM and ISM/ISE using Dijkstra's algorithm, automatic endpoint initialization, and search region limitation. (A) Segmentation of the ILM using automatic endpoint initialization, and (B) the pilot ISM/ISE segmented with a limited search region.

To determine which boundary was segmented, we inspect the region above the segmented path. Since the ILM is the inner-most boundary of the retina on an OCT image, there is little hyper-reflectivity above it. In contrast, the inner retinal layers sit above the ISM/ISE which exhibit hyper-reflectivity. In order to determine whether hyper-reflectivity is present, we first filter the image with a Gaussian kernel and threshold the smoothed image using Otsu's method [125] to generate a binary mask. This step isolates the NFL-OPL and ISE-RPE regions. The fraction of bright pixels in the region above the segmentation is then calculated using the binary image. If the fraction exceeds 0.025, then we conclude that the segmented layer boundary is the ISM/ISE due to the presence of hyper-reflective layers. Otherwise, we conclude that the ILM was segmented.

If the ISM/ISE was first segmented, we then limit the search region as described in Section 2.1.3 to the region 64.6 µm above the segmented line to subsequently segment the ILM. If the ILM was segmented first, then the search space is limited to the region 129.2 µm below the boundary to segment the ISM/ISE. Consequently, the algorithm successfully segments the two most prominent layer boundaries.

Figure 3.4A shows the image from Figure 3.2B where the ILM is first segmented given a search space of the entire image. The search region is then limited to the

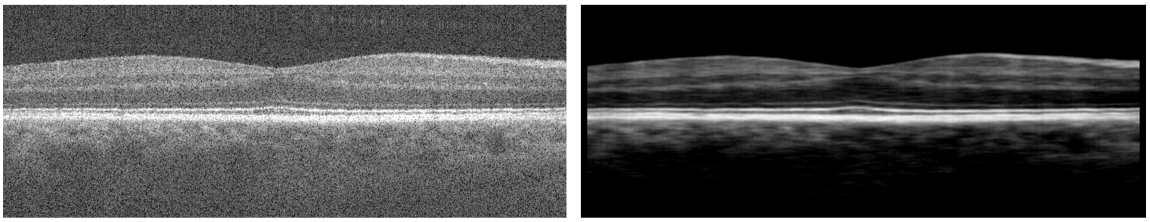

A B

FIGURE 3.5: (A) A flattened retinal SD-OCT image, and (B) the contrast-enhanced image.

space shown in Figure 3.4B, resulting in the segmented ISM/ISE boundary. This example also shows the result of using the first automatic endpoint initialization method from Section 2.1.2. Lastly, note that the pilot ISM/ISE detected at this stage may be inaccurate due to confusion with the OS/RPE boundary. Such errors are corrected in Section 3.2.8.

3.2.4 Search Region Limitation using Connectivity-Based Segmentation

While the ILM and ISM/ISE are easily identifiable due to the prominent change in hyper-reflectivity, the remaining layer boundaries are not as distinct. To accurately segment these remaining layers, we introduce a method for defining a valid and narrow search region that isolates the layer boundaries of interest. Our method is implemented in two steps. We first develop pilot estimates of hyper-reflective pixel clusters using a column-wise intensity profiling technique. We then connect and modify clusters associated with a particular layer in what we call the connectivity-based step. We exploit the resulting layer estimations to limit search regions in Sections 3.2.6 to 3.2.8. The column-wise intensity profiling and connectivity-based segmentation steps are described in the following paragraphs.

First, we enhance the contrast between the light and dark layers. To achieve this, we coarsely denoise the image with a rectangular averaging filter that is 3×19 pixels in size. Next, we threshold this image by setting intensities smaller than the

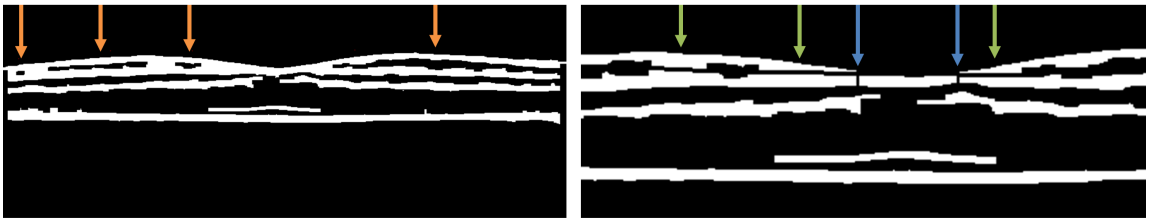

A B

FIGURE 3.6: Binary mask estimating hyper-reflective layers. (A) A binary mask of the filtered image in Figure 3.5B. The orange arrows point to holes corresponding to the GCL layer. (B) A zoomed-in image of A where merged layers have been disconnected by interpolating the lower boundaries of the holes from A (green arrows). Vertical breaks were used to separate clusters not disconnected through interpolation (blue arrows).

median of their corresponding column to zero. An example contrast-enhanced image is shown in Figure 3.5B.

A binary mask is then generated to isolate the hyper-reflective layers. This is done by taking the column-wise second-order derivative of the contrast-enhanced image to boost layer boundaries [126]. We then create a pilot binary mask by thresholding out any values less than zero. To remove outliers in each column, we set all non-zero clusters less than 16.15 µm tall to zero and join the remaining clusters that are closer than 9.69 µm from each other. The resulting mask corresponds to the hyper-reflective layers in the retina (i.e. NFL, IPL, OPL, ISE, and RPE). A horizontal 1D closing operation with a kernel of 10 pixels in size is performed on the image as a whole to close gaps, and any clusters less than 500 pixels in size are removed. The result is a coarse binary mask of the hyper-reflective retinal layers, as shown in Figure 3.6A.

Since some of the hyper-reflective layers may be joined together as seen in the top layers of Figure 3.6A, we disconnect the merged layers using neighboring columns with already-detached layers. This is done by first detecting pixel clusters with holes corresponding to a detected middle hypo-reflective layer. Examples of this are shown by Figure 3.6A, where the top cluster contains merged NFL-OPL regions as well as

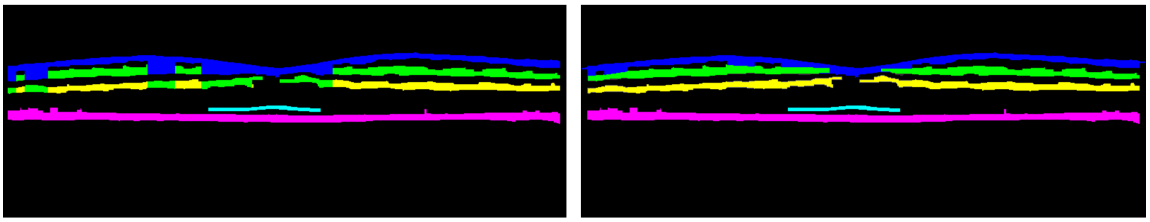

A B

FIGURE 3.7: Connectivity-based retinal layer assignments for the NFL (blue), IPL (green), OPL (yellow), ISE (cyan), and RPE (magenta). (A) Column-wise layer assignments of the mask in Figure 3.6A, noting the conflicts in the top three layer assignments. (B) Cluster-based refinement of the layer assignments in A.

holes (orange arrows) corresponding to the GCL. The merged layers are separated by interpolating the lower boundaries of the GCL holes (Figure 3.6B, green arrows). Since some layers may still be merged as shown in the foveal region of Figure 3.6B, these layers are separated from the original cluster with vertical breaks (Figure 3.6B, blue arrows).

The algorithm then examines each column in the original binary mask (Figure 3.6A) and tentatively assigns each pixel cluster in a column to a particular anatomical layer. The available choices for hyper-reflective layers are 1) NFL, 2) IPL, 3) OPL, 4) ISE, 5) RPE, or "no assignment" in the case that the rules fail to reach a reasonably certain assignment. To do this, the number of clusters is counted for each column. For columns with five clusters, the retinal layer assignments are straightforward since there is a 1:1 correspondence with the target layers. To determine missing layers in columns with fewer than five clusters, we take layer distances into consideration. For instance, we assume that the OS/RPE is at least 06.9 µm below the ILM, and the distance between the RPE and ISE is less than 32.3 µm. The end result is the tentatively-assigned retinal layers shown in Figure 3.7A.

To correct possible conflicts in the column-wise layer assignments where pixels within a 2D cluster were assigned as different layers (Figure 3.7A), we reassign all

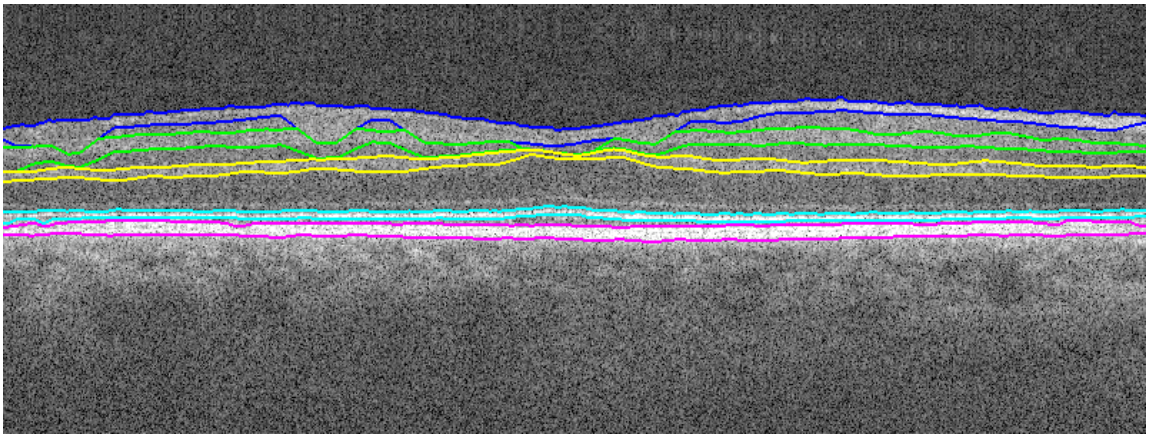

FIGURE 3.8: Connectivity-based retinal layer boundary segmentation of the NFL (blue), IPL (green), OPL (yellow), ISE (cyan), and RPE (magenta) using the assignments from Figure 3.7.

pixels in that cluster to the majority tentative assignment. The result from this cluster-based refinement method is shown in Figure 3.7B.

The boundaries of the NFL, IPL, and OPL are determined by finding the top and bottom edges of the assigned pixel clusters in Figure 3.7B. Next, we find the RPE by locating the brightest pixels in the contrast-enhanced image that are a) assigned as the ISE or RPE in Figure 3.7A, and b) the furthest from the top of the image in a given column; these pixels are then assigned as the center of the RPE. This center RPE line is smoothed with a median filter, and the RPE edges are located by searching for large changes in gradient on the contrast-enhanced image. A similar method is then used to locate the ISE edges, where the search region is just above the RPE layer. The resulting retinal layer estimates are displayed in Figure 3.8. Because these layer estimations still contain errors, they are refined in the subsequent sections using GTDP layer segmentation.

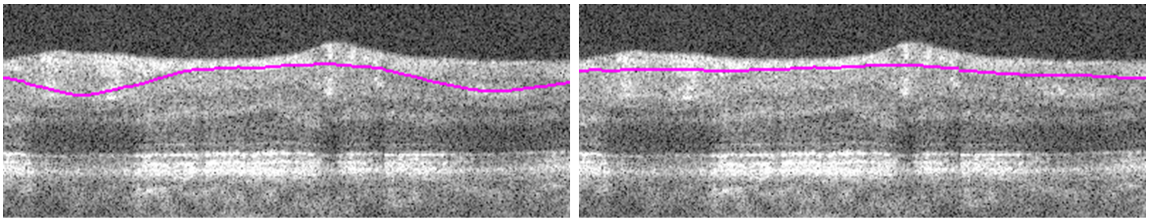

A B

FIGURE 3.9: Vessel detection. (A) NFL/GCL segmentation (magenta) without vessel detection, and (B) NFL/GCL segmentation with indifferent weights in the detected vessel regions.

3.2.5 Vessel Detection

Retinal SD-OCT images with prominent vessels can be challenging when segmenting the NFL/GCL boundary because there are hyper-reflective bulges in the NFL layer as shown in Figure 3.9A. To address this problem, we detect major vessels on individual B-scans and alter the graph weights accordingly so that segmentation algorithm is indifferent to the bulges in the NFL layer. In the first step, we tentatively segment BM using GTDP, where the pilot ISM/ISE segmentation is used to limit the search region. A Gaussian filter is then applied to the image, and columns lying between BM and 48.45 µm above BM are summed. Since the presence of vessels results in a dark shadowing in the summed region, columns exhibiting a low sum are defined as vessel regions. In the second step, we set edge weights in the vessel regions to ω_{min} when segmenting the NFL/GCL in Section 3.2.6. Figure 3.9B demonstrates the effectiveness of the vessel correction algorithm in improving the accuracy of NFL/GCL boundary detection.

3.2.6 NFL/GCL Segmentation

After incorporating minimum weights in the vessel regions and estimating the layer boundaries using connectivity-based segmentation, we form a pilot estimate of the NFL/GCL layer boundary using GTDP and the updated light-to-dark graph weights

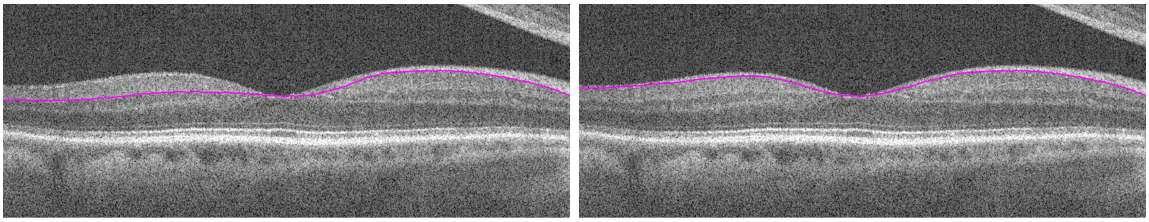

A B

FIGURE 3.10: NFL/GCL Segmentation. (A) NFL/GCL pilot segmentation (magenta), and (B) NFL/GCL segmentation after refining the search region based on the NFL orientation.

in Equation (3.3). We limit the search region using the ILM from Section 3.2.3 and the estimated IPL/INL from Section 3.2.4 prior to segmenting.

Since the NFL/GCL exhibits similar light-to-dark gradient characteristics to the IPL/INL boundary and since the thicker NFL layer on the nasal side of the fovea necessitates an asymmetric larger search region, we include additional restrictions to avoid NFL/GCL and IPL/INL confusion that may arise (Figure 3.10A). First, the image side which is temporal to the fovea is determined based on knowledge of the scan orientation (horizontal or vertical) and which eye was imaged (left or right). For instance, horizontal scans of the left eye exhibit layer thinning on the right side of the fovea, whereas vertical scans of the left eye show layer thinning on both sides of the fovea.

Using the ILM and the preliminary NFL/GCL boundary, we estimate the NFL thickness. Moving across the image from the thicker to the thinner side of the layer, we find the first instance where the thickness drops below a threshold of 19.38 µm and mark it as the divide between the thick and thin sides. We limit the search region on the thinner NFL side to 32.3 µm below the ILM, and the search region on the thicker side is expanded from 16.15 µm below the ILM to 16.15 µm below the preliminary NFL/GCL segmentation. Figure 3.10B shows the resulting NFL/GCL segmentation after a further restriction of the search region.

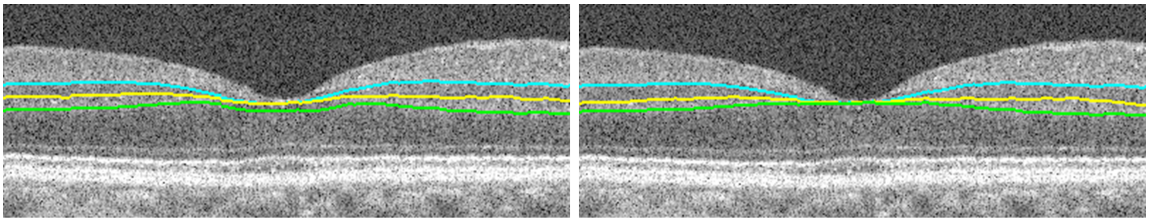

A B

FIGURE 3.11: Foveal correction. (A) GCL/IPL (cyan), INL/OPL (yellow), and OPL/ONL (green) pilot segmentations, and (B) the segmented inner retinal layer boundaries after foveal detection and further restriction of the search region.

3.2.7 Foveal Detection and Inner Retinal Layer Segmentation

It is important to detect whether the image contains the fovea since layers merge together and become increasingly indistinguishable near the fovea. Due to the specified search region padding between layer boundaries, errors similar to the example in Figure 3.11A often appear in the pilot segmentations for B-scans containing the fovea. To address such problems, we first perform pilot GTDP segmentations of the IPL/INL, INL/OPL, and OPL/ONL using the appropriate light-to-dark or dark-to-light adjacency matrix and search region limitation from previously segmented boundaries. For example, the IPL/INL search region is limited to 9.69 µm below the NFL/GCL and above the estimated IPL/INL or INL/OPL boundaries, whichever is higher.

In the next step, we estimate the presence and location of the fovea by calculating the NFL, GCL-IPL, INL, and OPL layer thicknesses from the tentatively segmented layers. We then assign columns with a mean layer thickness of less than 16.15 µm as the foveal region. Since this region may not necessarily be centered at the fovea, we locate the center by calculating the ILM-ISE thickness, where the column containing the minimum thickness is located and expanded by 20 pixels on either side. If this region coincides with the foveal region detected prior, then it is included as a part of the fovea.

After locating the fovea, we define more accurate search regions to account for foveal layer merging. This is done by maintaining the position of the lower search space boundary while expanding the top boundary upward to the ILM when re-segmenting the IPL/INL, INL/OPL, and OPL/ONL. The resulting segmentations are more accurate, as depicted in Figure 3.11B.

3.2.8 Outer Retinal Layer Segmentation

The remaining outer retinal boundaries (ISM/ISE, OS/RPE, and BM) are segmented in a straightforward manner by exploiting the previously estimated layer boundaries, the connectivity-based search regions, and GTDP. In particular, we improve upon the ISM/ISE estimate from Section 3.2.3 to remove any possible ISM/ISE and OS/RPE confusion. Our implementation re-segments the ISM/ISE with a modified search region ranging from 12.92 µm below the segmented OPL/ONL boundary to 6.46 µm above the estimated OS/RPE from Section 3.2.4.

3.2.9 Unflattening the Retina

After segmenting all layer boundaries, we restore the original curvature of the retina by shifting the columns up or down in the direction opposite to the flattening performed in Section 3.2.1 (see Equation (2.6)). The result is an algorithm that segments eight retinal layer boundaries on a given SD-OCT image.

3.3 Validation Methods

3.3.1 Automatic versus Manual Segmentation

To determine the accuracy of the eight retinal layer boundary segmentation algorithm for SD-OCT images, we conducted an automatic versus manual segmentation study. This study included macular scans from normal adult subjects segmented manually by an expert grader and automatically using our algorithm. To estimate inter-

observer variability, a subset of scans was graded manually by a second expert. Both expert graders were OCT readers certified by the Duke Reading Center.

Volumetric scans (6.7 × 6.7 mm) were acquired from 10 normal adult subjects in an institutional review board (IRB) approved protocol using Bioptigen (Research Triangle Park, NC, USA) SD-OCT imaging systems with an axial full-width at half-maximum (FWHM) resolution of 4.6 µm in tissue and an axial pixel resolution of 3.23 µm. Five of the volumetric scans had lateral and azimuthal pixel resolutions of 6.7 µm and 67 µm (1000 A-scans × 100 B-scans), respectively. The other five volumetric scans had resolutions of 13.4 µm and 33.5 µm (500 A-scans × 200 B-scans) to validate the algorithm on varying lateral and azimuthal image resolutions.

To compare the automatic versus manual segmentation results, 11 B-scans from each data set were selected with the sixth B-scan centered at the fovea and subsequent B-scans departing from the fovea at a linear rate. The inter-observer comparison included a subset of three B-scans from each set of 11 B-scans. The three B-scans chosen from each set included the foveal scan and two other randomly selected B-scans. Due to a prominent, irregular imaging artifact in one of the B-scans and a gross manual segmentation error in another B-scan, a total of two B-scans were removed from the study. Furthermore, eight B-scans were used as training data for bias correction as discussed below. As a result, 100 B-scans (10 B-scans per data set) were observed for the automatic versus manual comparison and a subset of 29 B-scans (3 B-scans per dataset with the exception of one) were included in the inter-observer comparison.

Prior to automatic segmentation, ten percent of the image width was cropped from either side of each image to remove regions with low signal. Eight retinal layer boundaries were segmented automatically on 108 B-scans using a MATLAB (The Mathworks, Natick, MA, USA) software implementation of our algorithm. The same eight layers were manually traced by two expert graders for the subset of 29

B-scans. Furthermore, these certified graders traced layers using their own expertise and were not allowed to consult with each other.

In order to closely match the segmentation results of an expert grader, the automatic segmentation results were smoothed using a moving average filter. This was necessary because the automatic algorithm tightly followed gradient changes, whereas manual segmentation tended to be smooth. Furthermore, each expert grader exhibited a bias when tracing layer boundaries, either consistently following above or below the actual boundary by a constant offset. As a result, training was performed on the eight test images to determine any segmentation biases from manual grading. Each automatically segmented layer in the set of 100 B-scans was then shifted up or down by bias values of -2.907, -2.584, -3.23, -4.199, -5.168, -4.199, -0.969, and -1.938 µm, respectively, in order to mimic the segmentation behavior of the manual grader.

Upon smoothing the layers and correcting for bias, we calculated the thicknesses of the seven retinal layers for each of the 100 B-scans between neighboring layer boundaries. The mean signed difference in layer thickness between automatic and manual segmentation was computed for each layer on each B-scan. The same was done to compare the two manual expert graders for 29 B-scans. Finally, the mean unsigned error in layer thickness was computed across all B-scans.

3.3.2 Algorithm Reproducibility

To test the reproducibility of the proposed method, we captured five volumetric scans of one normal subject with lateral and azimuthal pixel resolutions of 6.7 µm and 67 µm (1000 A-scans × 100 B-scans), respectively. The subject rested between each volumetric image capture. In accordance with longstanding clinical convention (described in the Age-Related Eye Disease Study (AREDS) [127]), we calculated the volume of each retinal layer within a 3-mm diameter circle around the fovea. We selected one of these volumetric scans as the anchor and compared the automatically

Table 3.1: Automatic versus manual segmentation results. *Column II:* differences in retinal layer thickness between two expert manual graders across 29 B-scans. *Column III:* differences between automatic segmentation and one grader for the same 29 B-scans. *Column IV:* differences between automatic and manual segmentation by the more senior grader for 100 B-scans. Each pixel is 3.23 µm.

	Inter-Observer	**Automatic vs Manual**	
	29 B-scans		100 B-scans
Retinal Layer	Mean ± SD (µm)	Mean ± SD (µm)	Mean ± SD (µm)
NFL	5.59 ± 2.91	3.17 ± 2.49	2.94 ± 2.23
GCL-IPL	3.42 ± 3.07	1.84 ± 1.55	2.52 ± 2.10
INL	7.17 ± 4.20	3.49 ± 2.81	3.17 ± 2.42
OPL	6.14 ± 4.94	5.20 ± 3.52	4.88 ± 3.36
ONL-ISM	5.26 ± 3.84	4.39 ± 3.49	3.84 ± 3.04
ISE-OS	3.59 ± 2.84	2.94 ± 2.71	2.81 ± 2.49
RPE	7.14 ± 3.23	3.10 ± 2.23	3.10 ± 2.75
TR	7.17 ± 3.23	3.07 ± 2.65	3.07 ± 2.71

measured volume for each layer with those of the other scans. We calculated the normalized mean and standard deviation (SD) of the differences in layer volume measurements.

3.4 Validation Results and Discussion

3.4.1 Automatic versus Manual Segmentation Results

The layer thickness errors when comparing automatic versus manual segmentation are shown in Table 3.1. Column II shows the mean thickness error for the various retinal layers as measured by two expert manual graders for 29 B-scans. Column III displays the same layer thickness difference calculation for the 29 B-scans, but with layer thicknesses determined by the automatic segmentation algorithm and the more senior manual grader. Column VI reports the thickness errors between the automatic and manual grader for the larger set of 100 B-scans.

The results in Table 3.1 show that the automatic algorithm accurately segmented

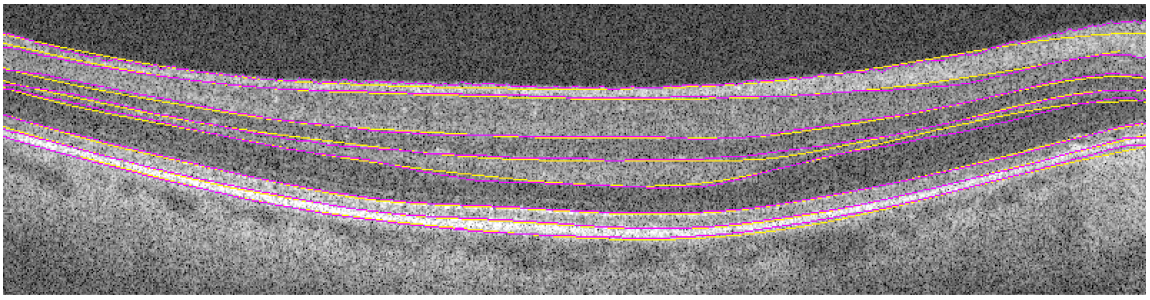

FIGURE 3.12: Comparison of automatic (magenta) versus manual (yellow) segmentation.

seven retinal layers in normal adult eyes more closely to an expert grader as compared to another grader. For example, two manual graders differed in their segmentation of the TR by an average of 7.17 µm, whereas our fully automatic algorithm differed from one of the manual graders by an average of 3.07 µm. Figure 3.12 displays the qualitative results, with the automatic segmentation (magenta) overlaid with the manual segmentation (yellow) results.

3.4.2 Reproducibility Results

Table 3.2 shows mean percent differences in the estimated layer volumes across five volume scans of the same eye. Differences in layer volume may be partially attributed to the fact that the volumes were unregistered. Furthermore, factors such as uncontrollable patient motion during scan acquisitions, improper alignment of the imaging system with the eye, or a low sampling density in the azimuthal dimension may have affected layer volumes.

3.5 Summary

An automatic retinal layer segmentation algorithm was developed using the GTDP framework to segment eight retinal layer boundaries on SD-OCT images of normal eyes. The algorithm was shown to accurately segment these boundaries with repro-

Table 3.2: Reproducibility of retinal layer thickness volumes. Percent differences in layer volumes across five volume scans of the same eye.

Layer	**Mean ± SD (%)**
NFL	3.88 ± 3.43
GCL-IPL	1.70 ± 1.99
INL	3.37 ± 3.43
OPL	2.20 ± 2.01
ONL-ISM	1.02 ± 0.76
ISE-OS	0.84 ± 0.61
RPE	0.16 ± 0.18
TR	0.26 ± 0.09

ducible results that matched an expert grader more closely than a second grader. This is highly encouraging for reducing the time and manpower required to segment images in ophthalmic studies.

4

Segmentation of AOSLO Photoreceptors

4.1 Motivation

Recent innovations in ophthalmic imaging such as the integration of AO technology have enabled visualization of the photoreceptor mosaic. As a result, many studies have been conducted on the photoreceptor mosaic to gather normative data on photoreceptor distribution [128, 129], density [130–132], spacing [19, 38, 133], directionality [134], and temporal changes [104, 135].

To generate quantitative metrics of the photoreceptor mosaic, identification of individual photoreceptors is often a required step. Since manual identification is extremely time-consuming, many groups have utilized some form of automation when studying the photoreceptor mosaic [21, 22, 25, 27, 129, 131]. Cone identification algorithms have also been developed and validated for accuracy [102, 103, 136–138]. For example, the Garrioch *et al.* 2012 algorithm [139] is a modified version of the Li & Roorda 2007 algorithm [102] and was thoroughly validated for repeatability on a large cone mosaic dataset. Even so, manual correction was still necessary to identify missed photoreceptors [34, 132].

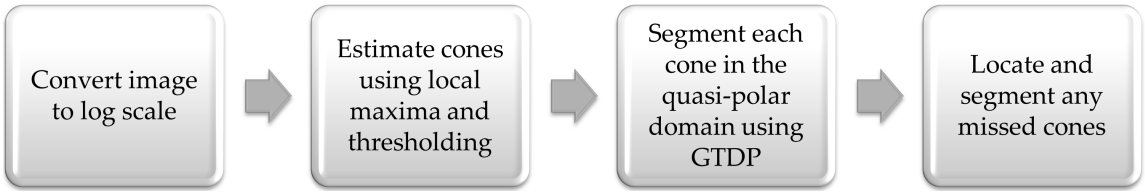

FIGURE 4.1: Flowchart of the GTDP algorithm for segmenting cone photoreceptors on AOSLO images of normal eyes.

4.2 GTDP Cone Photoreceptor Segmentation Algorithm

We developed an algorithm to automatically segment cone photoreceptors on *in vivo* AOSLO images of the human photoreceptor mosaic. The algorithm was developed based on the GTDP framework for closed-contour structures described in Section 2.2, and was later extended to segment both rod and cone photoreceptors. Figure 4.1 outlines the algorithm steps and details on the image dataset are described in Section 4.4.1.

4.2.1 Pilot Estimation of Cone Photoreceptors

Given an image $\boldsymbol{I}_c^{orig} \in \mathbb{R}^{150\times150}$, we first brighten dim photoreceptors using

$$\boldsymbol{I}_c^{full} = \text{LinNorm}(\ \log(\ \text{LinNorm}(\boldsymbol{I}_c^{orig},\ 0.1,\ 0.9)\ ),\ 0,\ 1). \tag{4.1}$$

The range 0.1 to 0.9 was chosen to increase the contrast between the dimmest and brightest pixels, as well as to avoid the log(0) and log(1) computations. We then determine cone pilot estimates by finding local maxima using imregionalmax($\boldsymbol{I}_c^{full}, 4$) in MATLAB. This results in the binary image $\boldsymbol{B}_c^{full}$ where values of 1 correspond to pilot estimates of cones.

We then analyze individual cones by order of decreasing intensity, where $\boldsymbol{I}_c^{full}$ and $\boldsymbol{B}_c^{full}$ are cropped about the centroid of the cone's pilot estimate to generate $\boldsymbol{I}_c$ and $\boldsymbol{B}_c \in \mathbb{R}^{21\times21}$; cropping the images enables a faster computation time, and the ten pixel buffer on all sides of the centroid ensures that the target cone is not cropped

out of $\boldsymbol{I}_c$. Pilot estimates for other cones contained within $\boldsymbol{B}_c$ are removed, and the remaining cone estimate in $\boldsymbol{B}_c$ is refined using thresholding. The new pilot estimate consists of connected pixels in $\boldsymbol{I}_c$ ranging from $0.95\boldsymbol{I}_{max}$ to $\boldsymbol{I}_{max}$ in intensity, where $\boldsymbol{I}_{max}$ is the maximum intensity in $\boldsymbol{I}_c$ that coincides with $\boldsymbol{B}_c = 1$, and $0.95\boldsymbol{I}_{max}$ was determined empirically to avoid thresholding adjacent cones.

4.2.2 Quasi-Polar Transform and GTDP Segmentation

To segment each cone, we first use our quasi-polar transform described in Section 2.2.2) to transform $\boldsymbol{I}_c$ to $\boldsymbol{I}_q$. To do this, we transform $\boldsymbol{I}_c$ and $\boldsymbol{B}_c$ (Figures 4.2A-B) into the polar domain to create $\boldsymbol{I}_p$ and $\boldsymbol{B}_p$ (Figures 4.2C-D). Next, we column-wise shift $\boldsymbol{I}_p$ until the pilot estimate in $\boldsymbol{B}_p$ is flat, resulting in the quasi-polar images $\boldsymbol{I}_q$ and $\boldsymbol{B}_q$ (Figures 4.2E-F). After obtaining $\boldsymbol{I}_q$, we remove regions containing other pilot estimates and already-segmented cones from the search space, and use layer-based GTDP (Section 2.1) to find the shortest path across $\boldsymbol{I}_q$ with weights following

$$\begin{aligned} \omega_{ab} =& \text{LinNorm}(-g_a^{LD} - g_b^{LD},\ 1,\ 2) + \\ & \text{LinNorm}(-g_a^{DL} - g_b^{DL},\ 0,\ 0.1) + \\ & \text{LinNorm}(d_{ab},\ 0,\ 0.05)\ +\ \omega_{min}, \end{aligned} \tag{4.2}$$

where d_{ab} is the Euclidean distance from node a to b and the rest of the variables are defined in Section 3.2.2. The vertical light-to-dark gradient comprises the majority of the weight since it is the primary indicator for the boundary of the central cone. A smaller weight is given to the dark-to-light gradient to segment boundaries of dimmer cones adjacent to brighter cones (Figure 4.2C, left). Finally, a vertical distance penalty is added to discourage the segmented line from including adjacent cones. Specific values for weight ranges were determined empirically.

We then transform the shortest path from the quasi-polar domain (Figure 4.2G) back into the Cartesian domain following Equation (2.6) to obtain the final segmen-

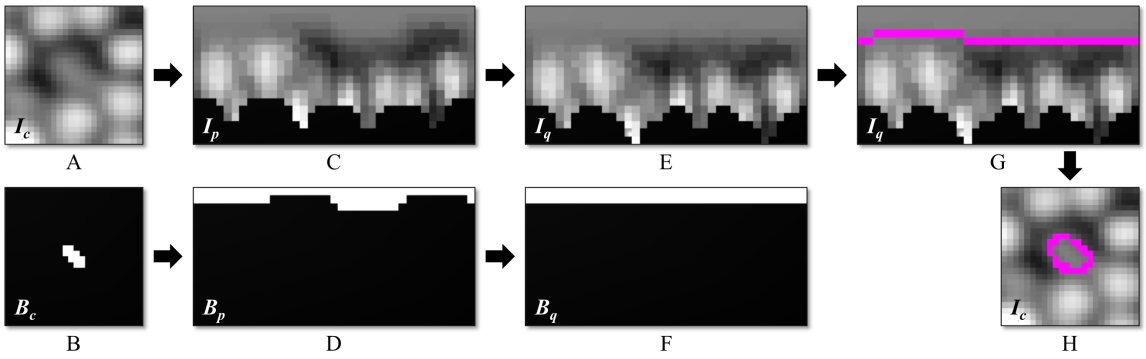

FIGURE 4.2: Cone photoreceptor segmentation using the quasi-polar transform and GTDP. (A) Cartesian image containing the cone to segment. (B) Pilot estimate of the cone in A. (C,D) Polar transformation of A and B, respectively. The black regions in C are invalid points that lie outside the image in the Cartesian domain. (E,F) Images C and D column-wise shifted until the pilot estimate in D is flat. (G) Segmentation of E using GTDP (magenta). (H) Transformation of the segmentation in G back into the Cartesian domain (magenta).

tation of the cone (Figure 4.2H), keeping it only if the mean radius is greater than one pixel. This entire process is then repeated for all subsequent cone estimates.

4.2.3 Segmentation of Missing Cones

At this stage of the algorithm, the cones identified and segmented by the GTDP method (Figure 4.3B, black) may be similar to those detected by previous methods, since local maxima are used to initialize the cone locations. To further identify any missed cones, we obtain pilot estimates of the cones using a second method: image deblurring using maximum likelihood blind deconvolution [140–142] (deconvblind function in MATLAB) with a Gaussian point spread function of half the mean radius of already segmented cones, followed by locating all regional maxima with a pixel connectivity of $n = 8$. Any pilot estimates lying outside already-segmented cone locations (Figure 4.3A, white boxes) are segmented using the same quasi-polar GTDP

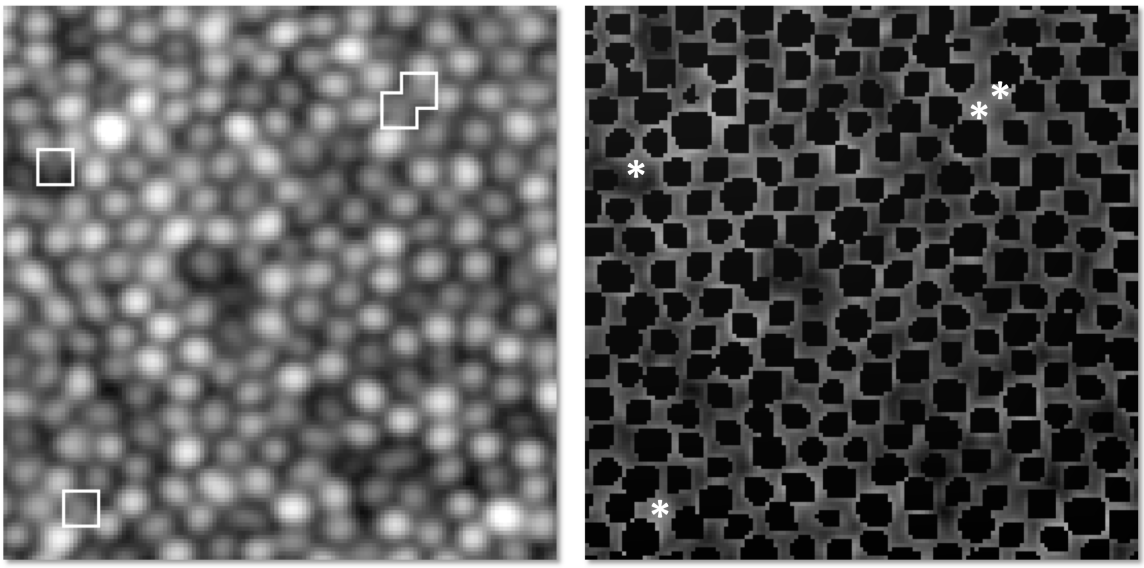

FIGURE 4.3: Identification of cones missed by local maxima. (A) AOSLO image in log scale with missed cones shown inside the white boxes. (B) Cone photoreceptors segmented using local maxima initialization in black, and pilot estimates of missed cones found using deconvolution and local maxima are shown in white asterisks.

technique, with modifications to the weighting matrix where

$$\begin{aligned}\omega_{ab} =& \text{LinNorm}(-g_a^{LD} - g_b^{LD},\ 1,\ 2) + \\ & \text{LinNorm}(-g_a^{DL} - g_b^{DL},\ 1,\ 1.51)\ +\ \omega_{min}.\end{aligned} \tag{4.3}$$

In this weighting scheme, the vertical dark-to-light gradient are assigned a higher weight since cones detected during this section iteration are typically dimmer and adjacent to brighter cones. The vertical distance penalty is also removed since adjacent cones are already segmented and thus removed from the search region. Figure 4.3B shows the cones that were found and segmented using this method (white asterisks).

4.3 Preliminary GTDP Rod-Cone Photoreceptor Segmentation Algorithm

To illustrate the potential of this algorithm to segment images containing both rods and cones, we modified the cone segmentation algorithm described in Section 4.2 to

segment a rod and cone photoreceptor image $\boldsymbol{I}_c^{full} \in \mathbb{R}^{250\times250} \rightarrow \mathbb{R}^{578\times578}$ at 0.186 µm per pixel captured using the new generation of AOSLO systems [129, 143]. In this modified version of the algorithm, photoreceptors are segmented in the quasi-polar domain with weights following

$$\begin{aligned}\omega_{ab} =&\text{LinNorm}(-g_a^{LD} - g_b^{LD},\ 1,\ 2) + \\ &\text{LinNorm}(i_a + i_b,\ 0.1,\ 0.2) + \\ &\text{LinNorm}(r'_a + r'_b,\ 0,\ 0.05) + \\ &\text{LinNorm}(d_{ab},\ 2,\ 2.1)\ +\ \omega_{min},\end{aligned} \tag{4.4}$$

where i_n is the intensity of $\boldsymbol{I}_q$ at node n and r'_n is the distance of node n from the top of $\boldsymbol{I}_q$ (also the row of node n). These additional weights are included to target the location of minimum intensity rather than the maximum gradient, and to penalize peripheral photoreceptors from being segmented.

Segmentations with radii less than 3.72 µm were considered to be rods, and the rest were re-segmented with the weighting scheme in Equation (4.5) to isolate cones. The r'_n distance penalty was removed since cones have larger radii than rods, and the g_n^{LD} weights were removed to delineate the prominent hypo-reflective region surrounding cones on AOSLO rather than the high gradient boundary.

$$\begin{aligned}\omega_{ab} =&\text{LinNorm}(i_a + i_b,\ 0.2,\ 1) + \\ &\text{LinNorm}(d_{ab},\ 0,\ 0.1)\ +\ \omega_{min}\end{aligned} \tag{4.5}$$

4.4 Validation Methods

4.4.1 Image Dataset

We validated our algorithm on 840 images (150 × 150 pixels) from the Garrioch *et al.* study [139] where the methods for image acquisition and pre-processing are described in detail. To summarize, the right eye of 21 subjects (25.9 ± 6.5 years in age, 1 subject with deuteranopia) was imaged using a previously described AOSLO

system [24, 129] with a 775 nm super luminescent diode and a $0.96 \times 0.96^{\circ}$ field of view. Four locations 0.65° from the center of fixation (bottom left, bottom right, top left, and top right) were imaged, capturing 150 frames at each site. This process was repeated 10 times for each subject. Axial length measurements were also acquired with an IOL Master (Carl Zeiss Meditec, Dublin, CA, USA) to determine the lateral resolution of the captured images.

Following image acquisition, pre-processing steps were taken in the Garrioch *et al.* study to generate a single registered image from each 150 image sequence. To do this, first any sinusoidal distortions from the resonant scanner were removed from individual frames. The frames from each sequence were then registered to a reference frame [144], and the top 40 frames with the highest normalized cross correlation to the reference were averaged together. This procedure was performed for all 21 subjects at each of the 4 locations and repeated 10 times over, resulting in a total of 840 images in the image data set. Finally, to ensure that each set of 10 repeated images captured the same patch of retina, the images were aligned using strip registration.

Since the image dataset was used strictly for algorithm validation, we obtained a separate set of images to tune the algorithm. These training images were captured using the same imaging protocol, and patients from the test and validation data sets did not overlap.

4.4.2 Gold Standard for Cone Identification

We defined the gold standard as the semi-automatically identified cone locations reported in the Garrioch *et al.* study, since the cone locations on all 840 images had been carefully reviewed and corrected by an expert grader. As described in the study, the initial cone coordinates were first automatically generated using the Garrioch *et al.* 2012 algorithm, a modified version of the Li & Roorda 2007 cone identification algorithm [102]. Any missed cones were then added manually. Automatically seg-

mented cones were not removed or adjusted, as the Garrioch *et al.* 2012 algorithm exhibited a tendency towards false negatives rather than false positives.

4.4.3 Statistical Algorithm Validation

We validated our GTDP algorithm by comparing its performance to the Garrioch *et al.* 2012 algorithm and to the gold standard generated by the Garrioch *et al.* paper [139]. To perfectly replicate the Garrioch *et al.* study, all images were cropped to a 55 µm × 55 µm region about the image center to remove any boundary effects.

To evaluate the performance in cone identification, we compared both fully automatic methods (GTDP and Garrioch *et al.* 2012) to the gold standard using two metrics: number of true positives (TP), N_{TP}, those detected by both the fully automatic and gold standard techniques, and number of false positives (FP), N_{FP}, those detected by the fully automatic method but not by the gold standard. A cone was considered to be a true positive if it was within a 1.75 µm Euclidian distance from a gold standard cone. This value was chosen since the mean cone spacing reported in the Garrioch *et al.* study was approximately 3.50 µm; half this value was therefore a reasonable estimate for the cone radius. If an automatically identified cone did not have any gold standard cones within the 1.75 µm distance, then it was tagged as a false positive. Furthermore, more than one automatically identified cone could not be matched to a single gold standard cone, thus yielding the following relationships:

$$\begin{aligned} N_{\text{automatic cones identified}} &= N_{TP} + N_{FP} \\ N_{\text{gold standard cones identified}} &= N_{TP} + N_{FN}, \end{aligned} \tag{4.6}$$

where N_{FN} was the number of false negative (FN) cones detected by the gold standard but not by the fully automatic method. The proportion of true and false positives were then estimated with 95% confidence intervals (CI) across all patients and all quadrants using a generalized estimating equation model with log link [145].

The reproducibility of each method was assessed by comparing *cone density* (number of cones per mm^2) and *cone spacing* (mean distance from each cone to its nearest neighbor) measurements output by each method at each quadrant. The variability in cone density and spacing measurements (characterized by the variance V_{total}) stemmed from two sources: 1) variability in measurements taken on the same subject, resulting from the method used (within-subject variability; variance V_{within}), and 2) variability in true values between subjects, resulting from biological variation between subjects (between-subjects variability; variance $V_{between}$). Thus, $V_{total} = V_{within} + V_{between}$. The reproducibility was characterized using two components: 1) within-subject coefficient of variation (CV), and 2) intra-class (or intra-subject) correlation coefficient (ICC). The within-subject CV was defined as the ratio of the square root of V_{within} to the overall mean measurement, where a lower CV indicates a better the method. ICC was defined as the ratio of $V_{between}$ to V_{total}, thus a ratio closer to 1 indicates a better method.

4.5 Validation Results

Section 4.5.1 discusses the segmentation results of our method, while Sections 4.5.2 and 4.5.3 show quantitative results comparing the performance of our method against the state-of-the-art for cone identification and cone density and spacing reproducibility, respectively. Finally, Section 4.5.4 shows a preliminary segmentation result for an image containing both rod and cone photoreceptors.

4.5.1 Cone Segmentation Results

Figure 4.4B (top) is a representative segmentation result generated by our GTDP algorithm to segment cone photoreceptors in AOSLO images, and Figure 4.4C (top) shows the centroid of each segmented cone. While the GTDP algorithm delineated the perceived cone boundaries, we used the result in Figure 4.4C to validate our

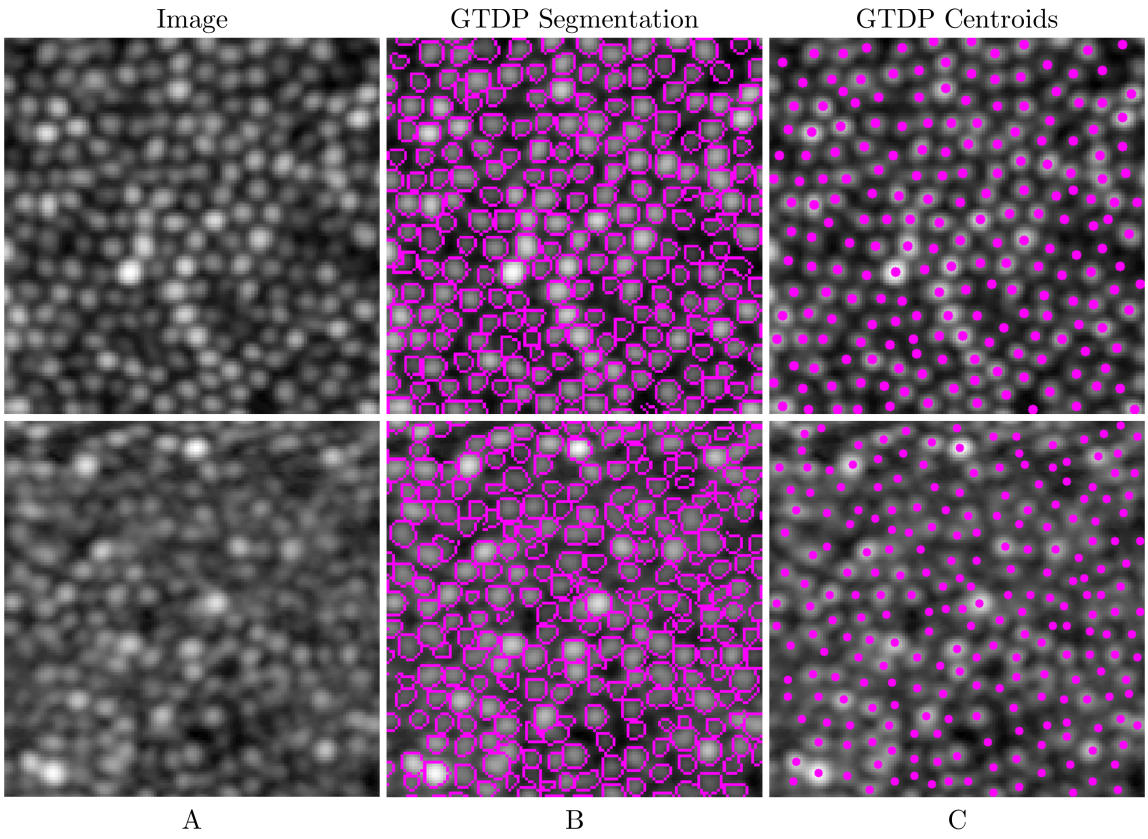

FIGURE 4.4: Qualitative GTDP cone segmentation result. *Top row:* (A) Higher quality AOSLO image of cone photoreceptors in log scale, (B) fully automatic segmentation result of A using GTDP for closed-contour structures, and (C) centroid of each fully automatically segmented cone from B. *Bottom row:* (A) Lower quality AOSLO image, (B) the GTDP segmentation result, and (C) corresponding centroids.

algorithm against other cone identification techniques. Figure 4.4 (bottom) shows the segmentation result for an image of lower quality.

The entire validation dataset and the corresponding GTDP, Garrioch *et al.* 2012, and gold standard segmentation results are available at `http://www.duke.edu/~sf59/Chiu_BOE_2013_dataset.htm`. The fully automated algorithm was coded in MATLAB and had an average computation time of 1.56 seconds per image (150 × 150 pixels, an average of 300 cones per uncropped image) using 8-thread parallel processing on a laptop computer with a 64-bit operating system, Core i7-820QM

Table 4.1: Cone identification performance of fully automatic methods compared to the gold standard across 840 images.

Algorithm	**%TP (95% CI)***	**%FP (95% CI)**
Garrioch *et al.* 2012	94.5 (93.7, 95.2)	–
GTDP	99.0 (98.8, 99.2)	1.5 (1.2,1.9)

* statistically significant

CPU at 1.73 GHz (Intel, Mountain View, CA, USA), 7200 RPM hard drive, and 16 GB of RAM. This time included the overhead required for reading and writing operations.

4.5.2 Cone Identification Performance

The performance in cone identification for each of the methods is shown in Table 4.1. This table shows that after taking into consideration all correlated data, our GTDP method correctly detected 99.0% of the cones, compared to the Garrioch *et al.* 2012 method which detected 94.5% of the gold standard cones; this difference was found to be significant ($Z = 15.0, p < 0.0001$). In addition, 1.5% of the cones found by the GTDP method were not in the gold standard. False positive cones could not be detected by the Garrioch *et al.* 2012 method since the gold standard was based off of the Garrioch *et al.* 2012 algorithm. Lastly, the mean distance error from the true positive GTDP cones to the gold standard cones was 0.20 ± 0.26 µm.

Figure 4.5 is an illustrative example of the cone identification results, where Figure 4.5B shows the mean cone identification performance for both automatic algorithms, while the Figures 4.5A and C show the performance approximately one standard deviation above and below the mean, respectively. The middle column displays the Garrioch algorithm *et al.* 2012 results, with true positives in yellow and false negatives in green. The right column shows the GTDP results, with true positives in magenta, false negatives in green, and false positives in blue. The performance (%TP by Garrioch *et al.* 2012; %TP by GTDP; %FP by GTDP) for

Figure 4.5A-C were (100; 98.4; 0), (99.1; 94.4; 2.1), and (97.5; 90.4; 3), respectively.

Finally, Figure 4.6 takes a closer look at the results from Figure 4.5B (right). The black boxes highlight "false positive" cones added by the GTDP algorithm per the gold standard, however inspection of the original image in Figure 4.6A indicates that cones are indeed present at those locations. In contrast, the white boxes in Figure 4.6 highlight "false negative" cones missed by the algorithm per the gold standard. However, by inspecting Figure 4.6A, these locations do not seem to exhibit hyper reflectivity.

4.5.3 Reproducibility Results

Table 4.2 shows the mean, ICC, and within-subject CV values for the cone density and spacing metrics as measured by the Garrioch, GTDP, and gold standard methods separated by image quadrant. The average GTDP cone density ICC of 0.989 indicates that on average, 98.9% of the total variability in the measurements was due to the variability between subjects, while only 1.1% was due to the GTDP algorithm. The average GTDP within-subject CV of 0.0146 indicates that the error in reproducing the same measurement for the same subject was within 1.46% of the mean.

4.5.4 Preliminary Rod-Cone Segmentation Result

Figure 4.7A shows an example rod and cone photoreceptor image [129, 143] accompanied by the GTDP segmentation result in Figure 4.7B and its associated centroids in Figure 4.7C. Figure 4.7D shows a histogram of the number of photoreceptors at various sizes based on the segmentation from Figure 4.7B, and Figure 4.7E demonstrates a straightforward classification of rod and cone photoreceptors using a size threshold of 27.7 μm^2.

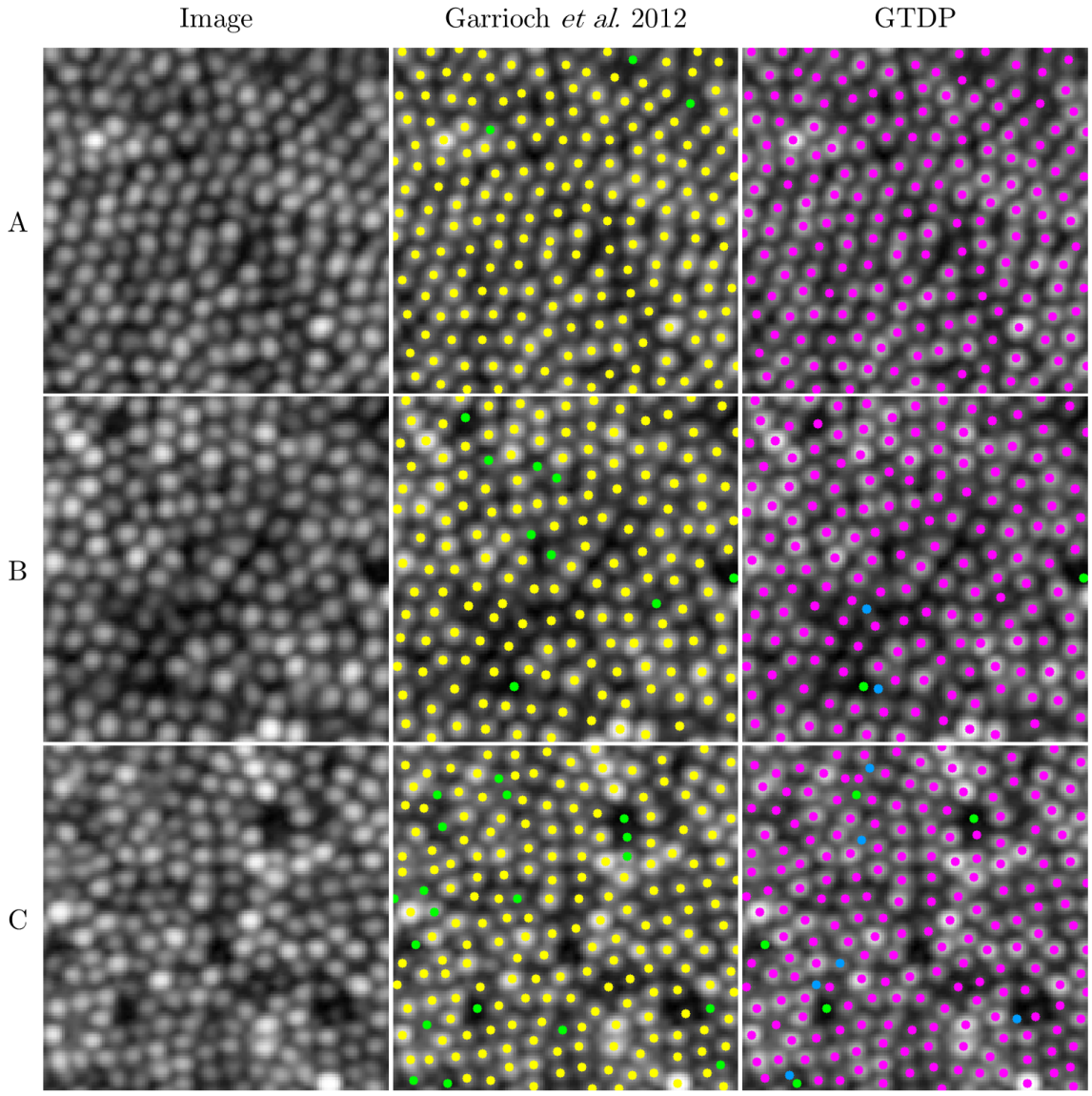

FIGURE 4.5: Variable performance of the fully automatic cone identification algorithms. *Left column:* AOSLO image of the cone mosaic in log scale. *Middle column:* Garrioch *et al.* 2012 algorithm results (TP: yellow, FN: green). *Right column:* GTDP algorithm results (TP: magenta, FN: green, FP: blue). (B) Typical (mean) performance by both algorithms. (A,C) Performance one standard deviation above and below the mean for both algorithms, respectively.

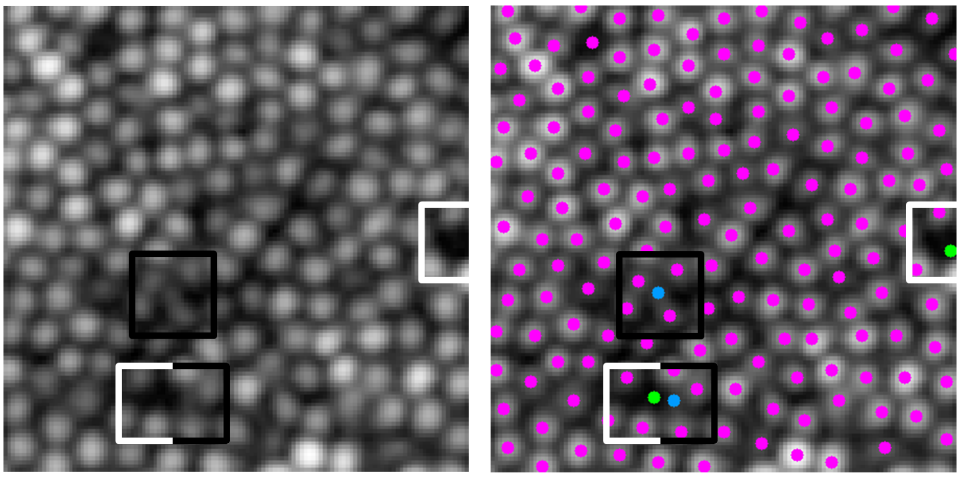

FIGURE 4.6: A closer look at the performance of the GTDP algorithm. (A) AOSLO image corresponding to Figure 4.5B, and (B) automatic GTDP segmentation result (TP: magenta, FN: green, FP: blue). *White boxes:* locations where the algorithm "missed" a cone, even though there appears to be no cone present. *Black boxes:* locations where the algorithm "erroneously added" a cone, although the original image seems to contain additional cones not identified by the gold standard.

4.6 Discussion

We obtained the dataset from the Garrioch *et al.* study [139] to validate the performance of our algorithm on a large untrained dataset. We compared the performance of our fully automatic cone segmentation algorithm to the state-of-the-art technique, and found that our GTDP method decreased the Garrioch *et al.* 2012 cone miss rate by a factor of 5.5 (Table 4.1, 1.0% vs. 5.5% FP). One point five percent of the cones not identified by the gold standard were also found using our technique. While this implies that our algorithm falsely identified these cones, Figure 4.6 shows that in some cases, our GTDP method was able to identify cones not found by the gold standard; such observations, while not the norm, are likely due to the resource intensive nature of semi-automatic cone identification.

The mean results in Table 4.2 indicate that the cone density and spacing metrics

Table 4.2: Reproducibility comparison of cone density and spacing measurements.

	Cone Density			Cone Spacing		
Fixation Location	Mean (cones/mm^2)	ICC	Within-Subject CV	Mean (µm)	ICC	Within-Subject CV
Garrioch						
Bottom left	67,207	0.979	0.0217	3.50	0.989	0.0074
Bottom right	66,812	0.972	0.0253	3.50	0.983	0.0087
Top left	70,928	0.950	0.0272	3.37	0.975	0.0090
Top right	69,192	0.970	0.0273	3.39	0.984	0.0093
Average	68,534	0.968	0.0254	3.44	0.983	0.0086
GTDP						
Bottom left	70,796	0.993	0.0121	3.42	0.978	0.0110
Bottom right	70,783	0.989	0.0149	3.40	0.964	0.0131
Top left	75,485	0.988	0.0133	3.28	0.960	0.0124
Top right	74,216	0.985	0.0181	3.29	0.957	0.0154
Average	72,820	0.989	0.0146	3.35	0.965	0.0130
Gold standard						
Bottom left	70,577	0.995	0.0101	3.45	0.981	0.0097
Bottom right	70,204	0.994	0.0111	3.44	0.975	0.0106
Top left	75,416	0.994	0.0103	3.31	0.968	0.0113
Top right	73,914	0.995	0.0109	3.32	0.985	0.0090
Average	72,528	0.994	0.0106	3.38	0.977	0.0101

extracted by the GTDP method were more accurate on average than the Garrioch *et al.* 2012 algorithm, despite the bias where the Garrioch *et al.* results were used as the starting point for generating the gold standard. While an unbiased comparison could have been conducted, this would have required a fully manual identification of nearly 256,000 cones. Table 4.2 also shows that the GTDP method generated more reproducible cone density measurements (mean 0.0146 CV) than the other automated method (mean 0.0254 CV). To be consistent with previous publications, we also compared reproducibility in cone spacing, which showed that the Garrioch *et al.* 2012 method produced more reproducible results (mean 0.0086 CV) compared to both the GTDP method (mean 0.0130 CV) and the gold standard. This is because both the GTDP method as well as the gold standard detected more cones; these were

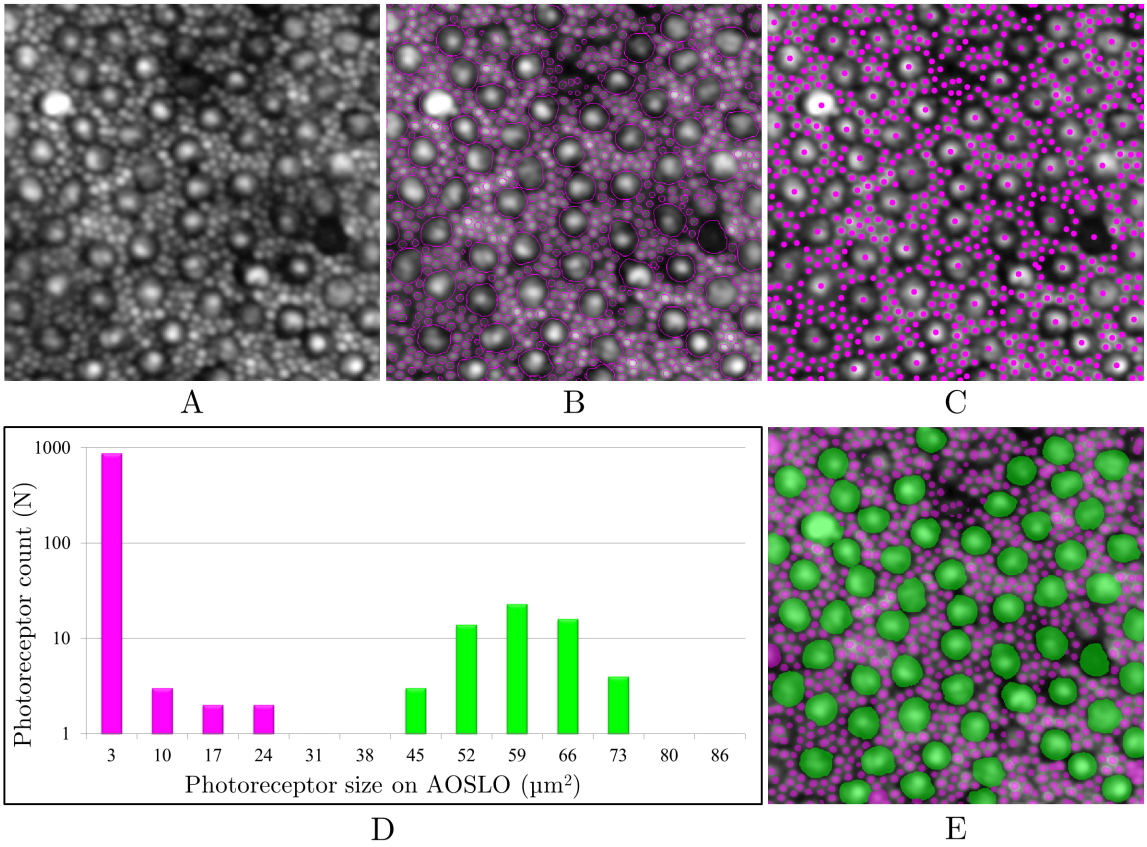

FIGURE 4.7: Fully automatic identification of rod and cone photoreceptors. (A) AOSLO image of rod and cone photoreceptors in log scale (image taken from [143]). (B,C) Fully automatic segmentation and identification of rods and cones using GTDP for closed-contour structures. (D) Histogram of the segmentations from B. (E) Threshold of 27.7 µm^2 used to classify the photoreceptors from D into rods (magenta) and cones (green).

typically the harder and more irregularly spaced cones, and thus resulted in more variable cone spacing. As a result, cone spacing reproducibility might not be the most reliable quantitative measure of performance. Nevertheless, all three methods had a very good within-subject CV, showing that the within-subject standard error (error due to method) ranged by only 0.74% to 2.73% from the mean. Furthermore, all three methods had a very good ICC, showing that 95% to 99.5% of the total variability in the measurements was due to variability between subjects, while only 0.5% to 5% was due to the method. This high ICC was a result of the pre-processing

image alignment performed in the Garrioch *et al.* study to ensure that the same patch of retina was imaged.

A notable difference and novelty of the GTDP algorithm as compared to existing *en face* cone segmentation algorithms is its use of segmentation to identify cones. While the most common technique for cone identification is to locate points of maximal intensity, such a method only locates cone centers. In contrast, our technique delineates cone boundaries, resulting in added information about the size and shape of the segmented object. This information may be helpful for applications such as studying how the multimodal structure of larger cones changes with time or wavelength. However, it is of importance to note that in the context of AO photoreceptor imaging, cone sizes may be near the resolution limit, especially towards the foveal center. Furthermore, estimation of photoreceptor size depends on the wavelength of the imaging modality (e.g. fundus camera, SLO, OCT) and even varies over time based on intensity fluctuations. As a result, extracting size and shape information about the cones, while helpful, may not be an accurate indication of its true morphologic state.

Another advantage of using segmentation is that it enables a higher cone detection rate. By keeping track of the entire area of a cone rather than only its centroid, we can look for additional cones in regions where cones have not yet been found (Figure 4.3B). Our technique also provides an advantage for isolating rods and cones within a single image (Figure 4.7E), as we can readily distinguish between the two types of photoreceptors based on their segmented area in normal retinae. However, since accurate photoreceptor classification depends on correctly segmented photoreceptors, the rods improperly segmented as cones in Figure 4.7B resulted in misclassification. A more accurate and robust rod-cone segmentation algorithm moving forward will be essential to improving this preliminary classification result.

A limitation of this study is its rather optimistic validation on higher quality

images of normal retina. In contrast, AO images taken from diseased retinae are often low in quality and plagued with diverse pathological features. Nonetheless, this work is the first step in introducing a conceptually simple yet robust framework adaptable to incorporating the mathematical and algorithmic innovations necessary for segmenting the more challenging real-world, clinical AOSLO images. Future steps include validation of our rod and cone segmentation algorithm, as well as extension and application of our framework to segment more complicated images of photoreceptors in disease states.

4.7 Summary

We developed a fully automatic algorithm using GTDP to segment cone photoreceptors in AOSLO images of the retina and validated its performance. We were able to achieve a higher cone detection rate, more accurate cone density and spacing measurements, and comparable reproducibility compared to the Garrioch *et al.* 2012 algorithm. Furthermore, the segmentation-based approach enabled identification and classification of rods and cones within a single image. This is encouraging for ophthalmic studies requiring an efficient and accurate analysis of the photoreceptor mosaic.

5

Clinical Application: OCT Biomarkers of AMD

5.1 Motivation

Age-related macular degeneration is a leading cause of irreversible blindness in Americans over 60 years of age [146]. There are many unanswered questions regarding the pathogenesis of AMD, which can be investigated in longitudinal studies using *in vivo*, high-resolution, cross-sectional imaging rather than color fundus photographs [147, 148]. The non-invasive, cross-sectional view of the retina from SD-OCT imaging has been used to characterize the vitreoretinal interface, retina, RPE, and drusen complexes in the presence of AMD [147–149]. For quantitative AMD studies, segmentation of the retina into layers and measurement of drusen volume are crucial.

For non-neovascular AMD, disease severity can be determined by quantifying drusen [150, 151] and geographic atrophy (GA) [152, 153]. Traditionally, methods for drusen quantification rely on the evaluation of 2D fundus photographs, where many algorithms have been developed to accelerate segmentation [97, 154–157]. With the advent of OCT, a third (axial) dimension of data has proven to be

advantageous for drusen detection [148]. While many have demonstrated quantitative accuracy in drusen volume quantification with either manual or semi-automatic techniques [149, 158], most fully-automatic methods only show proof-of-concept results [47, 54, 159–161] and very few have been validated for accuracy [162]. Furthermore, drusen identification by commercial software integrated into several SD-OCT systems has shown distinct limitations [163]. Such shortcomings have raised interest in the utilization of polarization-sensitive OCT (PS-OCT) systems [164] to directly segment the RPE [165]. Lastly, while several techniques for neovascular AMD segmentation have also been recently proposed [89, 166–168], we target imaging intermediate AMD prior to advanced disease.

In addition to the complexities associated with developing fully-automatic segmentation algorithms, uncertainties over the true boundary locations of evolving pathologic structures in retinal SD-OCT images pose yet another challenge. Reaching a consensus on these boundaries is often not a trivial task. For example, when assessing the RPE on SD-OCT images with AMD pathology, the presence of drusen and GA significantly complicates the RPE structure, especially in instances of subretinal drusenoid deposits [169–171] and irregular structures such as hyper-reflective foci [149] or drusen remnants over GA [172]. This results in an often subjective or arbitrary delineation of the RPE layer.

In this chapter, we propose guidelines for identifying the retinal layers that are indicative of AMD progression, including the neurosensory retina (NSR) and the RPE+drusen complex (RPEDC). To isolate these layers, we define boundaries at the inner aspect of the ILM, inner aspect of the RPEDC, and outer aspect of BM (Figure 5.1). We then describe an algorithm that automatically segments these layer boundaries using the GTDP framework described in Section 2.1. Finally, the algorithm is validated for its accuracy and reproducibility in quantifying the NSR and RPEDC layers.

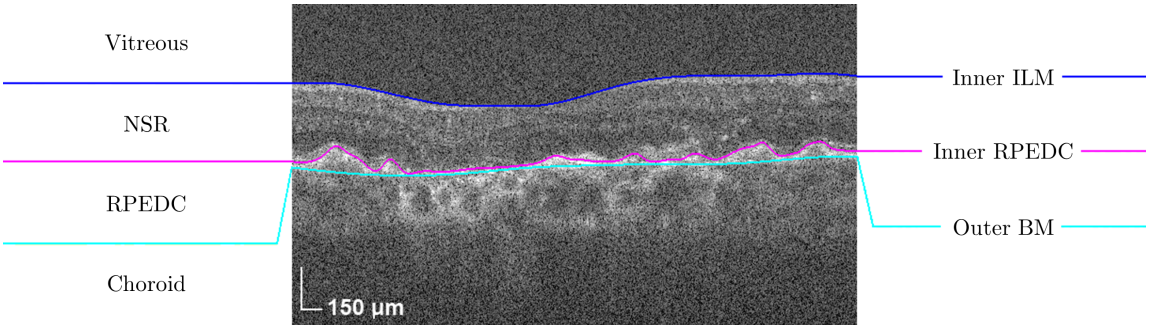

FIGURE 5.1: Manual segmentation of an unsummed SD-OCT image for an eye with intermediate AMD, delineating the inner aspect of the ILM (blue), inner aspect of the RPE+drusen complex (RPEDC) (magenta), and outer aspect of BM (cyan). Note the exclusion of the photoreceptor outer segments from the RPEDC layer and the near convergence of the RPEDC at the site of focal geographic atrophy.

5.2 Proposed Manual Segmentation Guidelines for AMD Pathology

Prior to manual segmentation and algorithm development, we constructed a set of qualitative guidelines based on previous literature, expertise from the Duke OCT Reading Center, and representative images, to trace layer boundaries on images with non-neovascular AMD pathology. Guidelines and example images were used as a reference for manual segmentation in order to maintain a consistent and unbiased interpretation between certified graders. Practice sessions for manual segmentation were also performed on training data sets based on the guidelines. These guidelines are listed as follows:

1. *We isolate the RPE and drusen complex (denoted RPEDC) by delineating the inner aspect of the RPE plus drusen material and the outer aspect of BM.*

   Sarks *et al.* have shown progression in AMD by correlating basal linear and basal laminar deposits of the RPE to greater amounts of membranous debris associated with clinically evident drusen and pigmentary changes on color funduscopic measurements [173]. More recently, Zweifel *et al.* have shown subretinal deposits in reticular drusen [174]. Thus, in particular for macular

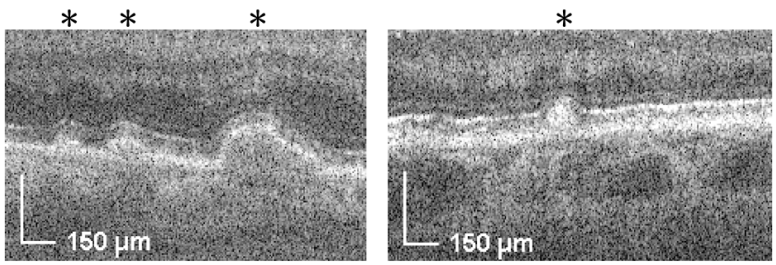

A B

FIGURE 5.2: Example features to include in the RPEDC for eyes with intermediate AMD. (A) Sub-RPE drusen (under asterisks) and (B) a subretinal drusenoid deposit (under asterisk), both of which are included in the RPEDC.

SD-OCT datasets with non-neovascular AMD, we believe that a measure of the RPEDC volume containing all drusen material, whether above (Figure 5.2B) or below the RPE (Figure 5.2A), would be a more useful measure of disease. Such a metric, which includes the RPE and small deposits of drusen material rather than only large collections of debris, should therefore differentiate normal aging from pathologic AMD processes. This hypothesis will be tested in the longitudinal AREDS2 Ancillary SD-OCT (or A2A SD-OCT) study with age-matched controls. Our hope is to show that RPEDC volume can be a useful metric for assessing earlier states of AMD by differentiating the earliest stages of disease from normal aging of the RPE.

2. *We include all hyper-reflective material contiguous with the RPE as part of the RPEDC, excluding the following:*

   (a) *Material over a nearly absent RPE with a width narrower than the azimuthal resolution (Figure 5.3B).*

   (b) *Indistinguishable dim or shadowy features over a nearly absent RPE (Figure 5.3C).*

   We include all forms of drusen, such as sub-RPE drusen (Figure 5.2A)

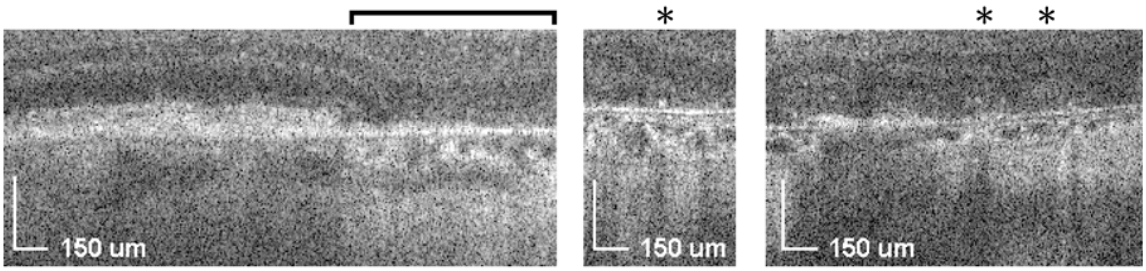

FIGURE 5.3: Example features to exclude from the RPEDC in eyes with GA. (A) A nearly absent RPE with hyper-reflectivity in the choroid (under bar) is typical of GA. Note the loss of the photoreceptor layer in this region. (B) Material over such a region with a width narrower than the azimuthal resolution (under asterisk) is not considered a component of RPEDC, and (C) indistinguishable dim or shadowy features (under asterisks) over such a region are also not considered a component of RPEDC. We require the presence of A to exclude the features in B and C from the RPEDC, and we use hyper-reflectivity in the choroid as a supporting indicator the presence of A.

and subretinal drusenoid deposits (Figure 5.2B), in the RPEDC due to the implications outlined in Guideline 1. While hyper-reflective foci have been suggested to indicate disease progression [149], we chose not to include these foci as part of the RPEDC because they represent cells that have migrated away from (and are not contiguous with) the RPE. The inner border of the RPEDC was distinguished from the overlying hyper-reflective ISE band when present, as demonstrated in Figure 5.1.

We do not include narrow particulate (Figure 5.3B) or dim material (Figure 5.3C) over regions where the RPE is nearly absent (Figure 5.3A) since they may represent residual drusen material or degenerated neurosensory cells [172]. To determine whether the RPE is nearly absent, we qualitatively assess the thickness of the RPE and utilize hyper-reflectivity in the underlying choroid as a supporting indicator of GA [153, 175].

For small, particulate material, we selected the minimum resolution to be

FIGURE 5.4: Flowchart of the GTDP algorithm for segmenting SD-OCT retinal layers of eyes with intermediate AMD.

equivalent to the azimuthal resolution to attain isotropic resolution, because in our experiments the azimuthal resolution was lower than the lateral and axial resolutions. In this chapter, 67 µm was used as the minimum resolution.

5.3 AMD Retinal Layer Segmentation Algorithm

We developed a three-retinal layer boundary segmentation algorithm for SD-OCT images with AMD pathology based on the GTDP framework implemented for normal retina in Chapter 3 [57]. An outline of the new algorithm flow in Figure 5.4 highlights the key components needed to adapt this method for images with drusen and GA, and an overview of the steps involved are described in the subsequent paragraphs. Further information about the image dataset is given in Section 5.4.1.

5.3.1 Image Downsampling

To reduce the overall computation time, we first downsample the image by a factor two in both dimensions using bicubic interpolation and antialiasing. This step can be ignored for images with low-resolution, or if the computational complexity is of no concern.

5.3.2 NFL-OPL and ISE-RPE Separation

There are two distinct hyper-reflective regions in filtered SD-OCT images of the retina: the region bounded by the ILM and OPL/ONL boundaries (denoted the NFL-OPL complex) and the region bounded by the ISM/ISE and BM boundaries

(denoted the ISE-RPE complex). For retinal images with AMD, the pathology may result in a merging of the NFL-OPL and ISE-RPE complexes. If these two regions are not separated prior to segmenting, then it is possible for the ILM and inner RPEDC boundaries to be mistaken for each other due to the similarity in their characteristics.

We therefore generate a binary mask of the image to isolate the NFL-OPL and ISE-RPE hyper-reflective complexes. This is done by smoothing the image with an 11×11 pixel Gaussian filter with a standard deviation of 11 pixels, extracting the edges using a $[-1, 1]^T$ high-pass filter, linearly normalizing the image to range from 0 to 1, generating a binary mask using a threshold of 0.5 on the normalized image, opening any gaps in the clusters using a 3×3 pixel structuring element, removing connected clusters smaller than 200 pixels, and closing any remaining gaps using the same structuring element.

Once the mask is generated, we delineate the boundaries of the two white bands corresponding to the two NFL-OPL and ISE-RPE complexes using GTDP. We generate two vertical gradient adjacency matrices: a black-to-white and a white-to-black matrix using the $[-1, 1]^T$ and $[1, -1]^T$ edge filters and setting all negative values to zero. After automatic endpoint initialization, we segment the four boundaries on the image. We achieve this by twice searching for a black-to-white edge to locate the upper boundaries of the two white bands, and twice searching for a white-to-black edge to locate the two lower boundaries of the white bands. In order to ensure the same edge is not segmented again, we exclude already-delineated nodes from the graph when cutting subsequent edges. The result is a pilot estimate of the ILM, OPL/ONL, inner RPEDC, and BM boundaries.

5.3.3 Flattening the Retina

Next, we flatten the retina based on the convex hull [176] of the estimated inner RPEDC boundary since it approximates BM. This is done by shifting the columns

of the image up or down until the estimated convex hull lies on a flat line. To prevent from introducing any new border artifacts, columns of the flattened image without pixel intensity information are assigned intensity values corresponding to the mirror image of the values in the valid regions of the same column.

5.3.4 GTDP Layer Segmentation

To segment the retinal layer boundaries using GTDP, we first create adjacency matrices based on the flattened image. To delineate the ILM, weights assigned to a dark-to-light adjacency matrix are calculated based on Equation (3.2). For BM, a separate adjacency matrix is utilized with weights calculated following

$$\begin{aligned}\omega_{ab} =&\text{LinNorm}(-g_a^{LD} - g_b^{LD},\ 2,\ 4) + \\ &\text{LinNorm}(-g_a^{DL} - g_b^{DL},\ 0,\ 0.2) + \\ &\text{LinNorm}(d_{ab},\ 2,\ 4)\ +\ \omega_{min}.\end{aligned} \tag{5.1}$$

Finally, for the inner RPEDC boundary, the dark-to-light adjacency matrix from Equation (3.2) is utilized along with a third adjacency matrix calculated based on image intensity where

$$\omega_{ab} = \text{LinNorm}(-i_a - i_b,\ 0,\ 1)\ +\ \omega_{min}. \tag{5.2}$$

Following Section 2.1, we automatically initialize the endpoints and segment the boundaries using Dijkstra's algorithm to find the shortest path. For the ILM, we use the dark-to-light adjacency matrix and a search region ranging from the top of the image to the inner RPEDC estimated from the binary mask in Section 5.3.2. To segment BM, we first tentatively cut the inner RPEDC using the dark-to-light adjacency matrix and a search region limited by the inner RPEDC and BM estimates from the binary mask. We then use the weights in Equation (5.1) and a search region with the inner RPEDC as the upper boundary.

To refine the inner RPEDC, we first estimate the RPE by segmenting it using the intensity-based adjacency matrix from Equation (5.2). We limit the search region to the inner RPEDC estimate and the final BM boundary. We then re-segment the inner RPEDC using the RPE as the lower boundary and 10 µm above the RPE as the upper boundary of the search region.

5.3.5 Unflattening and Upsampling

Lastly, we unflatten and upsample the segmentations by reversing the flattening and downsampling processes, resulting in the original retinal image with three automatically detected layer boundaries.

5.4 Validation Methods

5.4.1 Image Dataset

To validate our AMD retinal layer segmentation algorithm, we considered rectangular volumes with non-neovascular AMD under the A2A SD-OCT study, which was registered at clinicaltrials.gov (ClinicalTrials.gov Identifier: NCT00794498) and approved by the IRBs of the four A2A SD-OCT clinics (Devers Eye Institute, Duke Eye Center, Emory Eye Center, and the National Eye Institute (NEI)). Adhering to the tenets of the Declaration of Helsinki, informed consent was obtained from all participants.

In the A2A SD-OCT study, volumetric scans were acquired using the SD-OCT imaging systems from Bioptigen located at the four clinic sites. For each patient across all sites, horizontal (0°) and vertical (90°) rectangular volumes centered at the fovea with 1000 A-scans and 100 B-scans were captured for one eye. The scan sizes and the axial, lateral, and azimuthal resolutions varied slightly by site and are specified in Table 5.1. The eye length was not measured. For this study, we included volumes from all four clinical sites in order to validate algorithm performance for im-

Table 5.1: Bioptigen imaging resolutions varied by site. Rectangular volumetric scans were acquired with 1000 A-scans and 100 B-scans at all sites.

Imaging Resolutions	**Study Site**			
	Devers	**Duke**	**Emory**	**NEI**
Axial FWHM resolution in retina (µm)	4.54	4.38	4.56	4.56
Axial pixel resolution (µm/pixel)	3.21	3.23	3.06	3.24
Lateral resolution (µm/pixel)	6.60	6.54	6.58	6.50
Azimuthal resolution (µm/pixel)	68.2	67.0	69.8	65.0
Scan Width (mm)	6.60	6.54	6.58	6.50
Scan Length (mm)	6.82	6.70	6.98	6.50

ages acquired at slightly varying axial resolutions and by different clinical operators.

As part of the A2A SD-OCT study, each volume was graded for quality by graders certified by the Duke Advanced Research in SD-OCT Imaging (DARSI) group. In addition to an overall scoring of *good*, *fair*, or *poor*, they assessed these volumes for the following characteristics: a) foveal centration (a fovea located approximately at the center of the volume), b) presence of low resolution or saturation, c) presence of artifacts produced by subject blinking, d) presence of artifacts produced by eye motion or loss of fixation e) presence of complex conjugate artifacts, f) scan artifacts arising from the imaging system, g) tilt, clipping, or blank frames, and h) un-gradable. We utilized these existing scores in our study to classify the volumes as *high quality*, *low quality*, or *excluded from the study* based on the criteria in Table 5.2. For example, volumes with motion or loss of fixation artifacts could not be categorized as high in quality since they result in inaccurate retinal layer volume measurements. Likewise, we excluded volumes with blinking or complex conjugate artifacts in the region of interest to avoid validating B-scans with missing retinal data.

Based on the criteria from Table 5.3, we randomly selected a total of 25 volumes to validate the segmentation algorithm. The goal of the A2A SD-OCT study is to examine intermediate AMD; thus, we only considered volumes that were designated by the coordinating center to have Level 3 (intermediate) AMD based on color fundus

Table 5.2: The characteristics allowed for a particular volume quality. For example, a volume containing blinking artifacts could not be considered as a high or low quality volume, therefore it was excluded from the validation study. A volume exhibiting imaging system scan artifacts, on the other hand, did not impact volume quality.

	Volume Quality		
Allowable Characteristics	**High**	**Low**	**Excluded**
Pre-graded volume quality	good	good, fair	good, fair, poor
Low resolution or saturation		✓	✓
Blinking artifacts within frames 20-60			✓
Motion or loss of fixation		✓	✓
Complex conjugate artifact within frames 20-60			✓
Imaging system scan artifact	✓	✓	✓
Tilt, clipping, blank frames	✓	✓	✓
Un-gradable			✓

photography. Moreover, any volumes designated as Level 3 by fundus photography that exhibited Level 4 (advanced) pathology as seen on SD-OCT were excluded from the study. These included volumes with advanced AMD pathology such as choroidal neovascularization, serous pigment epithelial detachment, subretinal fluid, or GA at the foveal center. Vitelliform lesions were also excluded from the study since they represent subretinal material that is not drusenoid in nature. Lastly, of all 20 patients represented in the 25 selected volumes, seven patients were imaged at the Devers Eye Institute, three at the Duke Eye Center, six at the Emory Eye Center, and four at the NEI. All of the images used in this study and their corresponding manual and automatic segmentation data are available at `http://www.duke.edu/~sf59/Chiu_IOVS_2011_dataset.htm`.

5.4.2 Automatic versus Manual Segmentation

A total of 220 B-scans from 20 volumes were selected for this analysis. Five of these twenty volumes were comprised of one randomly selected volume from each patient in Group 1, and the remaining 15 volumes were those selected for Groups 2-4. The four groups are defined in Table 5.3. The 11 B-scans from each volume were chosen

Table 5.3: Validation study groups and volume selection criteria. All ten volumes selected for Group 1 were used in the Reproducibility analysis, while five volumes from each of the groups were used in the Automatic versus Manual Segmentation analysis.

Selection Criteria	**Volume Group**			
	1	2	3	4
Number of Patients	5	5	5	5
Number of Volumes per patient	2	1	1	1
Number of Total Volumes	10	5	5	5
Pathology Type	Drusen	Drusen	Drusen+GA	Drusen+GA
Volume Quality	High	Low	High	Low
Scan Orientation ($0^\circ/90^\circ$)	Both	Either	Either	Either

as follows, with F denoting the B-scan number containing the foveal center: F, F$\pm$2, F$\pm$5, F$\pm$10, F$\pm$15, and F$\pm$20.

Two DARSI-certified graders performed manual segmentation of the retina by drawing three layer boundaries (inner ILM, inner RPEDC, and outer BM) using customized software with a graphical user interface. During manual segmentation, no outside consultation or communication between graders was allowed. We then performed automatic segmentation using a MATLAB implementation of the algorithm.

Following segmentation, B-scans were cropped by 20% on each side to achieve equal axial and azimuthal lengths in the segmented volume. The mean thickness difference between the automatic and manual segmentation of a predetermined (the more senior) grader was calculated for each B-scan. The absolute mean difference and standard deviation across all B-scans were then computed and compared between the automatic and manual segmentation. We also determined the maximum error and the percentage of A-scans with an error > 5 pixels (note that the axial resolution varied by site, therefore the 5 pixels was not converted to the 15.3 - 16.2 µm range). The same comparison was then conducted between the two manual graders to estimate inter-observer variability.

5.4.3 Algorithm Reproducibility

We automatically segmented all B-scans in the 10 volumes from Group 1 using the developed software to delineate the inner ILM, inner RPEDC, and outer BM boundaries. Based on these segmentation results, we measured the volume of the RPEDC and NSR in microns for the region enclosed in a 4 mm-diameter circle centered at the fovea.

We chose a 4 mm-diameter circle to match the Automatic versus Manual analysis, where we examined the inner 60% of a 6.5 - 7.0 mm volume. Using the lateral and azimuthal resolutions of each volume, we summed the total number of pixels enclosed between the upper and lower boundaries of the layer across all A-scans within the circle to produce the pixel volume for the layer of interest. We calculated the micron volume of a pixel by multiplying the axial, lateral, and azimuthal resolutions from Table 5.1 and then multiplied the pixel volume by this factor. To determine the reproducibility of our segmentation algorithm, we compared the percent difference in the measured volumes between the 0° and 90° scans of the same eye at the same visit.

5.5 Validation Results

5.5.1 Automatic versus Manual Segmentation Results

Every image had at least one pixel of difference both between the manual segmentation by two graders and between automated versus manual segmentation. The mean and standard deviation of the segmented layer thickness differences are shown in Table 5.4 with the results categorized by volume group. Column III shows the layer thickness differences between two certified graders, and Column VI shows the differences of our automatic segmentation compared to the more senior grader. We also report the maximum thickness difference and the percentage of A-scans with an

Table 5.4: Automatic versus manual segmentation results. Differences (error) in retinal layer thickness segmentation between two certified manual graders for 220 B-scans (Column III), as compared to the thickness differences between the automatic segmentation and one certified manual grader of the same 220 B-scans (Column VI). The maximum difference and the percentage of A-scans with a difference greater than 5 pixels are also reported.

Volume Group	**Layer**	**Inter-Observer**			**Automatic vs Manual**		
		Mean±SD (µm)	Max (µm)	>5 pixels (%)	Mean±SD (µm)	Max (µm)	>5 pixels (%)
1	NSR	3.2 ± 2.3	40	5.5	2.5 ± 1.8	52	2.5
	RPEDC	4.1 ± 3.1	49	5.8	3.0 ± 2.1	52	3.2
2	NSR	3.3 ± 2.3	67	10.0	3.7 ± 2.3	67	7.6
	RPEDC	4.5 ± 3.5	70	12.5	2.8 ± 2.0	70	7.8
3	NSR	4.6 ± 3.9	103	12.8	5.0 ± 3.0	103	11.4
	RPEDC	4.8 ± 4.3	100	13.3	4.1 ± 3.5	90	11.3
4	NSR	2.7 ± 2.3	75	10.6	5.6 ± 3.0	97	10.6
	RPEDC	4.4 ± 3.2	71	13.4	3.0 ± 2.2	100	7.8
Total	NSR	3.4 ± 2.9	103	9.7	4.2 ± 2.8	103	8.0
	RPEDC	4.5 ± 3.5	100	11.3	3.2 ± 2.6	100	7.5

error > 5 pixels in Table 5.4. Figure 5.5 shows an example automatic segmentation result for each of the volume groups, and Figure 5.6 shows two examples of erroneous automated segmentation.

5.5.2 Reproducibility Results

The NSR and RPEDC volumes and the percent differences in volume between the 0° and 90° datasets are reported in Table 5.5. The table shows that the calculated volumes of the NSR and RPEDC measured on a 0° volumetric scan and equivalent 90° scan differed on average by 0.28 ± 0.28% and 1.60 ± 1.57%, respectively.

5.5.3 Performance

We coded the algorithm using MATLAB, resulting in an average computation time of 1.7 seconds per image (512 × 1000 pixels) on a laptop computer with a 64-bit operating system, Intel Core i7 CPU at 1.73 GHz, a 7200 RPM hard drive, and 16

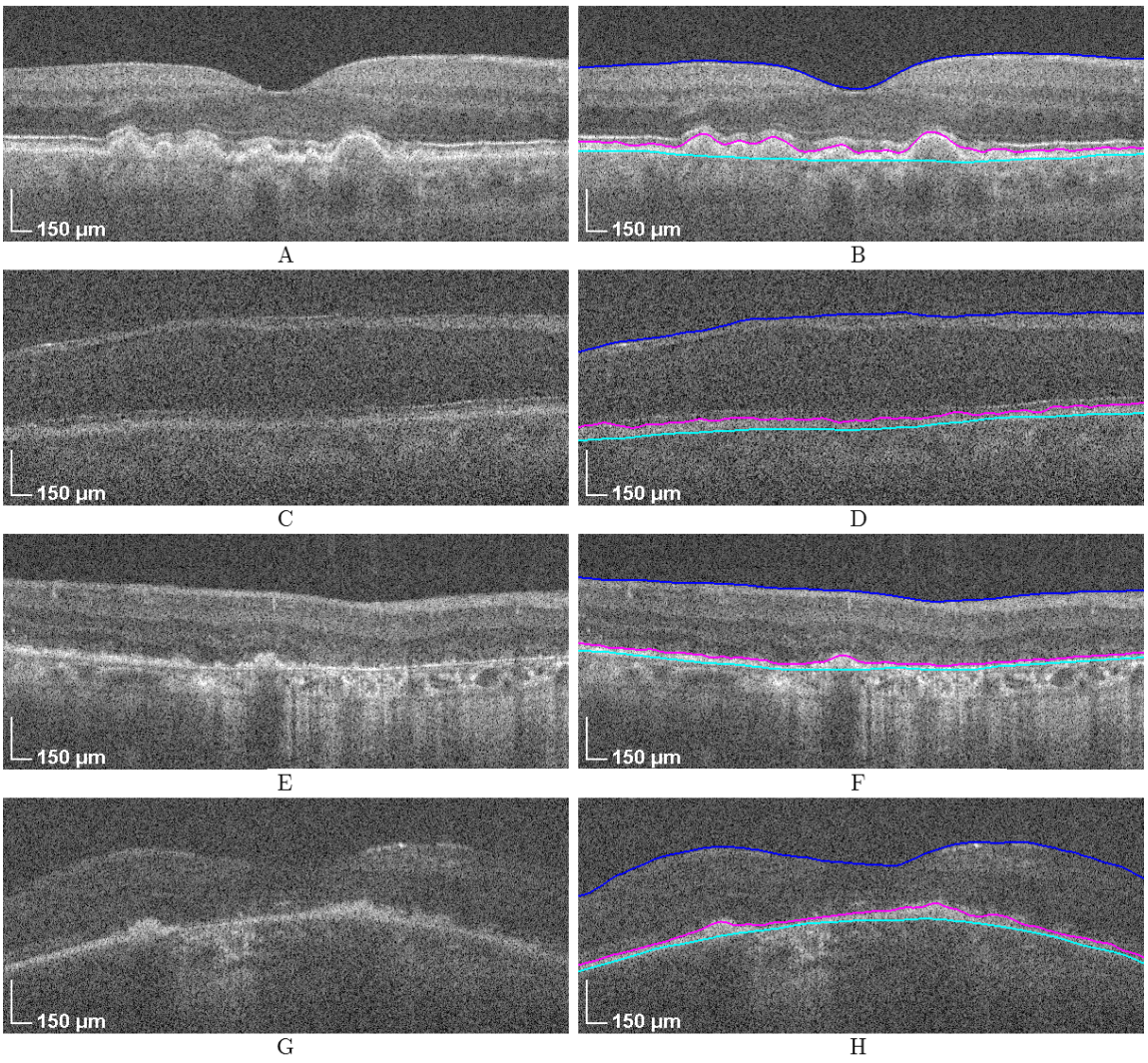

FIGURE 5.5: SD-OCT images of eyes with intermediate AMD without and with automatic segmentation (inner ILM: blue, inner RPEDC: magenta, and outer BM: cyan). (A) A high quality image with both large and small drusen and (B) the segmentation result. (C) A low quality image with small deposits of drusen material and (D) the segmentation result. (E) A high quality image demonstrating an extensive area of GA with irregular reflectivity from outer retinal structures and (F) the segmentation result. (G) A low quality image with an area of GA and an overlying small spot of hyper-reflectivity that was not included as REPDC and (H) the segmentation result.

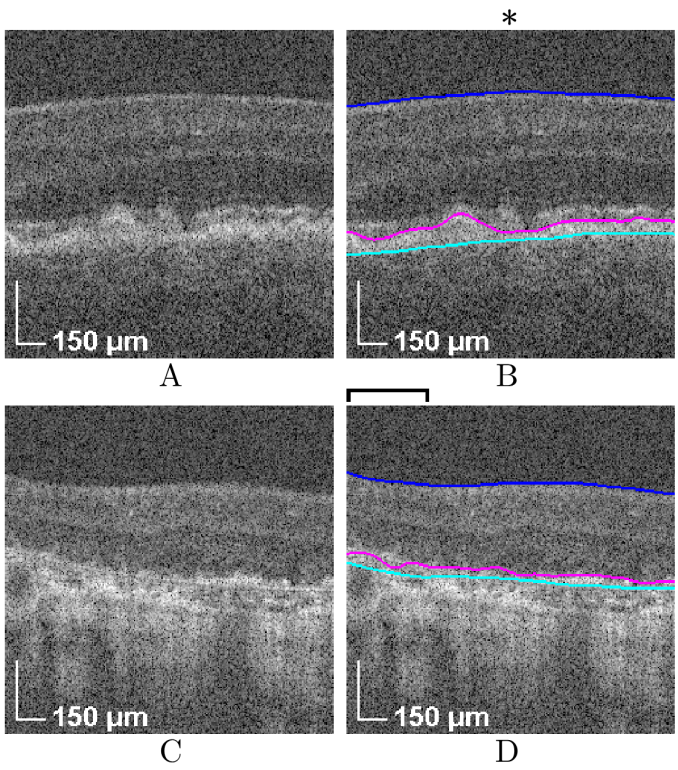

FIGURE 5.6: Erroneously segmented SD-OCT images of eyes with intermediate AMD. (A) An SD-OCT image from Volume Group 3 with a subretinal drusenoid deposit, and (B) the automated algorithm erroneously segmented the RPE without drusenoid material (under asterisk). (C) An SD-OCT image from Volume Group 3 with atrophy of the RPE and a hyper-reflective choroid typical of GA, and (D) the automated algorithm erroneously segmented hyper-reflective structures within the choroid as the RPEDC (under bar).

GB of RAM. This time includes the overhead required for read and write operations. Manual segmentation took an average time of 3.5 minutes per image.

5.6 Discussion

Despite the establishment of pre-defined segmentation guidelines and practice sessions for manual segmentation on training data sets, two certified graders did not achieve perfect agreement when delineating the layer boundaries (Table 5.4, inter-observer). Implementing even more explicit guidelines for manual segmentation

Table 5.5: Reproducibility of measured layer volumes between 0° and 90° datasets of the same patient and their calculated percent difference.

	Volume (mm^3)				**Difference (%)**	
	NSR		RPEDC		NSR	RPEDC
Patient	0°	90°	0°	90°		
1	3.45	3.45	0.31	0.32	0.00	1.62
2	3.56	3.57	0.36	0.36	0.20	0.33
3	3.74	3.71	0.38	0.38	0.75	0.36
4	3.46	3.45	0.44	0.43	0.15	1.50
5	3.48	3.49	0.46	0.44	0.30	4.18
Mean	3.54	3.53	0.39	0.39	0.28	1.60
SD	0.12	0.11	0.06	0.05	0.28	1.57

might improve agreement, but this will not eliminate the inherent intra-observer variability and differences between manual tracings. Also note that although we excluded RPEDC material over a nearly absent RPE with a minimum lateral width equal to the azimuthal resolution (67 µm in this study), future investigators may employ a fixed width to improve uniformity across clinical studies.

Results show that our algorithm automatically segmented the NSR and RPEDC in eyes with intermediate AMD with an accuracy comparable to that of a second human grader (Table 5.4). A low volume quality did not significantly reduce the segmentation accuracy (Table 5.4, Volume Group 1 vs. 2 and 3 vs. 4), illustrating the algorithm's robustness for images of varying quality. Future study across a dataset of several hundred eyes with intermediate AMD may reveal new segmentation challenges that occur infrequently and thus may not have been identified in this series. We currently do not know the range of changes in RPEDC volume associated with disease progression or how these compare to color fundus photographs, and therefore we cannot be certain of the accuracy required for predictive volume measurements. RPEDC volume measurements from SD-OCT imaging will hopefully provide greater accuracy in assessing drusen load compared to the common technique of mentally

summing the area of drusen visible on color fundus photographs [127].

Our measurement of the RPEDC builds from the known pathophysiology and morphology of AMD and should be useful in testing hypotheses of disease progression. The term *drusen* has been based on yellow spots visible on ophthalmoscopy, and has been recorded with color fundus photographs. They contain a wide range of material including lipids, lipoproteins, amyloid, collagen, proteins associated with inflammation, and degradation products [177–179]. Although drusen can be comprised of basal laminar deposits (internal to the RPE), basal linear deposits (external to the basal lamina of the RPE), and apical or subretinal deposits (reticular drusen), the difference between aging processes and the onset of AMD remains controversial [169, 180–182]. Each of these deposits has been implicated in the pathogenesis of AMD, and it would appear clinically relevant to identify the early onset of changes in the RPE associated with AMD. Although large drusen can be readily segmented from the RPE, small drusen deposits in the early stages of disease, depending on the pattern of reflectivity, would likely initially produce a change in RPE volume followed by a subsequent appearance of distinct drusen as the deposits enlarge. Thus, because of our interest in identifying RPE and drusen pathology associated with early AMD, we pursued RPEDC measurement so as to capture the full extent of early disease and chose to compare this to an aged non-AMD control population. This will be important when paired with measurements of the NSR to investigate the timing of RPE versus photoreceptor [149, 183, 184] morphologic changes in early AMD.

Because non-central GA may be a component of intermediate AMD, we included eyes with GA in our algorithm testing. The algorithm was marginally less accurate for volumes containing both GA and drusen versus solely drusen largely due to the differing morphology of the RPEDC in these two types of pathology (Figure 5.6D). Furthermore, the algorithm exhibited a tendency to segment the RPE rather than the RPEDC in the presence of some subretinal drusenoid deposits (Figure 5.6B).

Utilizing an integrated algorithm to segment these types of pathology resulted in a trade-off between extending functionality and compromising accuracy. To fully disclose these errors and any other limitations of our algorithm, we have made the complete validation dataset available online. A drawback of this or any automated segmentation system may be the need for human review of the automated segmentation results to assess for unexpected errors such as the ones seen in Figure 5.6.

Even with these limitations, our algorithm segmented drusen of various shapes and sizes (Figure 5.5B), images of significantly low quality (Figure 5.5D), RPE and drusen in the presence of GA (Figure 5.5F), and retinae with irregular curvatures (Figure 5.5H). Furthermore, the $< 5\%$ difference in measured layer volume when comparing 0° and 90° scans of the same eye (Table 5.5) attests to the reproducibly of the automatic measurements. Differences in the measured layer volume may partially be attributed to the fact that the volumes were unregistered.

Not only did the algorithm segment these images accurately and reproducibly, but also efficiently. On average, a certified grader could draw three boundaries on a single B-scan in 3.5 minutes. This long segmentation time was largely attributed to the difficulty in segmenting the irregularly shaped inner border of the RPEDC and in distinguishing the RPE and drusen from extraneous material, such as hyperreflective foci and drusenoid remnants over GA. Future studies will include a more in-depth analysis on a larger pool of data and could identify common automated drusen segmentation errors similar to other studies [162, 163].

The clinical implications of these results are encouraging for large-scale ophthalmic studies, since they suggest that this automatic segmentation algorithm can efficiently and reproducibly segment the NSR and RPEDC. Furthermore, for clinical studies with a wide range of image quality, our algorithm is capable of accurately segmenting images of lower quality. Lastly, automatic segmentation of the RPEDC contributes to the progress in drusen quantification, which is especially important in

AMD studies. However, note that the algorithm segments all drusen types, including soft drusen, cuticular drusen, and subretinal drusenoid deposits. While soft drusen and subretinal drusenoid deposits have been shown to be significant indicators of AMD progression [169, 173, 174, 185], cuticular drusen are considered by some as not being associated with AMD [186, 187]. Our future studies will include the development of automated drusen classification techniques to segment drusen types that are specific to a particular disease.

Validation of our proposed algorithm was limited to intermediate AMD and was not tested for disease processes such as neovascular AMD, vitreoretinal pathologies, or proliferative diabetic retinopathy (DR). Algorithmic modification, extension of application, and assessment of the performance in eyes exhibiting pathologies outside of non-neovascular AMD is part of our ongoing work. Furthermore, while only volumes with high or low quality were considered in our validation study, this does not imply that the algorithm necessarily errs for volumes excluded from the study. These volumes were excluded due to missing retinal data. All such volumes will be included in our future studies identifying common segmentation and acquisition errors on a broader pool of data.

5.7 Summary

In summary, we developed a fully automatic algorithm to segment three retinal boundaries with a performance comparable to that of manual graders. The algorithm performed reliably for images containing drusen and GA and for images varying in quality, and yielded reproducible measurements of layer volumes for the same eye. Our automatic approach can reduce time and labor costs and can yield an objective evaluation for the study of AMD in future clinical studies.

6

Clinical Application: Confocal Microscopy Biomarkers of AMD

6.1 Motivation

AMD is the leading cause of irreversible blindness in Americans older than 60 years [146]. In a recent study, Ding *et al.* showed that anti-amyloid therapy protects against RPE damage and vision loss in an APOE4 mouse model of AMD [10]. In that study, the average size and density of RPE cells imaged by confocal fluorescence microscopy were used as biomarkers for disease progression. To obtain these quantitative metrics, 22,495 cells were analyzed using customized semi-automatic segmentation software. To achieve a drastically faster segmentation rate, this chapter describes a fully automatic algorithm to segment RPE cells in confocal fluorescence microscopy images of flat-mounted retina for both normal and AMD mouse models.

6.2 RPE Cell Segmentation Algorithm

We implemented our closed-contour GTDP segmentation framework described in Section 2.2 to segment RPE cells imaged by confocal fluorescence microscopy. The

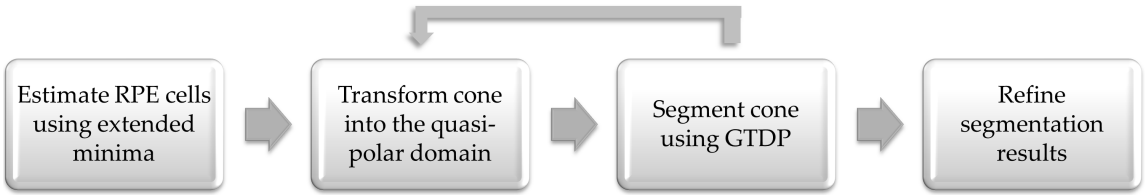

FIGURE 6.1: Flowchart of the GTDP algorithm for segmenting RPE cells on confocal fluorescence microscopy images of normal and AMD flat-mounted mouse retina.

algorithm is outlined in Figure 6.1 and described in the following subsections.

6.2.1 Pilot Estimation of RPE Cell Morphology

We first normalize the intensities of the image $\{\boldsymbol{I}_c^{full} \in \mathbb{R}^{1024\times1024} \mid 0 \leqslant \boldsymbol{I}_c^{full} \leqslant 1\}$ and smooth $\boldsymbol{I}_c^{full}$ using an 11 $\times$ 11 pixel Gaussian filter with a standard deviation of 25 pixels. Next, we compute the extended-minima transform [188] that finds all minima and suppresses those with a depth less than 0.05. To generate a binary image $\boldsymbol{B}_c^{full}$ containing pilot estimates for all cells, we set $\boldsymbol{B}_c^{full} = 1$ for all points $\boldsymbol{z}$ lying within the convex hull [176] of each minima.

To localize a single cell and its corresponding pilot estimate, we crop $\boldsymbol{I}_c^{full}$ and $\boldsymbol{B}_c^{full}$ to smaller images $\boldsymbol{I}_c$ and $\boldsymbol{B}_c \in \mathbb{R}^{201\times201}$. The cropped image size was chosen such that the largest conceivable cell in our model would not be clipped, and the central pixel for both images corresponds to the $\boldsymbol{z}_{ref}$ computed using the pilot estimate in $\boldsymbol{B}_c$. Since $\boldsymbol{B}_c$ may contain other cell estimates, we set all pixels outside the current pilot estimate to zero. Example images of $\boldsymbol{I}_c$ and $\boldsymbol{B}_c$ are shown in Figures 6.2A and B, respectively.

6.2.2 Transformation into the Quasi-Polar Domain

The RPE cell image is next transformed into the quasi-polar domain using Steps 1-3 in Section 2.2.2 with the following implementation details:

- The horizontal and vertical polar axes follow $\{\theta \in \mathbb{Z} \mid 0 \leqslant \theta \leqslant 360\}$ and

$\left\{r \in \mathbb{Z} \mid 1 \leqslant r \leqslant \sqrt{(F - i_{ref})^2 + (G - j_{ref})^2}\right\}$, respectively.

- After generating $\boldsymbol{B}_p$ in Step 1, we set $\boldsymbol{b}_{p1} = \boldsymbol{b}_{p(\Theta+1)} = \boldsymbol{b}_{p1} \vee \boldsymbol{b}_{p(\Theta+1)}$ (where $\vee$ is the element-wise logical OR operator) since the first column (0°) and last column (360°) should be equal. Note that there are a total of $\Theta + 1$ columns since θ ranges from 0° to 360°.

- In Step 2, the function $r = f_p[\theta]$ is found by segmenting $\boldsymbol{B}_p$ using the GTDP layer segmentation technique and smoothing the path using a moving average filter with a span of 1%. The resulting function is shown in green in Figure 6.2C, and it provides the shape information necessary to flatten the feature into the quasi-polar domain.

- In Section 6.2.3, we also generate a threshold image $\boldsymbol{T}_c$ where

$$\boldsymbol{T}_c[\boldsymbol{z}] = \begin{cases} 1, & \text{if } \boldsymbol{F}_c[\boldsymbol{z}] > \overline{\boldsymbol{F}}_c \\ 0, & \text{otherwise} \end{cases}, \quad \forall\ \boldsymbol{z}. \tag{6.1}$$

  In Equation (6.1), $\boldsymbol{F}_c$ is the Wiener-filtered image of $\boldsymbol{I}_c$ and $\overline{\boldsymbol{F}}_c$ is the mean of $\boldsymbol{F}_c$. We then set all connected components in $\boldsymbol{T}_c$ smaller than 20 pixels to zero, and for all $\boldsymbol{z}$ where $\boldsymbol{B}_c^{full}[\boldsymbol{z}] = 1$ and $\boldsymbol{B}_c[\boldsymbol{z}] = 0$, we set $\boldsymbol{T}_c[\boldsymbol{z}] = 1$. Finally, we transform $\boldsymbol{T}_c$ into its quasi-polar equivalent, $\boldsymbol{T}_q$.

The transformation of $\boldsymbol{I}_c \rightarrow \boldsymbol{I}_p \rightarrow \boldsymbol{I}_q$ is shown in Figure 6.2A→D→F. Figure 6.2E is the quasi-polar transformed pilot estimate, showing that the transform yielded a fully flattened pilot estimate and an approximately flattened RPE cell structure.

6.2.3 GTDP Cell Segmentation

After generating the quasi-polar transformed image $\boldsymbol{I}_q$, we use our GTDP layer segmentation framework from Section 2.1 to segment the RPE cell boundary. The graph weights are calculated based on the following three cost functions:

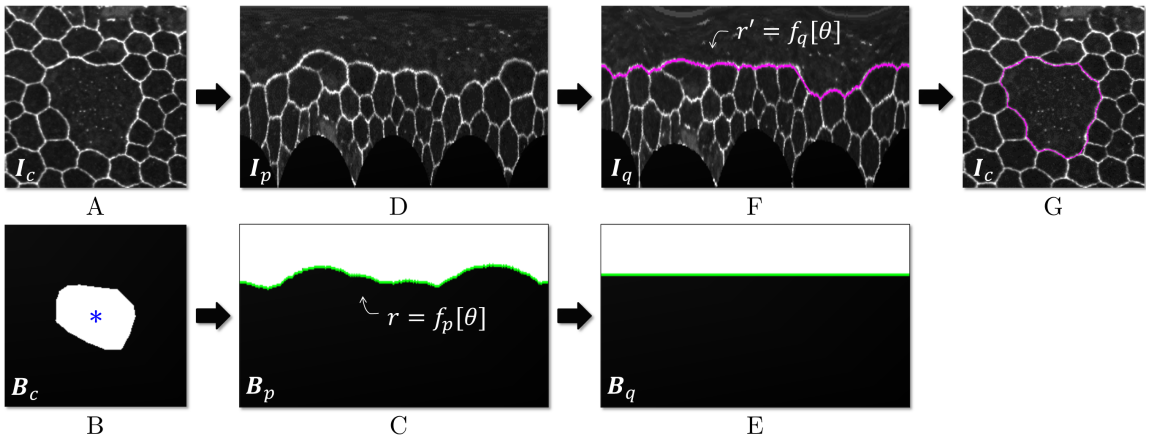

FIGURE 6.2: RPE cell segmentation using the quasi-polar transform. (A) Image of the RPE cell to segment and (B) its pilot estimate and centroid (blue asterisk). (C) Polar transformation of B segmented using GTDP to generate $r = f_p[\theta]$ (green). (D) Polar transformation of A using the centroid from B as the reference pixel. The black regions are invalid points that lie outside the image in A. (E,F) Images C and D flattened based on $f_p[\theta]$, and F segmented using GTDP to form $r' = f_q[\theta]$. (G) Transformation of $f_q[\theta]$ from F back into the Cartesian domain.

1. Penalize bright nodes further from the centroid to avoid segmenting multiple RPE cells at once ($\boldsymbol{J}_1 \in \mathbb{R}^{R\times\Theta}$).

2. Penalize nodes that include the pilot estimates of other cells to also avoid segmenting multiple cells at once ($\boldsymbol{J}_2 \in \mathbb{R}^{R\times\Theta}$).

3. Penalize nodes that fall below the $\boldsymbol{T}_q$ threshold criteria ($\boldsymbol{J}_3 \in \mathbb{R}^{R\times\Theta}$).

We then implement these three cost functions using the following MATLAB notation, where $\boldsymbol{t}_q$ and $\boldsymbol{j}_k$ are corresponding columns in $\boldsymbol{T}_q$ and $\boldsymbol{J}_k$, respectively, and

$$\begin{aligned} \boldsymbol{j}_1 &= \text{bwlabel}(\boldsymbol{t}_q > 0) \\ \boldsymbol{j}_2 &= \text{bwlabel}(\ \boldsymbol{t}_q \mid \boldsymbol{t}_q == -1) \\ \boldsymbol{j}_3 &= 2 \cdot \text{bwlabel}(\boldsymbol{t}_q \sim= -1) - 2. \end{aligned} \tag{6.2}$$

We then combine these cost functions to generate $\boldsymbol{J}_{total}$, where

$$\begin{aligned} \boldsymbol{J}_1(\boldsymbol{J}_1 == 0) &= \boldsymbol{J}_2(\boldsymbol{J}_2 > 0) + 1.5 \\ \boldsymbol{J}_3(\boldsymbol{J}_3 < 0) &= \max(\boldsymbol{J}_3) + 2 \\ \boldsymbol{J}_{total} &= \boldsymbol{J}_1 + \boldsymbol{J}_3. \end{aligned} \tag{6.3}$$

Finally, we calculate edge weights using

$$\begin{aligned} \omega_{ab} = &\text{LinNorm}(-i_a - i_b,\ 0,\ 0.25) + \\ &\text{LinNorm}(\boldsymbol{J}_{total}[a] + \boldsymbol{J}_{total}[b],\ 1,\ 2)\ +\ \omega_{min}, \end{aligned} \tag{6.4}$$

where $\boldsymbol{J}_{total}[n]$ is the value of $\boldsymbol{J}_{total}$ at node n.

We next limit the search region by setting all edges connected to nodes in previously segmented cells to zero. We also prevent the path from encapsulating a previously segmented cell. Automatic endpoint initialization and Dijkstra's algorithm are then used to find the minimum-weighted path described by the function $r' = f_q[\theta]$.

Since $f_q[\theta]$ must be equal for $\theta = 0^\circ = 360^\circ$, we check to see if this condition is satisfied, as it is not guaranteed when using automatic initialization. If the condition is not met, then we manually initialize the start and end nodes to $(r', \theta) = (f_q[0],\ 0)$ and $(f_q[0],\ 360)$, respectively to find the shortest path $\boldsymbol{p}_0$. We then initialize the endpoints to $(f_q[360],\ 0)$ and $(f_q[360],\ 360)$ to find path $\boldsymbol{p}_{360}$. We then select the final path (Figure 6.2F, magenta) as the one that is brighter overall following

$$f_q = \begin{cases} \boldsymbol{p}_0, & \text{if } \sum_{\theta=0}^{360} \boldsymbol{I}_q[\boldsymbol{p}_0[\theta],\ \theta] \geqslant \sum_{\theta=0}^{360} \boldsymbol{I}_q[\boldsymbol{p}_{360}[\theta],\ \theta] \\ \boldsymbol{p}_{360}, & \text{otherwise} \end{cases}. \tag{6.5}$$

Finally, the path $f_q[\theta]$ is transformed back into the Cartesian domain (Figure 6.2G, magenta) following Section 2.2.4 and the coordinates are shifted from $\boldsymbol{I}_c$ onto $\boldsymbol{I}_c^{full}$. The resulting cell segmentation is marked on a binary edge image

$\boldsymbol{E}_c^{full} \in \mathbb{R}^{1024\times1024}$, where for all pixels $\{\boldsymbol{z}_k\}_{k=1}^{\Theta}$ on the segmented path, $\boldsymbol{E}_c^{full}[\boldsymbol{z}_k] = 1$. For any adjacent pixels $\boldsymbol{z}_k$ and $\boldsymbol{z}_{k+1}$ that are unconnected, we use linear interpolation to connect the dots and create a closed-contour.

6.2.4 Segmentation of Subsequent RPE Cells

To segment subsequent RPE cells, we iterate through Sections 6.2.2 to 6.2.3 for all pilot estimates in $\boldsymbol{B}_c^{full}$. To prevent gaps from occurring between adjacent cells, we create a preference for already-segmented cell borders by brightening their intensity values such that $\boldsymbol{I}_c[\boldsymbol{z}] = \max\left(\boldsymbol{I}_c[\boldsymbol{z}],\ \text{mean}(\boldsymbol{I}_c) + \text{std}(\boldsymbol{I}_c)\right)$ (using MATLAB notation) and $\boldsymbol{T}_c[\boldsymbol{z}] = 1$ for all $\boldsymbol{z}$ where $\boldsymbol{E}_c^{full}[\boldsymbol{z}] = 1$.

6.2.5 Refinement

For our validation study in Section 6.3.1, we used Ding *et al.*'s [10] semi-automatic segmentation as our gold standard. In those segmentation results, cells were separated by drawing a line through the middle of the cell border with a thickness of a single pixel. Since our algorithm does not necessarily yield a cell border with a thickness of a single pixel, this section describes the post-processing steps required to match our automatic segmentation with the gold standard protocol, and to remove any erroneous cell segmentations.

First, we remove all cells smaller than 50 pixels by setting $\boldsymbol{E}_c^{full}[\boldsymbol{z}] = 1$ for all $\boldsymbol{z}$ lying within those cells. We then generate the skeleton of $\boldsymbol{E}_c^{full}$ and remove all spurs [126]. Next, we look at individual cell edges by setting branch points in $\boldsymbol{E}_c^{full}$ equal to zero. We compute the minimum edge threshold as $t = \text{mean}(\boldsymbol{I}_c^{full}[\boldsymbol{z}]) - 1.5 \cdot \text{std}(\boldsymbol{I}_c^{full}[\boldsymbol{z}])$ using all points $\boldsymbol{z}$ where $\boldsymbol{E}_c^{full}[\boldsymbol{z}] = 1$. If all pixels for a given cell segmentation fall below t or if 80% of the pixels fall below t and there were at least 15 such pixels, then we remove the cell segmentation from $\boldsymbol{E}_c^{full}$. Once we remove all invalid cell segmentations, we restore all branch points on $\boldsymbol{E}_c^{full}$ and remove any

newly created spurs or pixels no longer connected to the cell segmentation.

6.3 Validation Methods

6.3.1 Image Dataset

We used Ding *et al.*'s dataset published in PNAS in 2011 [10]. This dataset included 23 confocal fluorescence microscopy images (0.64 × 0.64 mm) of central RPE flat mounts from 17 mice with approximately 1000 cells per image. RPE cells were stained with a rabbit antibody against ZO-1 (402200, 1:100; Invitrogen) and imaged on a Nikon Eclipse C1 microscope.

6.3.2 Automatic versus Manual Segmentation

To validate our fully automatic segmentation results against the gold standard, we compared the cell count and mean cell size for each of the 23 images in Ding *et al.*'s study [10]. To prevent from biasing our results, these images were not used during the algorithm development stage. Instead, a single confocal microscopy fluorescence image of an AMD mouse model not included in the validation dataset was used to train the algorithm.

We did not alter the data in Ding *et al.*'s study in any shape or form, with one slight exception. In that study, closed-counter features smaller than 100 pixels were absorbed into neighboring cells since such regions were likely a result of incorrect manual segmentation. In our replication of Ding *et al.*'s results, we discarded these regions from our quantitative comparison since such regions were negligible. Furthermore in Ding *et al.*'s study [10], regions of the image considered invalid due to imaging errors, flat-mount preparation errors, or cells being cut off by image borders, were marked separately and discarded from the analysis. In our study, we used the markings from [10] to ignore the exact same invalid regions in our analysis. The above two types of outliers occupied a very small percentage of the total area

segmented.

6.4 Validation Results

Quantitative results for the RPE cell segmentation algorithm are shown in Table 6.1. The average error between automatic segmentation and the gold standard was $1.49 \pm 1.44\%$ for the cell count and $1.32 \pm 1.53\%$ for the mean cell area. The median error was found to be 0.97% and 0.71% for the detected number of cells and mean cell area, respectively.

Qualitative results for this validation study are shown in Figure 6.3, where Figure 6.3A (corresponding to Image 16 in Table 6.1) is the automatically segmented confocal fluorescence image of an AMD flat-mounted mouse retina, and Figure 6.3B-G are zoomed-in cell segmentation results.

Figure 6.4 (top) shows two confocal images of RPE cells along with their gold standard (Figure 6.4, middle) and automatic (Figure 6.4, bottom) segmentation results. The image in Figure Figure 6.4A corresponds to Image 9 in Table 6.1 with approximately median error, and Figure 6.4B shows Image 10 from Table 6.1 with maximum error.

Lastly, Figure 6.5 shows zoomed-in images of Images 6 and 9 from Table 6.1 comparing the gold standard (Figurse 6.5A-E) to automatic segmentation (Figures 6.5F-J). The images in Figures 6.5A-C are examples of erroneous gold standard segmentation, while Figure 6.5J is an example of erroneous automatic segmentation. Their corresponding images (Figures 6.5E-H) are examples of accurate segmentation. Finally, Figures 6.5D,I show an undetermined case where it is unclear which segmentation is correct.

All 23 images used in the study and their corresponding manual and automatic segmentation data are available at `http://www.duke.edu/~sf59/Chiu_BOE_2012_dataset.htm`. The "single click" algorithm was coded in MATLAB and resulted in

Table 6.1: Comparison of RPE cell count and average cell area obtained for each confocal fluorescence microscopy image via fully automatic segmentation versus the gold standard.

	Number of Cells			**Mean Cell Area**		
Image	Gold Standard (N)	GTDP (N)	Error (%)	Gold Standard (pixels)	GTDP (pixels)	Error (%)
1	885	855	3.39	1003	1036	3.27
2	710	721	1.55	1228	1204	1.97
3	829	830	0.12	1087	1082	0.47
4	776	775	0.13	1126	1124	0.23
5	825	817	0.97	1092	1100	0.71
6	923	902	2.28	866	882	1.83
7	981	937	4.49	899	940	4.53
8	971	960	1.13	875	881	0.72
9	1097	1088	0.82	832	836	0.52
10	1253	1181	5.75	715	757	5.94
11	1187	1170	1.43	771	781	1.24
12	833	828	0.60	1062	1065	0.21
13	900	895	0.56	1007	1010	0.23
14	1235	1220	1.21	730	736	0.89
15	1005	999	0.60	892	895	0.32
16	1109	1075	3.07	815	839	2.96
17	1084	1077	0.65	836	840	0.37
18	1003	982	2.09	916	934	1.93
19	1013	1008	0.49	865	866	0.11
20	1054	1042	1.14	856	863	0.90
21	931	927	0.43	970	972	0.16
22	973	967	0.62	931	935	0.36
23	919	912	0.76	964	969	0.45
Median	973	960	0.97	899	934	0.71
Mean	978	964	1.49	928	937	1.32
SD	141	132	1.44	130	123	1.53

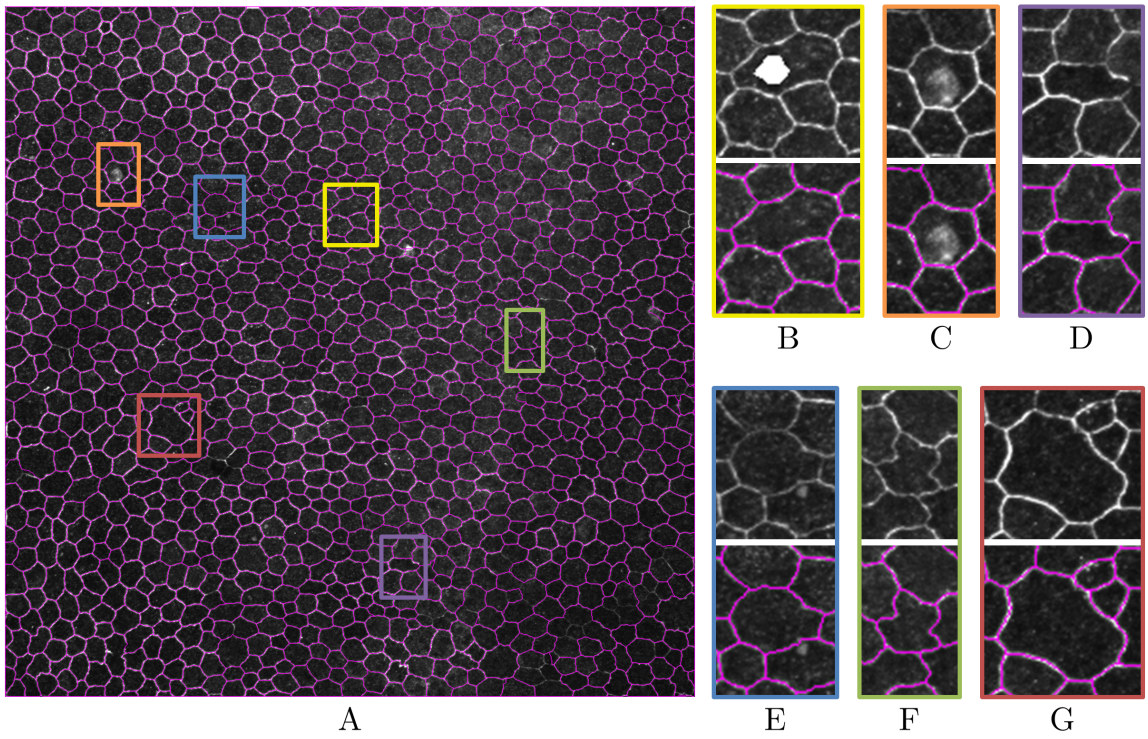

FIGURE 6.3: Examples of automatic RPE cell segmentation. (A) Automatically segmented confocal fluorescence image of a flat-mounted mouse retina (Image 16 in Table 6.1). The cell borders could still be segmented in cases when (B) the pilot estimate (white) was off-center and not a close estimate of the cell, (C) image artifacts or extraneous features were present, (D) the reflectivity of the cell border varied, (E) the cell had a low SNR, (F) the cell was of an abnormal shape, and (G) cell sizes were large or small. Each colored box in A corresponds to the zoomed-in image with the same colored box in B-G.

an average computation time of 2.95 minutes per image (with an average of 964 cells per image) on a desktop computer with a 64-bit operating system, Core i7 2600K CPU, solid state hard drive, and 16 GB of RAM. This time included the overhead required for reading and writing operations.

6.5 Discussion

To the best of our knowledge, no other technique has been reported for fully automatically segmenting confocal fluorescence images of RPE cells. The qualitative

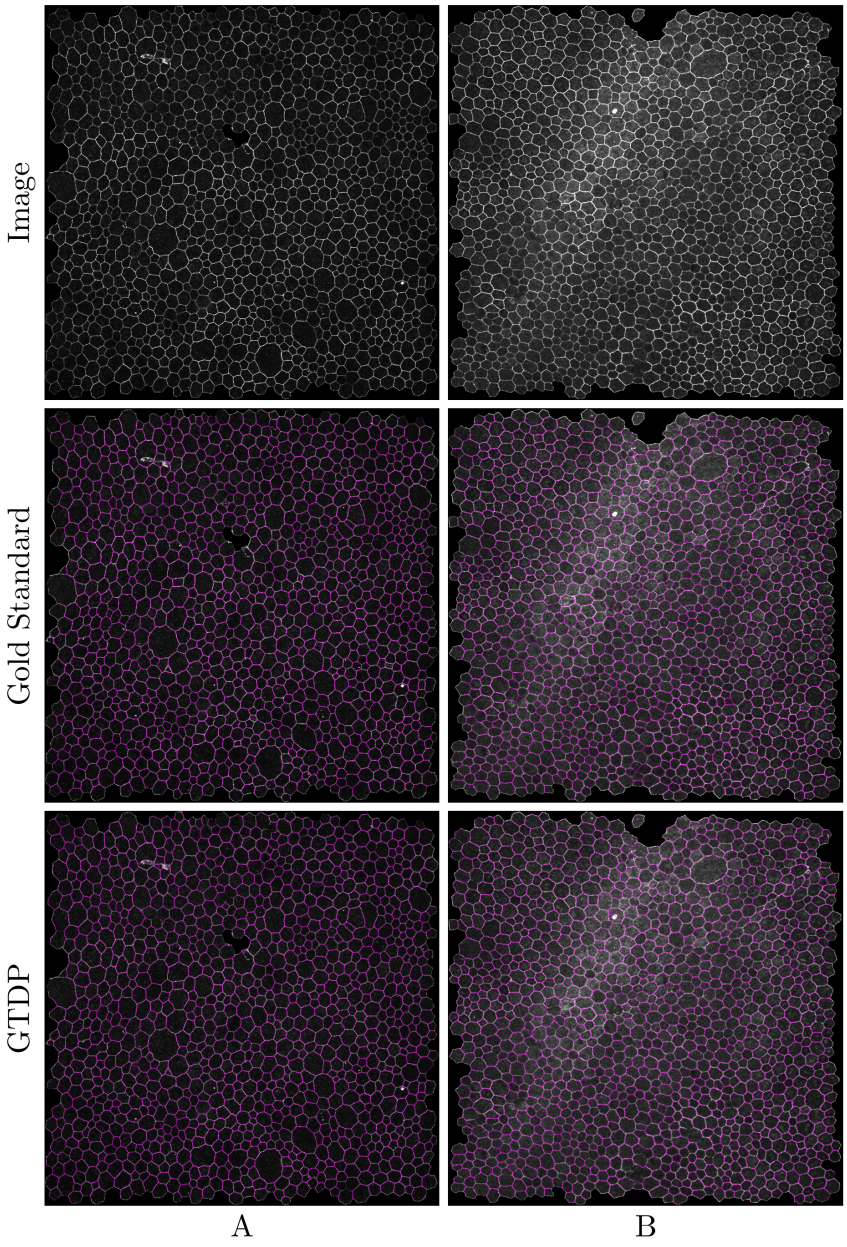

FIGURE 6.4: Comparison of fully automatic segmentation versus the gold standard. *Top*: two confocal fluorescence microscopy images of flat-mounted mouse retina. *Middle*: gold standard segmentation of RPE cells (magenta) obtained semi-automatically using an independent technique. *Bottom*: fully automatic segmentation (magenta) using the closed-contour GTDP technique. In the gold standard, cells bordering the image and invalid regions due to folding of tissue during preparation and imaging artifacts were ignored. These regions (black borders) were therefore discarded for the comparison study shown in Table 6.1.

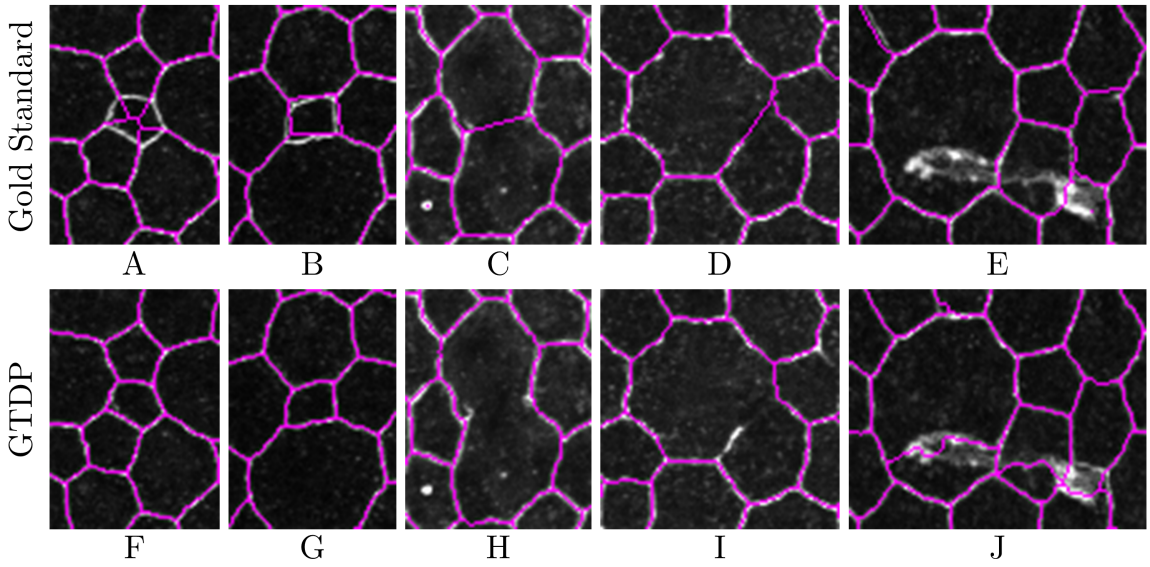

FIGURE 6.5: Zoomed-in comparison of fully automatic GTDP segmentation versus the gold standard. (A) *Erroneous gold standard segmentation*: the small middle cell was merged with adjacent cells. (B) *Erroneous gold standard segmentation that did not significantly alter quantitative comparison*: although the middle cell was incorrectly shifted, the cell count remained correct. (C) *Erroneous gold standard segmentation*: an enlarged diseased cell was incorrectly separated into two cells. We emphasize that the errors in A-C were very infrequent in the gold standard dataset consisting of thousands of semi-automatically segmented cells. However, existence of even a handful of such errors shows the limitation of subjective segmentation techniques relative to our automatic segmentation, F-H. (D,I) *An undetermined case*: the gold standard, D, delineated two separate cells, while the automatic segmentation, I, grouped them as a single cell. Since these are diseased RPE cells, it is unclear whether cells with a partially disappeared cell border should be considered individually or as a unit. (J) *Erroneous automatic segmentation*: borders were incorrectly drawn through the cells due to an artifact. (E-H) Accurate gold standard and automatic segmentations.

results shown in Figure 6.3 demonstrate accurate automatic cell segmentation despite the presence of image artifacts, low SNR, or inaccurate estimations. Furthermore, the cell shape and size were not constraining factors for the presented automatic algorithm.

Quantitative results show that our fully automatic algorithm accurately segmented RPE cells on confocal images of flat-mounted mouse retina with AMD, yielding cell count and mean cell area measurements with an average error of less than 1.5%. Automatic segmentation errors similar to Figure 6.5J occurred due to the presence of bright imaging artifacts which erroneously altered values in the first cost function of Equation (6.2). However, as shown in Figure 6.5A-C, even the gold standard segmentation reported in PNAS contained errors as well. Such errors will naturally occur in most manual or semi-automatic segmentation tasks required for large-scale studies, where multiple human experts subjectively grade images at different dates. Furthermore, since manual correction is extremely time consuming, cells with inconsequential errors (Figure 6.5B) may not have been a priority to correct. As a result, a 0% error from the gold standard does not imply perfect segmentation.

To reduce the influence of pilot estimation on the segmentation result and improve segmentation accuracy, one may employ an iterative approach where the segmentation result for one iteration is used as the pilot estimate for the next iteration. In addition, denoising of the raw images with modern adaptive techniques [189, 190] may remove imaging artifacts without altering anatomic structures, thus potentially further improving the automated segmentation performance.

Our motivation for using cell count and area as validation metrics stems from the need to quantify the extent of cell damage present in different groups of diseased mice [10]. While error in the absolute position of each automatically segmented cell may have been a more direct validation metric, the presence of errors in the gold standard made this unfeasible. Furthermore, the cell boundary is several pixels thick,

making it difficult to assign a "true" boundary position. While the gold standard often divided cells through the middle of the cell border, this was not always the case. As a result, we considered cell count and area to be a more meaningful and viable validation metric.

6.6 Summary

In summary, we demonstrated the utility of the quasi-polar transform and GTDP framework for segmenting irregularly shaped, diseased closed-contour structures. Implementation of the algorithm for RPE cell segmentation in confocal fluorescence images of flat-mounted AMD mouse retina resulted in accurate extraction of cell count and average cell size. We believe that such a tool will be extremely useful for future studies which use cell morphology as a biomarker for the onset and progression of disease.

7

Clinical Application: Multi-Platform Image Segmentation

7.1 Motivation

In the past decade, OCT has become an increasingly popular imaging modality for monitoring changes in retinal thickness and morphology for diseases such as diabetic macular edema [191]. Accurate retinal layer thickness measurements often depend on adequate image quality obtained by OCT imaging systems, as well as accurate segmentation of the retinal layer boundaries. Various OCT imaging systems are currently used clinically, including the Stratus TD-OCT system (Carl Zeiss Meditec, Dublin, CA, USA), Cirrus spectral domain HD-OCT system (Carl Zeiss Meditec, Dublin, CA, USA), and Spectralis SD-OCT system (Heidelberg Engineering, Heidelberg, Germany). While each of these OCT systems include software to segment the retina, their respective segmentation algorithms delineate the outer retinal boundary at different positions [43, 192–194].

Discrepancies in retinal thickness measurements produced by different OCT software algorithms can adversely affect the interpretations of disease progression and

response to therapy. For example, with multi-center clinical trials on DME, it is difficult to directly compare retinal thickness changes since such measurements are often obtained by different imaging systems. Similar challenges also occur in clinic when patients change physicians. While manual adjustment of the outer retinal layer boundary is possible, this approach is inefficient for clinical trials and often not practical in clinics.

This chapter discusses a fully automatic segmentation algorithm capable of segmenting three retinal layer boundaries on images of DME obtained by two different SD-OCT systems (Spectralis and Cirrus HD-OCT) without any changes made to the algorithm. We also assessed whether retinal thickness measurements determined by the algorithm could be directly compared across imaging platforms.

7.2 Retinal Layer Identification Guidelines for Multi-Platform Images of DME

Prior to any manual segmentation and algorithm development, we constructed a set of qualitative guidelines to identify layer boundaries on multi-platform images of DME. These guidelines were established to maintain a consistent and unbiased interpretation of each retinal boundary, and were determined based on previous literature, expertise from the Duke Reading Center, and representative images. The guidelines are listed as follows:

1. The total retinal thickness (TRT) is defined as the thickness of the region of tissue between the ILM and BM for both Spectralis and Cirrus images (Figures 7.1A and D).

2. On images acquired by Spectralis, the retinal thickness (sRT, s for Spectralis) is defined as the thickness of the region of tissue between the ILM and OS/RPE boundary (Figure 7.1B). This is also known as the NSR.

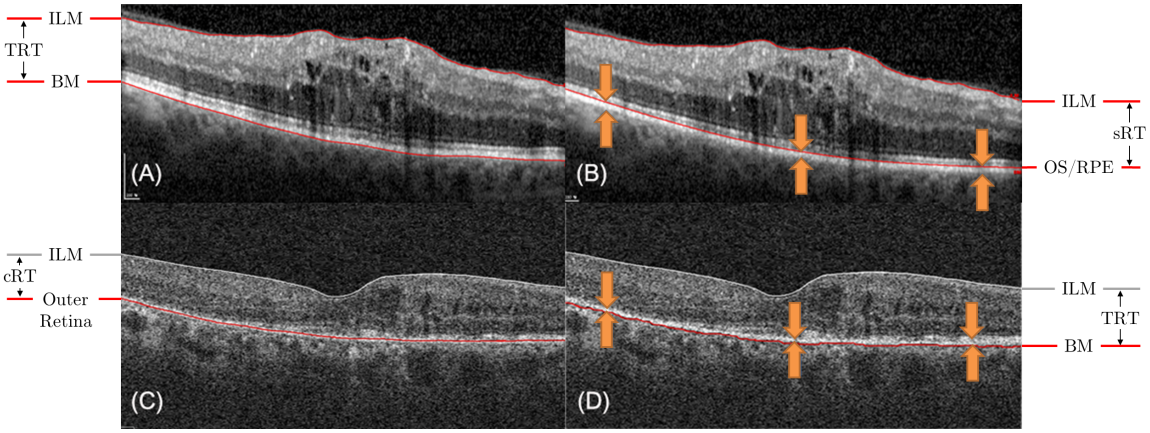

FIGURE 7.1: Spectralis and Cirrus retinal layer identification guidelines. (A) Automated Spectralis segmentation of the ILM and BM to extract total retinal thickness (TRT). (B) Semi-automated Spectralis segmentation with the outer boundary manually moved to the OS/RPE to extract the Spectralis-based retinal thickness (sRT). (C) Automated Cirrus segmentation of the ILM and outer retina to extract the Cirrus-based retinal thickness (cRT). (D) Semi-automated Cirrus segmentation with the outer boundary manually moved to BM to extract the TRT. The orange arrows indicate manual adjustment of the retinal layer boundary.

3. On images acquired by Cirrus, the retinal thickness (cRT, c for Cirrus) is defined as the thickness of the region of tissue between the ILM and a position just external to the OS/RPE. This is because the Cirrus software segments the outer retinal boundary at this location rather than at the OS/RPE boundary (Figure 7.1C).

7.3 Fully-Automatic GTDP Segmentation Algorithm

We developed an algorithm based on GTDP to segment the ILM, OS/RPE, and BM boundaries on SD-OCT images of DME. This algorithm was based on previous implementations for normal retina [56] and retina with non-neovascular AMD pathology [57]. In these previous publications, images were acquired using the Bioptigen SD-OCT system. An outline of the new algorithm is shown in Figure 7.2 and the key components needed to adapt the algorithm to Spectralis and Cirrus images of

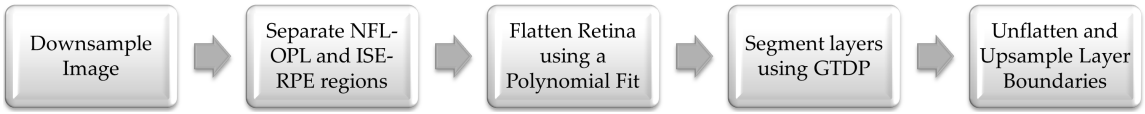

FIGURE 7.2: Flowchart of the GTDP algorithm for segmenting retinal layers on Spectralis and Cirrus SD-OCT images of eyes with DME.

eyes with DME are described below.

First, instead of flattening the retina based on the convex hull of the estimated inner RPEDC [57], the image is flattened based on a polynomial fit of BM. We fit the pilot estimate of BM to both a second and third order polynomial, and the polynomial with the lower residual norm is used to flatten the retina. Second, the graph weights are changed so that BM is segmented using a combination of gradient, intensity, and distance weights, and the OS/RPE is segmented using only gradient weights. These weights are fixed for all images of all patients captured by both the Spectralis and Cirrus systems. Third, we utilize the lateral and axial pixel resolutions imported from the Spectralis and Cirrus imaging systems so that the algorithm can segment images of any resolution. This also allows us to apply the exact same algorithm to segment both Spectralis and Cirrus images.

7.4 Semi-Automatic Segmentation by Commercial Software

The automated software algorithms provided by Spectralis and Cirrus HD-OCT each segmented two retinal layer boundaries corresponding to the ILM and BM on Spectralis (Figure 7.1A) and the ILM and outer retina on Cirrus (Figure 7.1C). Both imaging systems also generated topographic surface maps as defined by the Early Treatment Diabetic Retinopathy Study (ETDRS). In cases where the fovea was not centered on the ETDRS grid, the grid was manually centered at the fovea using the system's software (Figure 7.3). For the central 1-mm and four surrounding 3-mm ETDRS sectors (superior, inferior, nasal, and temporal), the Spectralis software

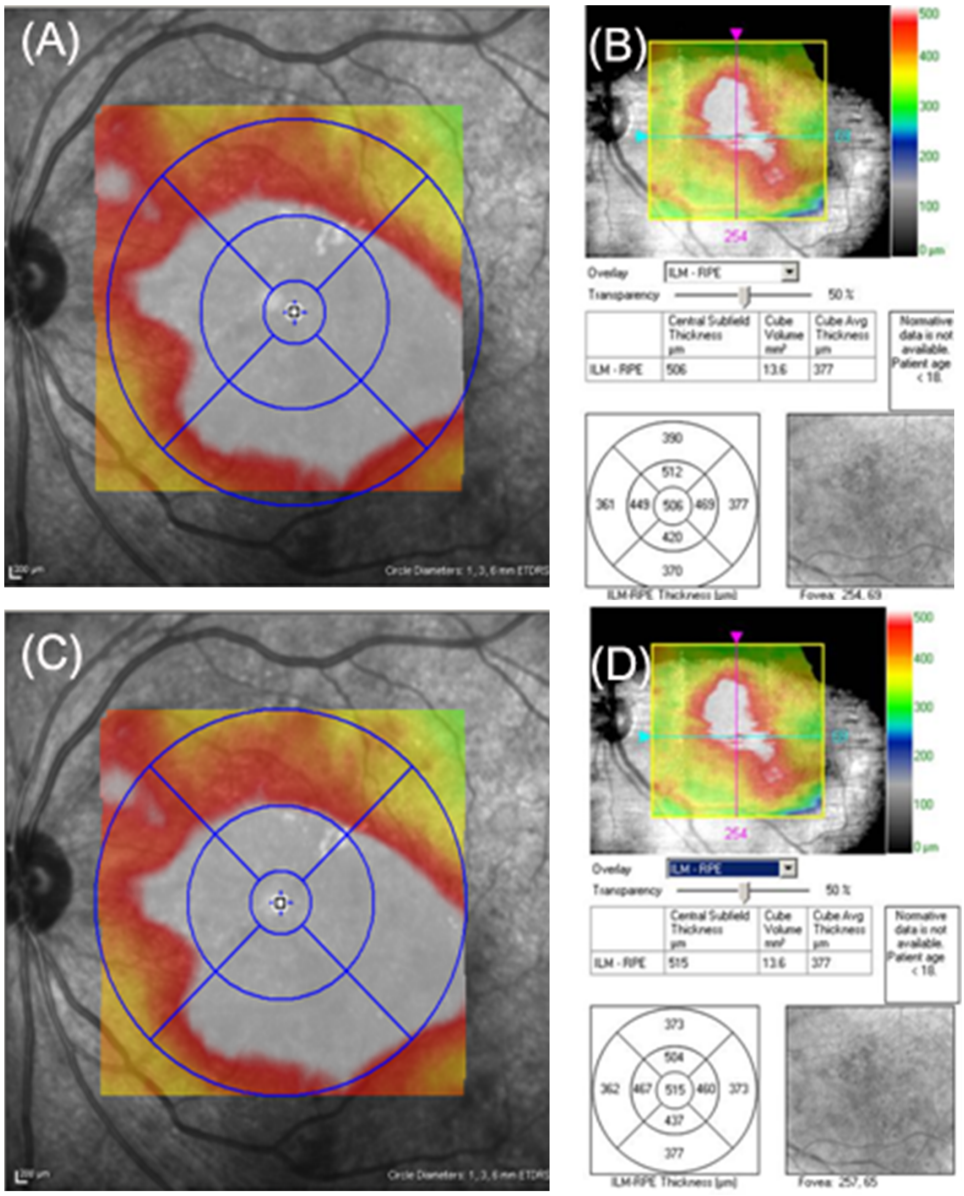

FIGURE 7.3: (A,B) Automatically generated Spectralis and Cirrus ETDRS thickness maps, respectively. (C,D) Manual adjustment of the ETDRS grid to be centered at the fovea using Spectralis and Cirrus software, respectively.

calculated mean TRT and total retinal volume (TRV) measurements while the Cirrus software computed mean cRT values. Because the Cirrus software did not produce separate retinal volume measurements for the five ETDRS grid sectors, Cirrus volume comparisons were not performed in these areas.

To correct for errors in Spectralis and Cirrus software segmentation, a certified Duke Reading Center reader manually adjusted erroneous retinal layer boundary positions using the respective system's software. Corrected measurements for Spectralis and Cirrus thickness as well as Spectralis volume were then determined.

Finally, the outer retinal layer boundaries were manually adjusted by graders to the OS/RPE on Spectralis and to BM on Cirrus (Figure 7.1B,D). This was done to enable thickness and volume comparisons against the fully-automatic GTDP algorithm using two different reference boundaries.

7.5 Validation Methods

7.5.1 Image Dataset

We validated the algorithm using SD-OCT images of eyes of subjects with DME that were enrolled in a randomized prospective DME clinical trial. The study was approved by the Duke University Review Board, which adhered to the tenets of the Declaration of Helsinki. Informed consent was obtained from all participants.

Volumetric scans were acquired using two SD-OCT imaging systems, Spectralis with Viewing Module (Ver. 5.3.0.15), and Cirrus HD-OCT with review software (Ver. 5.2.0.210). Scans acquired by Spectralis followed a custom $20^\circ \times 20^\circ$ high-speed volume acquisition protocol resulting in 512 A-scans $\times$ 49 B-scans for each eye. For Cirrus systems, the 512 $\times$ 128 Macular Cube scan protocol was used to generate 512 A-scans $\times$ 128 B-scans.

Scan quality was evaluated by a certified Duke Reading Center reader, where an image quality of *high* or *low* was assigned based on previously published criteria [57].

For example, well-resolved images free of artifacts were considered to be *high quality*, while dim images or images with artifacts from patient motion or loss of fixation were categorized as *low quality*. We then randomly selected 40 subjects (20 imaged by Spectralis and 20 imaged by Cirrus) with high quality images to validate the segmentation algorithm.

7.5.2 GTDP Algorithm versus Commercial Software

Fully-automatic segmentation of all Spectralis and Cirrus datasets was performed using the GTDP segmentation algorithm. The datasets were also semi-automatically segmented using commercial software following Section 7.4. To demonstrate that the GTDP algorithm was able to accurately match the segmentation output by both Spectralis and Cirrus software, we compared the following for all patients:

1. Mean TRT and TRV generated automatically by the GTDP algorithm, automatically by Spectralis, and semi-automatically by Spectralis after manual correction of erroneously segmented boundaries.

2. Mean sRT and Spectralis-based retinal volume (sRV) generated automatically by the GTDP algorithm and semi-automatically by Spectralis after manual placement of the OS/RPE.

3. Mean cRT generated automatically by the GTDP algorithm, automatically by Cirrus, and semi-automatically by Cirrus after manual correction of erroneously segmented boundaries.

4. Mean TRT generated automatically by the GTDP algorithm and semi-automatically by Cirrus after manual placement of BM.

We reported the mean and SD for thickness and volume measurements for five of the nine ETDRS sectors, as listed in Table 7.1. We also computed the paired difference (PD) and standard error (SE). Finally, the analysis revealed a constant offset in

Table 7.1: ETDRS grid sectors used to analyze the GTDP algorithm versus commercial software.

Region	**ETDRS Grid Sector**	**Sector Location** (on Figure 7.3)
Central	0 to 1-mm diameter central foveal region	Center
Superior	1 to 3-mm diameter superior region	Middle top
Nasal	1 to 3-mm diameter nasal region	Middle left
Inferior	1 to 3-mm diameter inferior region	Middle bottom
Temporal	1 to 3-mm diameter temporal region	Middle right

the OS/RPE and BM boundary positions when comparing the GTDP algorithm to Spectralis and Cirrus software. Thus when comparing with Spectralis, the OS/RPE and BM boundaries generated by the GTDP algorithm were shifted one pixel externally and one pixel internally to compute the sRT and TRT, respectively. Similarly when comparing with Cirrus, the OS/RPE and BM boundaries from GTDP were shifted five pixels externally and one pixel externally to compute the cRT and TRT, respectively.

7.5.3 Statistical Analysis

Statistical analysis was performed using JMP 9.0.0 (SAS Institute, Cary, NC, USA) and IBM SPSS Statistics 20 (SPSS, Chicago, IL, USA). ICC was used to determine agreement between retinal thickness and volume measurements obtained by the GTDP algorithm and commercial software for each of the comparisons. Bland-Altman plots with 95% limits of agreement (LoA) were also generated to evaluate whether differences in thickness and/or volume measurements depended on the magnitude of the measurement.

7.6 Validation Results

Examples of the automatic GTDP and Spectralis segmentation are shown in Figures 7.4A,C. Quantitative comparisons between the GTDP and Spectralis segmen-

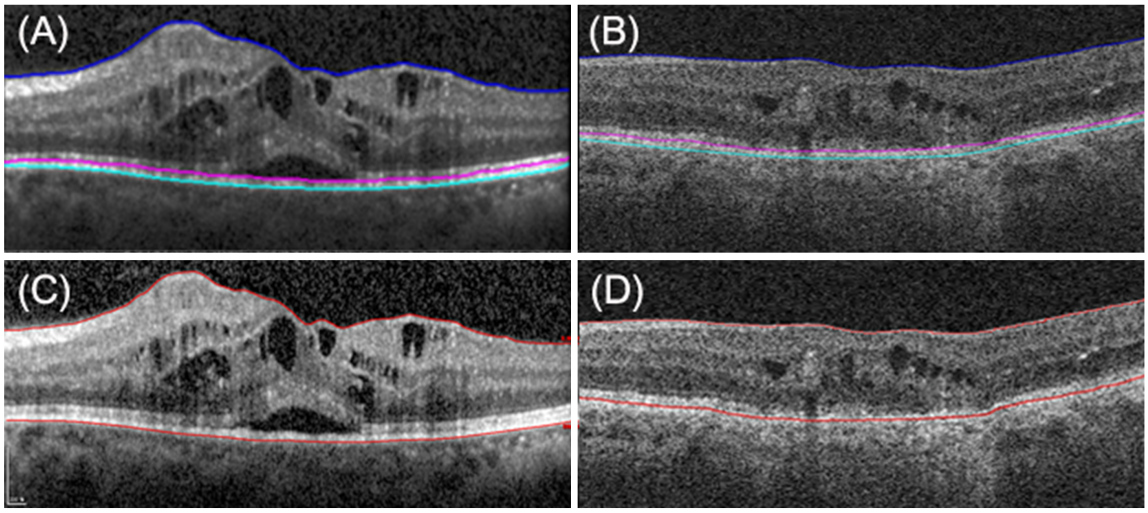

FIGURE 7.4: Automatic multi-platform segmentation results. (A,B) GTDP segmentation, (C) Spectralis segmentation, and (D) Cirrus segmentation.

tation methods for five ETDRS grid regions are shown in Tables 7.2 and 7.3 for TRT and TRV, respectively. Table 7.2 shows that the mean TRT of the central 1-mm region determined by the GTDP, automatic Spectralis, and corrected Spectralis algorithms were 463.8 ± 107.3 µm, 467.0 ± 108.1 µm, and 467.2 ± 109.3 µm. Tables 7.4 and 7.5 show the GTDP versus semi-automatic segmentation results for measuring the sRT and sRV. The mean PD and SE between methods in measuring the sRT for the central 1-mm region was found to be -2.02 ± 1.35 µm with an ICC of 0.998. Tables 7.2 to 7.5 show that there was good agreement for all GTDP and Spectralis measurement comparisons across all quadrants.

Automatic GTDP and Cirrus segmentation is shown in Figures 7.4B,D. Comparison of the cRT measurements generated by the GTDP and Cirrus algorithms is shown in Tables 7.6. The mean 1-mm diameter central foveal subfield cRT was 440.8 ± 183.4 µm, 442.7 ± 182.4 µm, and 442.5 ± 182.9 µm for the automatic GTDP, automatic Cirrus, and semi-automatic Cirrus methods, respectively. The mean cRT of the surrounding regions were all similar except for the superior region which was

Table 7.2: Comparison of mean TRT measurements across 20 subjects determined by the automatic GTDP algorithm, automatic Spectralis software, and semi-automatic Spectralis software after manual correction of errors.

	Total Retinal Thickness (μm)		
Region	Automatic GTDP (Mean ± SD)	Automatic Spectralis (Mean ± SD)	Semi-Automatic Spectralis (Mean ± SD)
Central	463.8 ± 107.3	467.0 ± 108.1	467.2 ± 109.3
Superior	444.1 ± 90.3	442.9 ± 88.6	442.9 ± 89.2
Nasal	420.7 ± 68.7	418.3 ± 66.6	418.9 ± 67.5
Inferior	410.1 ± 63.7	406.5 ± 59.2	405.9 ± 59.8
Temporal	456.9 ± 103.9	457.0 ± 102.7	455.7 ± 103.1
	GTDP vs Automatic Spectralis		
	PD (μm) (Mean ± SE)	ICC (95% CI)	95% LoA
Central	-3.22 ± 1.14	0.999 (0.997 − 0.999)	-5.61 − -0.82
Superior	1.25 ± 1.37	0.998 (0.994 − 0.999)	-1.62 − 4.12
Nasal	2.36 ± 1.66	0.994 (0.985 − 0.998)	-1.10 − 5.83
Inferior	3.71 ± 1.66	0.993 (0.982 − 0.997)	0.24 − 7.19
Temporal	-0.08 ± 1.62	0.998 (0.994 − 0.999)	-3.47 − 3.31
	GTDP vs Corrected Spectralis		
	PD (μm) (Mean ± SE)	ICC (95% CI)	95% LoA
Central	-3.42 ± 0.67	1.000 (0.999 − 1.000)	-4.83 − -2.01
Superior	1.20 ± 1.32	0.998 (0.995 − 0.999)	-1.33 − 2.28
Nasal	1.81 ± 1.58	0.995 (0.986 − 0.998)	1.85 − 9.63
Inferior	4.26 ± 1.60	0.993 (0.983 − 0.997)	6.92 − 16.2
Temporal	1.22 ± 1.65	0.997 (0.994 − 0.999)	2.15 − 8.94

more variable (ICC for all regions except the superior region was $0.993 - 0.999$). In the superior region, the PD (mean ± SE) between the automatic GTDP and Cirrus measurements was 19.47 ± 19.72 μm with an ICC of 0.734 (Table 7.6). An example automated Cirrus segmentation error is shown in Figure 7.5. Finally, Table 7.7 shows the TRT results when comparing the GTDP and semi-automatic Cirrus methods. There was good agreement in all five regions, with an ICC ranging from 0.996-0.999.

Table 7.3: Comparison of mean TRV measurements across 20 subjects determined by the automatic GTDP algorithm, automatic Spectralis software, and semi-automatic Spectralis software after manual correction of errors.

	Total Retinal Volume (mm^3)		
Region	Automatic GTDP (Mean ± SD)	Automatic Spectralis (Mean ± SD)	Semi-Automatic Spectralis (Mean ± SD)
Central	0.37 ± 0.08	0.37 ± 0.09	0.37 ± 0.09
Superior	0.69 ± 0.14	0.70 ± 0.14	0.70 ± 0.14
Nasal	0.66 ± 0.10	0.66 ± 0.10	0.66 ± 0.11
Inferior	0.64 ± 0.10	0.64 ± 0.09	0.64 ± 0.09
Temporal	0.71 ± 0.16	0.72 ± 0.16	0.72 ± 0.16
	GTDP vs Automatic Spectralis		
	PD (mm^3) (Mean ± SE)	ICC (95% CI)	95% LoA
Central	0.000 ± 0.001	0.996 (0.991 − 0.999)	-0.003 − 0.004
Superior	-0.002 ± 0.001	0.999 (0.998 − 1.000)	-0.004 − 0.001
Nasal	-0.003 ± 0.000	0.999 (0.999 − 1.000)	0.002 − 0.005
Inferior	-0.001 ± 0.002	0.996 (0.989 − 0.998)	0.003 − 0.002
Temporal	-0.003 ± 0.002	0.999 (0.997 − 1.000)	-0.001 − 0.007
	GTDP vs Corrected Spectralis		
	PD (mm^3) (Mean ± SE)	ICC (95% CI)	95% LoA
Central	-0.001 ± 0.001	0.998 (0.994 − 0.999)	-0.003 − 0.002
Superior	-0.002 ± 0.001	0.999 (0.998 − 1.000)	-0.005 − 0.001
Nasal	-0.003 ± 0.001	0.999 (0.997 − 1.000)	-0.005 − -0.000
Inferior	-0.001 ± 0.002	0.996 (0.990 − 0.998)	-0.005 − 0.002
Temporal	-0.001 ± 0.002	0.999 (0.998 − 1.000)	-0.004 − 0.002

Table 7.4: Comparison of mean sRT measurements across 20 subjects determined by the automatic GTDP algorithm and the semi-automatic Spectralis software after manual placement of the OS/RPE.

	Spectralis-Based Retinal Thickness (µm)		
Region	Automatic GTDP (Mean ± SD)	Semi-Automatic Spectralis (Mean ± SD)	
Central	441.9 ± 107.9	443.9 ± 108.6	
Superior	424.3 ± 90.1	422.3 ± 88.1	
Nasal	399.0 ± 68.8	396.4 ± 66.1	
Inferior	389.3 ± 63.3	385.2 ± 58.5	
Temporal	436.4 ± 103.9	435.5 ± 102.7	
	GTDP vs Semi-Automatic Spectralis		
	PD (µm) (Mean ± SE)	ICC (95% CI)	95% LoA
Central	-2.02 ± 1.35	0.998 (0.996 − 0.9999)	-4.84 − 0.80
Superior	1.99 ± 1.53	0.997 (0.993 − 0.999)	-1.21 − 5.19
Nasal	2.64 ± 1.79	0.993 (0.982 − 0.997)	-1.12 − 6.39
Inferior	4.14 ± 2.20	0.987 (0.967 − 0.995)	-0.45 − 8.74
Temporal	0.87 ± 1.50	0.998 (0.995 − 0.999)	-2.26 − 4.01

7.7 Discussion

The thickness and volume measurements were similar for all GTDP and Spectralis and all GTDP and Cirrus method comparisons, with the exception of the superior region in the cRT comparison (Table 7.6). This difference in the superior subfield was likely due to significant errors in the Cirrus automated segmentation for one of the subjects (Figure 7.5A), as after manual correction of these errors (Figure 7.5B), the mean cRT determined by GTDP and Cirrus were nearly identical (ICC: 0.999; Table 7.6). There were also no reproducible systematic thickness differences as a function of retinal thickness magnitude. Quantitative evaluation of the frequency of segmentation errors on different software platforms was not conducted in this study.

This study specifically analyzed eyes with DME, however macular edema caused by other diseases such as retinal vein occlusion, uveitis, and neovascular AMD can

Table 7.5: Comparison of mean sRV measurements across 20 subjects determined by the automatic GTDP algorithm and the semi-automatic Spectralis software after manual placement of the OS/RPE.

	Spectralis-Based Retinal Volume (mm^3)		
Group	Automatic GTDP (Mean ± SD)	Semi-Automatic Spectralis (Mean ± SD)	
Central	0.35 ± 0.08	0.35 ± 0.08	
Superior	0.65 ± 0.14	0.66 ± 0.14	
Nasal	0.62 ± 0.10	0.62 ± 0.10	
Inferior	0.59 ± 0.09	0.60 ± 0.10	
Temporal	0.68 ± 0.16	0.68 ± 0.16	
	GTDP vs Semi-Automatic Spectralis		
	PD (mm^3) (Mean ± SE)	ICC (95% CI)	95% LoA
Central	0.001 ± 0.001	0.999 (0.998 − 1.000)	-0.007 − 0.003
Superior	-0.001 ± 0.002	0.999 (0.997 − 1.000)	-0.005 − -0.002
Nasal	-0.002 ± 0.002	0.997 (0.992 − 0.999)	-0.006 − 0.002
Inferior	-0.001 ± 0.003	0.992 (0.980 − 0.997)	-0.006 − -0.005
Temporal	-0.000 ± 0.002	0.999 (0.998 − 1.000)	-0.004 − 0.003

also be assessed quantitatively with OCT [195]. Thus, we anticipate that our automatic GTDP algorithm will be similarly useful in determining retinal thickness and volume in eyes with other macular edema-related conditions. Future studies will be aimed at applying our GTDP algorithm to eyes with macular edema from these various conditions.

We showed previously that the GTDP segmentation algorithm could automatically segment the NFL, GCL-IPL, INL, OPL, ONL-ISM, ISE-OS, and RPE layers on SD-OCT images of normal eyes and eyes with non-neovascular AMD [56, 57]. In this chapter, we automatically segmented the ILM, OS/RPE, and BM boundaries to calculate mean retinal and TR thicknesses and volumes for eyes with DME. Thickness abnormalities of the NFL and GCL have been associated with visual function in eyes with optic neuropathies such as optic neuritis. Abnormal external limiting

Table 7.6: Comparison of mean cRT measurements across 20 subjects determined by the automatic GTDP algorithm, automatic Cirrus software, and semi-automatic Cirrus software after manual correction of errors.

	Cirrus-Based Retinal Thickness (µm)		
Region	Automatic GTDP (Mean ± SD)	Automatic Cirrus (Mean ± SD)	Semi-Automatic Cirrus (Mean ± SD)
Central	440.8 ± 183.4	442.7 ± 182.4	442.5 ± 182.9
Superior	410.7 ± 142.7	391.3 ± 139.9	411.2 ± 139.9
Nasal	409.2 ± 131.5	408.6 ± 128.3	408.7 ± 128.2
Inferior	405.4 ± 148.6	402.6 ± 142.8	401.8 ± 141.0
Temporal	416.2 ± 170.3	411.0 ± 154.7	415.5 ± 165.7
	GTDP vs Automatic Cirrus		
	PD (µm) (Mean ± SE)	ICC (95% CI)	95% LoA
Central	-1.84 ± 1.65	0.999 (0.998 − 1.000)	-5.30 − 1.61
Superior	19.47 ± 19.72	0.734 (0.441 − 0.886)	-21.80 − 60.75
Nasal	0.61 ± 1.70	0.998 (0.996 − 0.999)	-2.94 − 4.17
Inferior	2.83 ± 2.10	0.998 (0.995 − 0.999)	-1.57 − 7.24
Temporal	5.16 ± 4.16	0.993 (0.984 − 0.997)	-3.55 − 13.9
	GTDP vs Corrected Cirrus		
	PD (µm) (Mean ± SE)	ICC (95% CI)	95% LoA
Central	-2.24 ± 1.16	1.000 (0.999 − 1.000)	-4.67 − 0.18
Superior	-0.48 ± 1.57	0.999 (0.997 − 1.000)	-3.77 − 2.81
Nasal	0.46 ± 1.78	0.998 (0.995 − 0.999)	-3.25 − 4.18
Inferior	3.63 ± 2.49	0.997 (0.993 − 0.999)	-1.57 − 8.84
Temporal	0.71 ± 1.68	0.999 (0.997 − 1.000)	-2.80 − 4.23

Table 7.7: Comparison of mean TRT measurements across 20 subjects determined by the automatic GTDP algorithm and the semi-automatic Cirrus software after manual placement of BM.

	Total Retinal Thickness (μm)		
Region	Automatic GTDP (Mean ± SD)	Semi-Automatic Cirrus (Mean ± SD)	
Central	459.0 ± 183.8	463.0 ± 184.8	
Superior	428.9 ± 143.5	428.9 ± 140.6	
Nasal	428.1 ± 131.7	428.3 ± 127.9	
Inferior	423.2 ± 148.8	420.8 ± 141.2	
Temporal	434.4 ± 171.0	435.0 ± 168.2	
	GTDP vs Semi-Automatic Cirrus		
	PD (μm) (Mean ± SE)	ICC (95% CI)	95% LoA
Central	-4.05 ± 1.45	0.999 (0.998 − 1.000)	-7.08 − -1.01
Superior	0.00 ± 1.72	0.999 (0.996 − 0.999)	-3.61 − 1.72
Nasal	-0.19 ± 2.61	0.996 (0.990 − 0.998)	-5.66 − 5.28
Inferior	2.44 ± 2.86	0.996 (0.990 − 0.998)	3.56 − 8.43
Temporal	-0.62 ± 1.74	0.999 (0.997 − 1.000)	-4.26 − 3.03

membrane, IS/OS junction integrity, and ONL thickness have been associated with decreased visual acuity. Assessment of these retinal layers is beyond the current scope of our study and will be addressed in future studies.

Further limitations to this study include the relatively high image quality of the validation dataset which facilitated retinal boundary identification. In practice, factors such as media opacity or patient motion could degrade the image quality, thus potentially compromising automatic segmentation accuracy [43, 196, 197]. The performance of our algorithm on these types images remains to be determined. Another limitation is that the patients imaged by Spectralis and Cirrus were not the same. We are currently collecting data where the same subject is imaged on both systems during the same session to facilitate direct comparison of thickness measurements.

Analysis of the retinal and total retinal thickness and volume was determined for

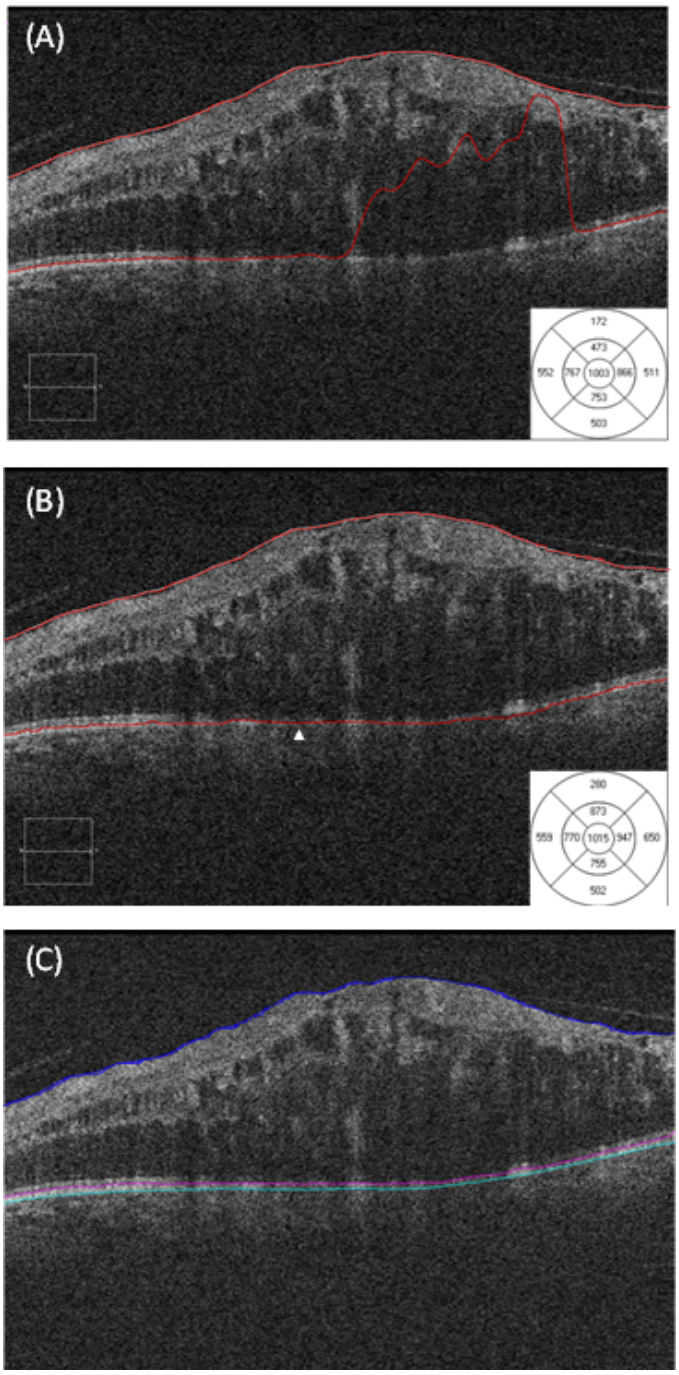

FIGURE 7.5: An example segmentation error produced by the Cirrus software. (A) Erroneous outer retinal boundary resulted in an incorrect mean cRT measurement of 473 µm in the superior region. (B) Accurate outer retinal boundary after manual correction yielded a mean cRT of 873 µm. (C) Accurate outer retinal boundary automatically segmented by the GTDP algorithm.

eyes with DME using images obtained by Spectralis and Cirrus, two commonly used OCT systems. The performance of our GTDP algorithm is not yet known for other SD-OCT systems. Regardless, the high degree of agreement in thickness and volume between the GTDP algorithm and commercial software is encouraging.

7.8 Conclusion

We developed an algorithm based on GTDP to automatically segment three retinal layer boundaries of eyes with DME imaged by Spectralis and Cirrus systems. The algorithm was able to extract retinal and total retinal thickness and volume measurements which were in agreement with the commercial systems' software. The ability to extract quantitative layer information from images acquired by two different manufacturers suggests that the GTDP algorithm may be useful in clinics or in DME trials where the SD-OCT imaging system manufacturer cannot be controlled.

8

Beyond Segmentation and Future Work: Kernel Regression-Based Classification

While our GTDP segmentation framework has proven to be an effective tool for identifying ophthalmic imaging biomarkers, additional methods may be necessary to facilitate search region limitation (Section 2.1.3) or pilot structure estimation (Section 2.2.1). This is especially the case for images of diseased states, where oftentimes pathologies severely complicate the underlying tissue structure. We therefore developed a *kernel regression-based classification* method to tentatively identify the structures of interest. We then use these estimates to guide GTDP framework for more accurate segmentation results.

Sections 8.1 and 8.2 provide an overview on kernel regression [189] and classification [198, 199] as individual methods. As part of our ongoing work, we then build upon these techniques in Section 8.3 to describe an integrated kernel regression-based classification method for improved feature identification. Finally, an implementation of this method is described in Chapter 9.

8.1 Kernel Regression: An Overview

Kernel regression is a non-parametric (data-driven) method for deriving local estimates of a function with a kernel that weights the relative importance of nearby points [189]. Following the work of Takeda *et al.* [189], we provide an overview on the second order iterative Gaussian steering kernel regression method for image denoising. For a more generalized description of the kernel regression framework, refer to Takeda *et al.* [189].

8.1.1 Problem Formulation

Looking at a small patch of P pixels on a noisy image $\boldsymbol{I} \in \mathbb{R}^{M \times N}$, the intensity y_p of a pixel can be described by

$$y_p = f(\boldsymbol{z}_p) + n_p, \quad p = 1, \ldots, P, \tag{8.1}$$

where $\boldsymbol{z}_p = [i_p, j_p]^T$ is the p^{th} pixel located at row i and column j on $\boldsymbol{I}$, $f(\cdot)$ is an unspecified (non-parametric) regression function, and n_p is an independent and identically distributed zero-mean noise value at $\boldsymbol{z}_p$. Using this formulation, we can obtain a local estimate of the regression function, $\hat{f}(\boldsymbol{z})$, to generate a denoised image $\hat{\boldsymbol{I}}$.

If we assume $\hat{\boldsymbol{I}}$ is locally smooth, then we can approximate $f(\boldsymbol{z}_p)$ using the second order Taylor series expansion about a point $\boldsymbol{z}$ near $\boldsymbol{z}_p$ following

$$\begin{aligned} f(\boldsymbol{z}_p) &\approx f(\boldsymbol{z}) + \left[\bigtriangledown f(\boldsymbol{z})\right]^T (\boldsymbol{z}_p - \boldsymbol{z}) \\ &\quad + \frac{1}{2}(\boldsymbol{z}_p - \boldsymbol{z})^T \left[\mathcal{H} f(\boldsymbol{z})\right] (\boldsymbol{z}_p - \boldsymbol{z}) \\ &= f(\boldsymbol{z}) + \left[\bigtriangledown f(\boldsymbol{z})\right]^T (\boldsymbol{z}_p - \boldsymbol{z}) \\ &\quad + \frac{1}{2}\mathrm{vec}^T \left[\mathcal{H} f(\boldsymbol{z})\right] \mathrm{vec}\left[(\boldsymbol{z}_p - \boldsymbol{z})(\boldsymbol{z}_p - \boldsymbol{z})^T\right] \\ &= \beta_0 + \boldsymbol{\beta}_1^T (\boldsymbol{z}_p - \boldsymbol{z}) + \boldsymbol{\beta}_2^T \mathrm{vech}\left[(\boldsymbol{z}_p - \boldsymbol{z})(\boldsymbol{z}_p - \boldsymbol{z})^T\right], \end{aligned} \tag{8.2}$$

where

$$\bigtriangledown = \begin{bmatrix} \dfrac{\partial f}{\partial i} \\ \dfrac{\partial f}{\partial j} \end{bmatrix} \qquad \mathcal{H} = \begin{bmatrix} \dfrac{\partial^2 f}{\partial i^2} & \dfrac{\partial^2 f}{\partial i \partial j} \\ \dfrac{\partial^2 f}{\partial j \partial i} & \dfrac{\partial^2 f}{\partial j^2} \end{bmatrix} \tag{8.3}$$

$$\text{vec}\left(\begin{bmatrix} a & c \\ b & d \end{bmatrix}\right) = \begin{bmatrix} a \\ b \\ c \\ d \end{bmatrix} \qquad \text{vech}\left(\begin{bmatrix} a & b \\ b & c \end{bmatrix}\right) = \begin{bmatrix} a \\ b \\ c \end{bmatrix} \tag{8.4}$$

$$\beta_0 = f(\boldsymbol{z}) \qquad \boldsymbol{\beta}_1 = \begin{bmatrix} \dfrac{\partial f(\boldsymbol{z})}{\partial i} \\ \dfrac{\partial f(\boldsymbol{z})}{\partial j} \end{bmatrix} \qquad \boldsymbol{\beta}_2 = \frac{1}{2}\left[\frac{\partial^2 f(\boldsymbol{z})}{\partial i^2}, \quad \frac{\partial^2 f(\boldsymbol{z})}{\partial i \partial j}, \quad \frac{\partial^2 f(\boldsymbol{z})}{\partial j^2}\right]^T. \tag{8.5}$$

8.1.2 Linear Least Squares

We can solve for the unknowns (β_0, $\boldsymbol{\beta}_1$, and $\boldsymbol{\beta}_2$) using a weighted linear least squares formulation [189, 200] following

$$\underset{\beta_0, \boldsymbol{\beta}_1, \boldsymbol{\beta}_2}{\text{argmin}} \sum_{k=1}^{P} \left[\left(y_p - \beta_0 - \boldsymbol{\beta}_1^T (\boldsymbol{z}_p - \boldsymbol{z}) - \boldsymbol{\beta}_2^T \text{vech}\left[(\boldsymbol{z}_p - \boldsymbol{z})(\boldsymbol{z}_p - \boldsymbol{z})^T \right] \right)^2 \hat{\boldsymbol{K}}(\boldsymbol{z}_p - \boldsymbol{z}) \right], \tag{8.6}$$

where $\hat{\boldsymbol{K}}(\cdot)$ is a normalized kernel function used to weight the P observations. Rewriting Equation (8.6) in matrix form yields

$$\hat{\boldsymbol{b}} = \underset{\boldsymbol{b}}{\text{argmin}} \left[(\boldsymbol{y} - \boldsymbol{X}\boldsymbol{b})^T \boldsymbol{D}_{\hat{\boldsymbol{K}}} (\boldsymbol{y} - \boldsymbol{X}\boldsymbol{b}) \right], \tag{8.7}$$

where

$$\begin{aligned}
\boldsymbol{y} &= [y_1, y_2, \ldots, y_P]^T \\
\boldsymbol{b} &= [\beta_0,\ \boldsymbol{\beta}_1^T,\ \boldsymbol{\beta}_2^T]^T \\
\boldsymbol{D}_{\hat{\boldsymbol{K}}} &= \text{diag}[\ \hat{\boldsymbol{K}}(\boldsymbol{z}_1 - \boldsymbol{z}),\ \hat{\boldsymbol{K}}(\boldsymbol{z}_2 - \boldsymbol{z}),\ \ldots,\ \hat{\boldsymbol{K}}(\boldsymbol{z}_P - \boldsymbol{z})\ ] \\
\boldsymbol{X} &= \begin{bmatrix} 1 & (\boldsymbol{z}_1 - \boldsymbol{z})^T & \text{vech}[(\boldsymbol{z}_1 - \boldsymbol{z})(\boldsymbol{z}_1 - \boldsymbol{z})^T] \\ 1 & (\boldsymbol{z}_2 - \boldsymbol{z})^T & \text{vech}[(\boldsymbol{z}_2 - \boldsymbol{z})(\boldsymbol{z}_2 - \boldsymbol{z})^T] \\ \vdots & \vdots & \vdots \\ 1 & (\boldsymbol{z}_P - \boldsymbol{z})^T & \text{vech}[(\boldsymbol{z}_P - \boldsymbol{z})(\boldsymbol{z}_P - \boldsymbol{z})^T] \end{bmatrix}.
\end{aligned} \tag{8.8}$$

Since Equation (8.7) is a linear least squares formulation, the solution [189, 200] can therefore be given by

$$\hat{\boldsymbol{b}} = (\boldsymbol{X}^T \boldsymbol{D}_{\hat{\boldsymbol{K}}} \boldsymbol{X})^{-1} \boldsymbol{X}^T \boldsymbol{D}_{\hat{\boldsymbol{K}}} \boldsymbol{X} \boldsymbol{y}, \tag{8.9}$$

where $\hat{\boldsymbol{I}}(\boldsymbol{z}) = \hat{y_p}(\boldsymbol{z}) = \hat{\beta}_0(\boldsymbol{z})$ is the denoised estimate of $\boldsymbol{I}(\boldsymbol{z})$.

8.1.3 Select Kernel Functions

While many different kernel functions exist, we focus on the iterative adaptive Gaussian steering kernel ($\boldsymbol{K}_{iGS}$) from Takeda *et al.* [189] due to its superior performance compared to other techniques [189]. We describe this kernel and all other relevant kernels in the following subsections. To then apply these kernels $\boldsymbol{K}$ to Section 8.1.2 as a weighting function, they should first be linearly normalized following

$$\hat{\boldsymbol{K}} = \frac{\boldsymbol{K}}{\|\boldsymbol{K}\|}. \tag{8.10}$$

Classic Gaussian Kernel

For $\boldsymbol{z}_p = [i_p, j_p]^T$ and $\boldsymbol{z} = [i, j]^T$, the 2D Gaussian kernel is described by

$$\boldsymbol{K}_G(\boldsymbol{z}_p - \boldsymbol{z}) = \exp\left[-\left(\frac{(i_p - i)^2}{2h_i^2} + \frac{(j_p - j)^2}{2h_j^2} \right) \right], \tag{8.11}$$

where h_i and h_j are the standard deviations of the Gaussian function in the i and j dimensions, respectively.

Adaptive Gaussian Steering Kernel

The adaptive Gaussian steering kernel $\boldsymbol{K}_{GS}$ [189] can be described as a Gaussian function that is elongated (σ), rotated (θ), and scaled (γ) to reduce blurring when used as an image filter. For example, a wider and more isotropic Gaussian function is used to filter smoother image regions, while a longer and narrower Gaussian oriented along an edge is used to filter the edge.

The Gaussian steering kernel can be computed for a pixel $\boldsymbol{z}$ in two steps. First, we obtain estimates of the image gradients $\boldsymbol{G}_i$ and $\boldsymbol{G}_j$ along the i and j dimensions, respectively (e.g. the estimate of $\boldsymbol{\beta}_1$ using the classic Gaussian kernel regression method). Second, we compute the truncated singular value decomposition [201] of the gradient information [189, 202] following

$$\begin{bmatrix} \boldsymbol{G}_i(\boldsymbol{z}_1) & \boldsymbol{G}_j(\boldsymbol{z}_1) \\ \boldsymbol{G}_i(\boldsymbol{z}_2) & \boldsymbol{G}_j(\boldsymbol{z}_2) \\ \vdots & \vdots \\ \boldsymbol{G}_i(\boldsymbol{z}_P) & \boldsymbol{G}_j(\boldsymbol{z}_P) \end{bmatrix} = \boldsymbol{U}\boldsymbol{S}\boldsymbol{V}^T. \tag{8.12}$$

This information is used to compute the steering parameters (θ, σ, and γ) [189], where

$$\begin{gathered} \boldsymbol{S} = \begin{bmatrix} s_1 & 0 \\ 0 & s_2 \end{bmatrix} \quad \boldsymbol{V} = \begin{bmatrix} V_{11} & V_{12} \\ V_{21} & V_{22} \end{bmatrix} \\ \theta = \arctan\left(\frac{V_{12}}{V_{22}}\right) \quad \sigma = \frac{s_1 + \lambda'}{s_2 + \lambda'} \quad \gamma = \left(\frac{s_1 \cdot s_2 + \lambda''}{P}\right)^{\frac{1}{2}}, \end{gathered} \tag{8.13}$$

and λ' and λ'' are parameters that prevent undefined or zero values for σ and γ. The resulting Gaussian steering kernel with a global smoothing parameter h is defined as

$$\boldsymbol{K}_{GS}(\boldsymbol{z}_p - \boldsymbol{z}) = \exp\left[-\frac{(\boldsymbol{z}_p - \boldsymbol{z})^T \boldsymbol{\Sigma} (\boldsymbol{z}_p - \boldsymbol{z})}{2h^2}\right], \tag{8.14}$$

where

$$\boldsymbol{\Sigma} = \gamma \boldsymbol{\Theta} \boldsymbol{\Lambda} \boldsymbol{\Theta}^T \qquad \boldsymbol{\Theta} = \begin{bmatrix} \cos\theta & \sin\theta \\ -sin\theta & \cos\theta \end{bmatrix} \qquad \boldsymbol{\Lambda} = \begin{bmatrix} \sigma & 0 \\ 0 & \sigma^{-1} \end{bmatrix}. \tag{8.15}$$

Iterative Adaptive Gaussian Steering Kernel

The Gaussian steering kernel $\boldsymbol{K}_{GS}$ can be iteratively improved to upon by refining the steering parameters based on improved estimates of $\boldsymbol{G}_i$ and $\boldsymbol{G}_j$ [189]. More specifically, the resulting estimate of $\boldsymbol{\beta}_1$ from the Gaussian steering kernel regression method can be used to update $\boldsymbol{G}_i$ and $\boldsymbol{G}_j$. The steering parameters are then recalculated using the new gradients to create an improved kernel $\boldsymbol{K}_{iGS}$. This process can be repeated in an iterative fashion until the desired level of denoising is achieved.

8.2 Classification: An Overview

In image processing, classification refers to a set of techniques which aim to categorize pixels into specific groups or classes [198, 199]. Many of these methods are a subset of supervised machine learning, where the classifier is first learned from a training dataset [199]. For example, an OCT retinal layer classifier can be generated based on a set of manually segmented images. The classifier can subsequently be used to identify retinal layers on new datasets. In this section, we provide an overview of the relevant classification techniques used in this dissertation.

8.2.1 Features

In order to classify a pixel $\boldsymbol{z}$, the pixel needs to have associated *features* (descriptors), where each feature v is represented by a single value and a group of L features make up a feature vector $\boldsymbol{v} = [v_1, v_2, \ldots v_L]$. Basic features include pixel intensity, gradient, and location. The texture of an image can also be characterized by features using methods such as co-occurrence matrices [203–206] or Laws' Texture Energy Measures [206, 207], which is described below.

Laws' Texture Energy Measures

The texture of an image $\boldsymbol{I}$ can be described by the spatial variation of its pixel intensities [206]. Laws developed a method to extract textural features using spatial filtering [207]. This is done by first high-pass filtering the image to remove low frequency content following

$$\boldsymbol{H} = \boldsymbol{I} - (\boldsymbol{I} * \boldsymbol{F}_{mean}), \tag{8.16}$$

where $\boldsymbol{F}_{mean}$ is a mean filter and $\boldsymbol{H}$ is the high-pass filtered image. Next, four textural 1D filters defined by

$$\begin{aligned} L5 &= \begin{bmatrix} +1 & +4 & +6 & +4 & +1 \end{bmatrix} \quad \text{(Level)} \\ E5 &= \begin{bmatrix} -1 & -2 & 0 & +2 & +1 \end{bmatrix} \quad \text{(Edge)} \\ S5 &= \begin{bmatrix} -1 & 0 & +2 & 0 & -1 \end{bmatrix} \quad \text{(Spot)} \\ R5 &= \begin{bmatrix} +1 & -4 & +6 & -4 & +1 \end{bmatrix} \quad \text{(Ripple),} \end{aligned} \tag{8.17}$$

are used to generate 16 2D filters following

$$\begin{array}{cccc} L5^T L5 & E5^T L5 & S5^T L5 & R5^T L5 \\ L5^T E5 & E5^T E5 & S5^T E5 & R5^T E5 \\ L5^T S5 & E5^T S5 & S5^T S5 & R5^T S5 \\ L5^T R5 & E5^T R5 & S5^T R5 & R5^T R5. \end{array} \tag{8.18}$$

Symmetric filter pairs are then averaged to generate nine filters ($\boldsymbol{F}_{Ln} \in \mathbb{R}^{5\times5}$) as shown in Equation (8.19), where each filter extracts a particular texture characteristic. For example, $\boldsymbol{F}_{L1}$ extracts edges while $\boldsymbol{F}_{L2}$ locates spots.

$$\begin{array}{lll} \boldsymbol{F}_{L1} = (L5^T E5 + E5^T L5)/2 & \boldsymbol{F}_{L4} = E5^T E5 & \boldsymbol{F}_{L5} = (E5^T S5 + S5^T E5)/2 \\ \boldsymbol{F}_{L2} = (L5^T S5 + S5^T L5)/2 & \boldsymbol{F}_{L7} = S5^T S5 & \boldsymbol{F}_{L6} = (E5^T R5 + R5^T E5)/2 \\ \boldsymbol{F}_{L3} = (L5^T R5 + R5^T L5)/2 & \boldsymbol{F}_{L9} = R5^T R5 & \boldsymbol{F}_{L8} = (S5^T R5 + R5^T S5)/2 \end{array} \tag{8.19}$$

Sixteen textural features $\{v_n\}_{n=1}^{16}$ can then be computed for a pixel $\boldsymbol{z} = [i, j]^T$ on $\boldsymbol{I}$, where

$$v_n = \frac{1}{25} \sum_{j=-2}^{2} \sum_{i=-2}^{2} \Big(\boldsymbol{H}[\boldsymbol{z} + i, \boldsymbol{z} + j] \boldsymbol{F}_{Ln}[3 - i, 3 - j] \Big). \tag{8.20}$$

8.2.2 Classes

The groups or categories output by a classifier are called *classes*. Example classes for an OCT retinal layer classifier include the NFL, RPE, and any other layers visible on OCT images. In supervised classification, a set of K classes $\boldsymbol{C} = \{C_k\}_{k=1}^{K}$ is pre-defined for a given classifier [199].

8.2.3 Classifier

Given an image $\boldsymbol{I} \in \mathbb{R}^{M \times N}$, we wish to define a classifier $\phi(\cdot)$ which estimates the class $\hat{c}$ of a pixel $\boldsymbol{z}$ following

$$\hat{c} = \phi(\boldsymbol{v}), \tag{8.21}$$

where $\boldsymbol{z} = [i, j]^T$ is a pixel located at row i and column j of $\boldsymbol{I}$, $\boldsymbol{v}$ is the feature vector of $\boldsymbol{z}$, $\hat{c} \in \boldsymbol{C}$ is the estimated class of $\boldsymbol{z}$, and $c \in \boldsymbol{C}$ is the true class of $\boldsymbol{z}$.

Provided that the training dataset is composed of n images $\in \mathbb{R}^{M \times N}$, we have a total of $T = nMN$ training pixels. The feature vectors for all T pixels are then combined into a feature vector set $\boldsymbol{V} = [{\boldsymbol{v}_1}^T, {\boldsymbol{v}_2}^T, \ldots, {\boldsymbol{v}_T}^T]^T \in \mathbb{R}^{T \times L}$. For each class C_k, a feature vector subset $\boldsymbol{V}_k \subseteq \boldsymbol{V}$ is defined where $\boldsymbol{V}_k = \{\boldsymbol{v} \in \boldsymbol{V} \mid c = C_k\} \in \mathbb{R}^{T_k \times L}$. From this definition, it can be seen that $T_k \leqslant T$ and $\sum_{k=1}^{K} T_k = T$.

While many classifier types exist, the nearest neighbor classifier is one of the most intuitive and well-known classifiers [199]. Using the *minimum Euclidean distance* as the distance measure, the nearest neighbor classifier is defined as

$$\hat{c} = \phi(\boldsymbol{v}) = \left\{ C_k \in \boldsymbol{C} \mid \underset{k}{\operatorname{argmin}} \sqrt{(\boldsymbol{v} - \boldsymbol{\mu}_k)(\boldsymbol{v} - \boldsymbol{\mu}_k)^T} \right\}. \tag{8.22}$$

where $\boldsymbol{\mu}_k \in \mathbb{R}^{1\times L}$ is the mean feature vector for the training set $\boldsymbol{V}_k$ following

$$\boldsymbol{\mu}_k[l] = \frac{1}{T_k}\sum_{t=1}^{T_k} \boldsymbol{V}_k[t,l], \quad l = 1\ldots L. \tag{8.23}$$

8.2.4 Feature Selection

Since not all features in $\boldsymbol{v}$ may be useful for predicting the true class c, we can reduce the dimension of $\boldsymbol{v}$ by defining a subset $\boldsymbol{v}' \subseteq \boldsymbol{v}$ of length L' containing only the most relevant features [208–210]. Because the brute force method for finding the optimal features of an unknown length L' is generally insurmountable, many methods have been developed to perform non-exhaustive searches [208]. While these feature selection methods may result in suboptimal solutions, they are oftentimes sufficient for classification purposes.

Sequential forward feature selection (SFFS) is a commonly used method where features as added to $\boldsymbol{v}'$ sequentially [209]. While the solution may reside at a local minimum rather than the global optimum, this technique is still popular due to its computational speed and interpretability of results. In SFFS, $\boldsymbol{v}'$ begins as a null set. Features are added to $\boldsymbol{v}'$ in a sequential manner, where with each addition the selected feature minimizes a predefined criterion function $E(\cdot)$. An example criterion function is shown in Equation (8.24), where $E(\cdot)$ is a measure of the misclassification rate of a set of training feature vectors $\boldsymbol{V}' = [\boldsymbol{v}_1'^T, \boldsymbol{v}_2'^T, \ldots, \boldsymbol{v}_T'^T]^T \in \mathbb{R}^{T\times L'}$ and c_t is the true class for $\boldsymbol{v}_t$ and $\boldsymbol{v}_t'$. Typically features are added until the output of the criterion function begins to increase.

$$E(\boldsymbol{V}') = T - \sum_{t=1}^{T} \left[\phi(\boldsymbol{v}_t') - c_t\right]^0 \tag{8.24}$$

In order to reduce overfitting of the classifier, validation methods such as K-fold cross-validation [211] may also be used during feature selection. In this scenario, the

training data is split into K subsets. One subset is used as the validation dataset during feature selection, and the remaining subsets are used to train the classifier. This process is repeated K times until all subsets have served as the validation dataset. The accuracy of cross-validation and other methods are discussed in the literature [212–214].

8.3 Kernel Regression-Based Classification

In this section, we integrate the kernel regression and classification methods in Sections 8.1 and 8.2 as a means to more accurately classify images. Below is a detailed outline of the KR-based classification steps, and Chapter 9 presents an implementation of this method.

1. Define a set of classes $\boldsymbol{C}$ and manually classify a training dataset to generate a true class c for each training pixel $\boldsymbol{z}$.

2. Denoise the training images using the KR method as described in Section 8.1, making sure to keep track of the kernel information for each pixel (e.g. for each pixel $\boldsymbol{z}$, keep all values of $\hat{\boldsymbol{K}}(\boldsymbol{z}_p - \boldsymbol{z})$ for $p = [1, \ldots, P]$).

3. Compute the feature vectors for all training pixels as described in Section 8.2.1.

   (a) The kernels from Step 2 can be used as features themselves (e.g. β_0, $\boldsymbol{\beta}_1$, $\boldsymbol{\beta}_2$, kernel height, kernel width, and kernel area). These are new classification features that would have otherwise not been available without using the KR method.

   (b) Use the kernels from Step 2 to calculate feature values using a weighted average of neighboring pixels. For example, if the l^{th} feature is image intensity, then for a pixel $\boldsymbol{z}$ with P neighboring pixels $\{\boldsymbol{z}_p\}_{p=1}^{P}$, the feature

value can be computed following

$$\boldsymbol{v}[l] = \sum_{p=1}^{P} \Big(\boldsymbol{K}(\boldsymbol{z}_p - \boldsymbol{z}) \boldsymbol{I}[\boldsymbol{z}_p] \Big). \tag{8.25}$$

This reduces the effects of noise while preserving edge information.

(c) For the training feature vector set $\boldsymbol{V}$, normalize each feature across all training vectors following

$$\hat{\boldsymbol{V}}_l = \frac{\boldsymbol{V}_l}{\|\boldsymbol{V}_l\|}, \quad l = 1, \ldots, L, \tag{8.26}$$

where $\boldsymbol{V}_l$ and $\hat{\boldsymbol{V}}_l$ are the l^{th} columns in $\boldsymbol{V}$ and $\hat{\boldsymbol{V}}_l$, respectively. This allows for features to be fairly compared when using the minimum distance classifier. In cases where feature values are not linearly distributed, other methods such as the logarithm, exponential, histogram equalization may be used to evenly distribute the values.

4. Perform weighted SFFS, where features are individually weighted to provide a more accurate class prediction.

(a) Define a set of A possible weight values $\boldsymbol{a} = [a_1, a_2, \ldots, a_A]$ for the features.

(b) Given $\hat{\boldsymbol{V}} \in \mathbb{R}^{T \times L}$, create a new set of weighted feature vectors $\hat{\boldsymbol{V}}_A = [a_1 \hat{\boldsymbol{V}}, a_2 \hat{\boldsymbol{V}}, \ldots, a_A \hat{\boldsymbol{V}}] \in \mathbb{R}^{T \times LA}$.

(c) Perform SFFS on $\hat{\boldsymbol{V}}_A$ as described in Section 8.2.4 to find a subset of "optimally" weighted features. The result is a set of training feature vectors $\hat{\boldsymbol{V}}' \subseteq \hat{\boldsymbol{V}}$ and weights $\boldsymbol{\omega} = [\omega_1, \omega_2, \ldots, \omega_{L'}]$, where $\hat{\boldsymbol{V}}' \in \mathbb{R}^{T \times L'}$ and $\omega_l \in \boldsymbol{a}$.

5. Create a classifier with weighted features to classify the feature vectors. For example, the nearest neighbor classifier computed using the *minimum weighted distance* can be used, where

$$\hat{c} = \phi(\boldsymbol{v}) = \left\{ C_k \in \boldsymbol{C} \mid \underset{k}{\operatorname{argmin}} \sqrt{[\boldsymbol{\omega} \circ a(\boldsymbol{v} - \boldsymbol{\mu}_k)] \, [\boldsymbol{\omega} \circ (\boldsymbol{v} - \boldsymbol{\mu}_k)]^T} \right\}. \quad (8.27)$$

6. Gauge the performance of the classifier, classify the training feature vectors using Equation (8.27) and measure the classification error using a criterion function such as the one in Equation (8.24). If the classifier is unsatisfactory, then modify the criterion function until the desired classification is achieved.

9

Future Work: OCT Biomarkers of DME

9.1 Motivation

Diabetic retinopathy is a leading cause of blindness among working-aged adults in the United States [215] and affects approximately 93 million people worldwide [216]. Among those affected, approximately 21 million people develop diabetic macular edema [216]. DME results from the breakdown of the blood-retinal barrier as retinal vascular endothelial cells become damaged from chronic hyperglycemia, causing plasma exudation into the extracellular space of the neurosensory retina [217]. This leads to retinal hypoxia and increased production of vascular endothelial growth factor (VEGF) [217–219], which further progresses DME through mechanisms such as cytotoxic damage to the cells that reabsorb fluid from the retina back into the vascular system. RPE cells, for example, absorb fluid from the subretinal space, while Müller cells reabsorb fluid from the intraretinal space [220, 221]; damage to the RPE cells is therefore believed to be associated with subretinal fluid [222, 223], while Müller cell swelling from imbalanced fluid transport is believed to cause cystoid edema [220, 221]. Thus, the volume and type of DME is related to a dynamic process of pathologic plasma leakage into the retina and dysfunctional fluid pumping out of

the retina. Ultimately, the persistence of fluid in the retina leads to vision loss.

Randomized controlled clinical trials conducted in the 1980's for DME treatments demonstrated that focal laser (ablation of vascular leakage sites) and grid pattern laser (targeting the RPE under a thickened retina) were effective in many cases [224]. More recently, numerous trials have shown that intravitreal anti-VEGF therapies (pegaptanib, ranibizumab, and VEGF-Trap) are generally more effective than laser [225–229]. Furthermore, eyes that fail laser therapy often respond well to anti-VEGF or corticosteroid therapies [230, 231]. While these and other studies suggest that anti-VEGF agents may be the first-line therapy for patients with DME [227, 232, 233], the trials demonstrate that no therapy is universally effective. In clinical practice, many eyes that fail anti-VEGF monotherapy demonstrate a better response to laser or intravitreal corticosteroids. Ultimately, the variability in treatment response implies that the DME pathophysiology is multifactorial, and that not all DME is mediated by VEGF.

No consensus exists for determining which patients are more likely to respond to specific therapies. This may be due to the absence of a standard method for patient stratification based on specific disease mechanisms [234, 235]. In recent years, the additional depth-resolved dimension of data provided by SD-OCT imaging has prompted groups to correlate morphological patterns of the retina on OCT with DME and vision outcomes [236–240, 66]. Even so, the majority of the studies require either manual [236, 238–240] or semi-automatic [241] evaluation of the OCT images, as currently only very few automated algorithms exist to quantify morphological or pathological features on images with DME [42, 66, 87, 88, 90–92, 94, 95]. Furthermore, to the best of our knowledge, none of the automated algorithms identify all retinal layers and fluid-filled regions. As such, the development of pathophysiology-specific therapeutic agents for DME has been limited and the selection of specific therapies personalized for individual patients remains subjective. An automated

method capable of stratifying DME patients into subgroups reflecting specific pathophysiological mechanisms would facilitate an optimal choice of personalized therapy for each patient.

As part of our ongoing work, we developed an algorithm to identify fluid-filled regions and seven retinal layers on SD-OCT images of eyes with DME. Two phases were involved in the development of this algorithm: 1) applying the KR-based classification method introduced in Section 8.3 to train classifiers for fluid and retinal layer estimation (Section 9.2), and 2) developing an automated algorithm to classify fluid-filled regions and segment layer boundaries on retinal images with DME (Section 9.3). Validation of our algorithm's performance is an important step within our future work and currently underway. An outline of the algorithm is shown in Figure 9.1, and details are provided in subsequent sections.

9.2 Learning the DME Classifier

We developed a classifier to identify retinal layers and fluid-filled regions on SD-OCT images with DME pathology. This section discusses the steps required to systematically learn the classifier.

9.2.1 Training Dataset

We used the Duke Enterprise Data Unified Content Explorer (DEDUCE) search engine to retrospectively identify patients within the Duke Eye Center Medical Retina practice with a billing code for DME associated with their visit. An ophthalmologist then identified six patients with volumetric macular SD-OCT scans that contained DME and were of adequate image quality. All six scans were acquired using the Spectralis SD-OCT imaging system with the standard 61-line volume scan protocol. Averaging of the B-scans was determined by the photographer. The volumetric scans were 61 B-scans $\times$ 768 A-scans with an axial resolution of 3.87 µm/pixel, and lateral

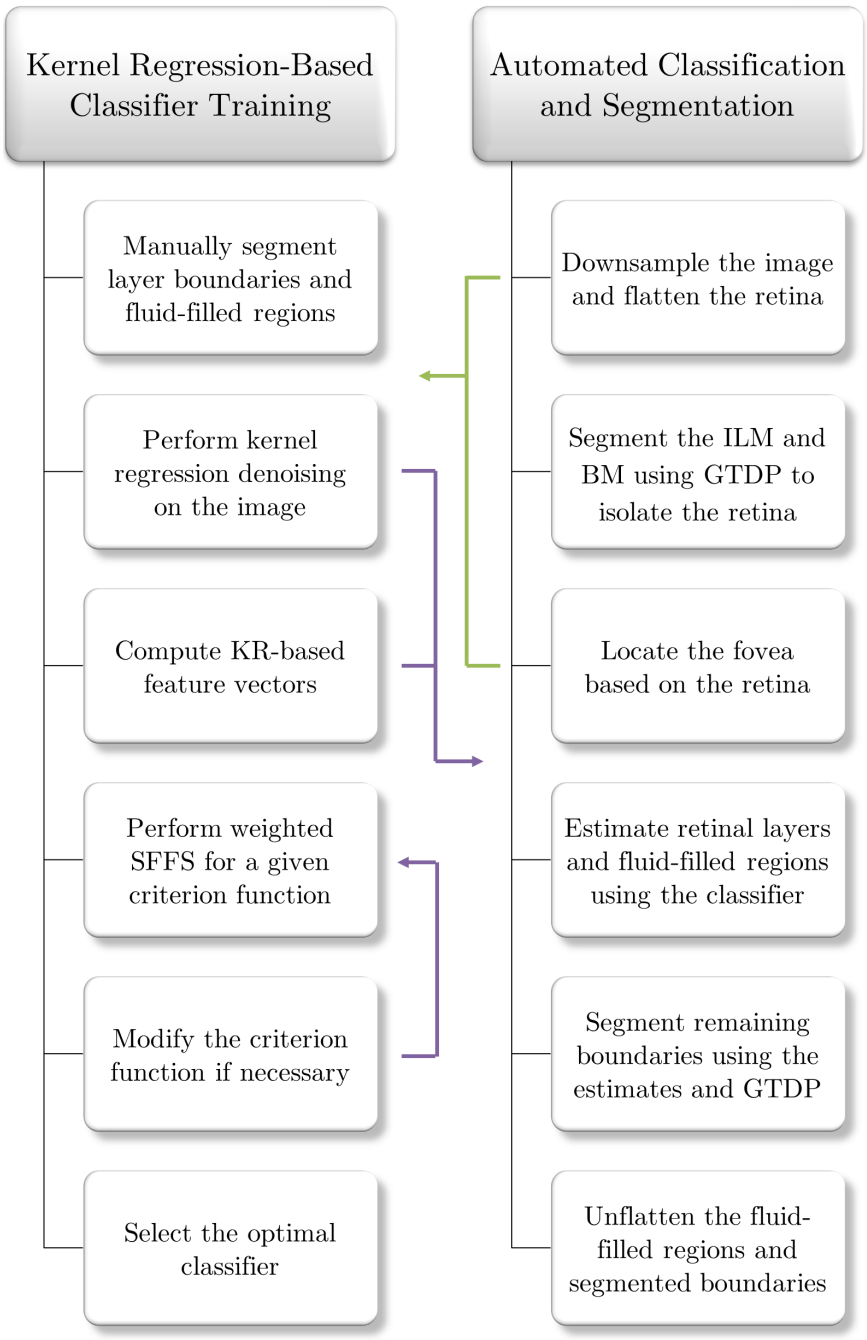

FIGURE 9.1: Flowchart of the KR-based classification and GTDP-based segmentation algorithm for identifying fluid-filled regions and seven retinal layers on images with DME pathology.

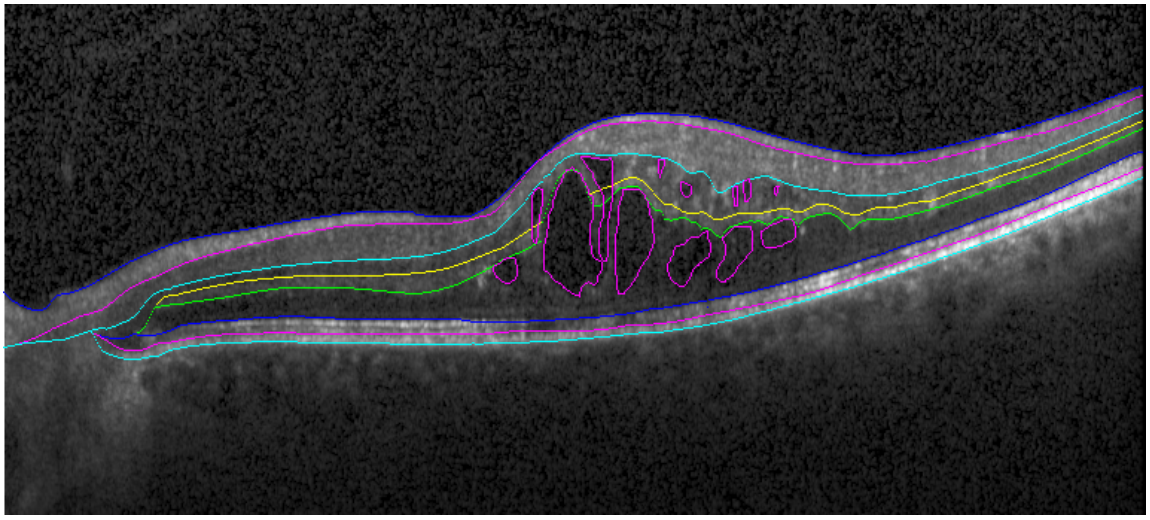

FIGURE 9.2: Manual segmentation of eight retinal layer boundaries (as defined in Figure 1.2) and fluid-filled regions (magenta) on an SD-OCT image of an eye with DME.

and azimuthal resolutions ranging from 11.07 - 11.59 and 118 - 124.6 µm/pixel, respectively.

9.2.2 Manual Segmentation

We manually segmented a total of twelve B-scans (two from each volume) to generate the target classes for classifier training. Within each volume, we selected one image near the fovea (B-scan 31 for all volumes) and one peripheral image. The peripheral images were incrementally spaced to extend out to the peripheral-most scan, where B-scans 26, 21, 16, 11, 6, and 1 were used for the six volumes. A grader manually segmented eight retinal layer boundaries following the definitions in Figure 1.2 and all fluid-filled regions. An example of a manually segmented training image is shown in Figure 9.2.

9.2.3 Kernel Regression-based Denoising

We performed iterative Gaussian steering kernel regression on each training image $\boldsymbol{I}$ as described in Section 8.1 to 1) extract the normalized kernels $\hat{\boldsymbol{K}}_{iGS}$ for every

pixel $\boldsymbol{z}$ in the retina, and 2) recover $\hat{\boldsymbol{b}}$ containing the denoised image and its first and second order gradients (Equations (8.8) and (8.5)). Parameter values included a kernel size of 42.6 × 121.7 µm (11 × 11 pixels, $P = 121$), 3 iterations for $\boldsymbol{K}_{iGS}$, $h_i = 1$, $h_j = 3$, $h = 3$, $\lambda' = 0.1$, and $\lambda'' = 1$. For computational efficiency, we resized the image prior to denoising to a lateral and axial resolution of 13.4 and 6.7 µm per pixel, respectively. We also segmented the ILM, flattened the retina, and located the fovea as described in Sections 9.3.1 and 9.3.2 to replicate the automated classification and segmentation algorithm's image conditions.

Figures 9.3A,F show an example training image and its denoised result. Figures 9.3B,D are zoomed-in images of the pink and green boxes in Figure 9.3A, and Figures 9.3C,E are their respective iterative Gaussian steering kernels. The kernel in Figure 9.3C is wider and more isotropic since its corresponding image patch does not contain strong edges, while the kernel in Figure 9.3E is narrower and is oriented along the image edge. Lastly, Figure 9.3F shows that the regions external to the retina (black) were not denoised with the exception of a padded boundary surrounding the retina; the thickness of this padded boundary is half the kernel size to encapsulate all pixels required for KR-based feature vector computation in Sections 9.2.4 and 9.3.3.

9.2.4 DME Training Features

To train the classifier, we generated feature vectors for all retinal pixels across all training images. Nine of the features were computed using the kernel regression result from Section 9.2.3, four were based on relative spatial positions, and nine were Laws' texture energy features defined in Equation (8.19). All features are listed in Table 9.1 along with their normalization methods. We used adaptive histogram equalization (adapthisteq in MATLAB) to enhance the contrast between feature values while maintaining their order of magnitude, and we used linear normalization for features where the relative magnitude was important (e.g. retinal thickness).

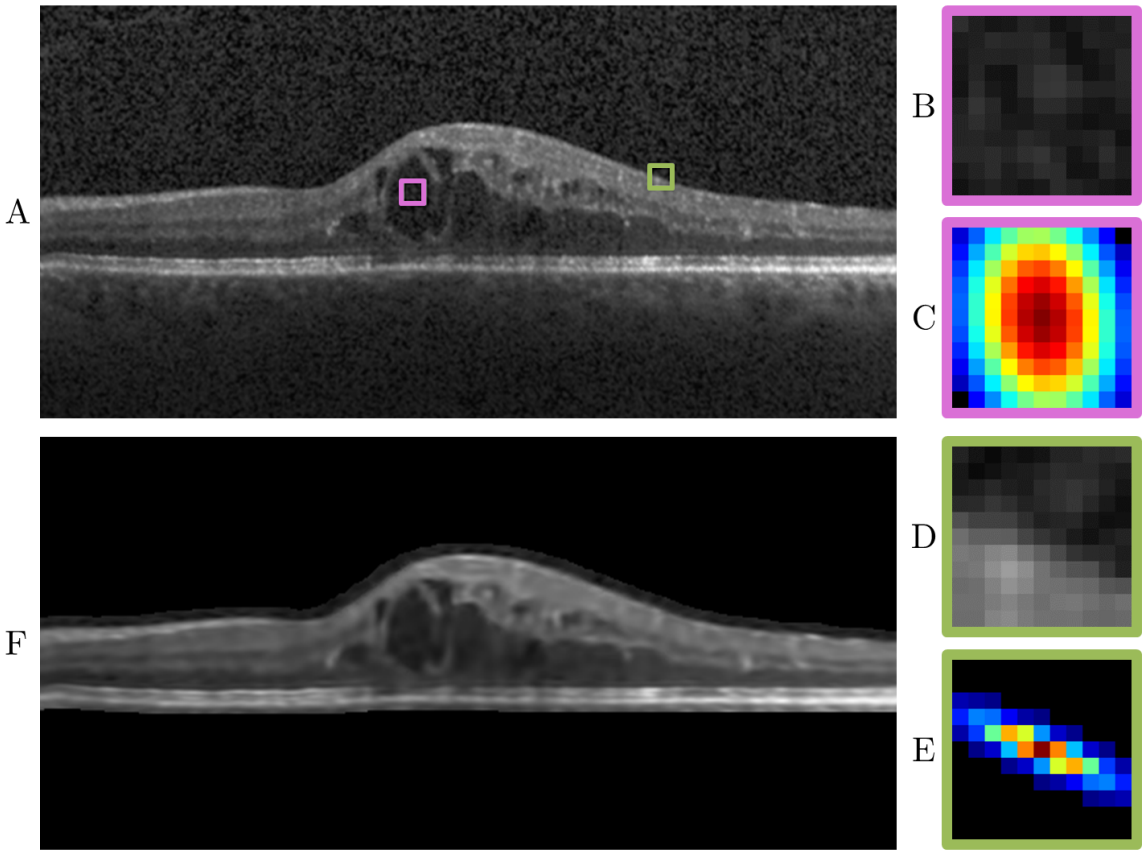

FIGURE 9.3: Second order iterative Gaussian steering kernel regression of an SD-OCT image with DME. (A) Automatically flattened SD-OCT image of an eye with DME, (B,D) zoomed-in images of the pink and green boxes in A, (C,E) Gaussian steering kernels used to denoise the central pixel of B and D, respectively, and (F) the KR-denoised image of A. In F, regions external to the retina (black) were not denoised with the exception of a padded boundary surrounding the retina required for KR-based feature vector computation.

Table 9.1: Twenty two features on SD-OCT images of eyes with DME for classifier training.

Name	**Category**	**Normalization**	**Description**
F01	KR	Adapthisteq	β_0, KR denoised image
F02	KR	Adapthisteq	$\boldsymbol{\beta}_1[1]$, KR denoised vertical gradient
F03	KR	Adapthisteq	$\boldsymbol{\beta}_1[2]$, KR denoised horizontal gradient
F04	KR	Adapthisteq	$\boldsymbol{\beta}_2[1]$, KR denoised vertical 2^{nd} derivative
F05	KR	Adapthisteq	$\boldsymbol{\beta}_2[2]$, KR denoised diagonal 2^{nd} derivative
F06	KR	Adapthisteq	$\boldsymbol{\beta}_2[3]$, KR denoised horizontal 2^{nd} derivative
F07	KR	Linear	Kernel FWHM along the j axis
F08	KR	Linear	Kernel FWHM along the i axis
F09	KR	Linear	Kernel area
F10	Position	Linear	Horizontal temporal-to-nasal position
F11	Position	Linear	Vertical position within the retina
F12	Position	Linear	Radial ij distance from the fovea
F13	Position	Linear	Retinal thickness
F14	Laws	Adapthisteq	$\boldsymbol{F}_{L1}$, Laws' L5E5/E5L5 filter
F15	Laws	Adapthisteq	$\boldsymbol{F}_{L2}$, Laws' L5S5/S5L5 filter
F16	Laws	Adapthisteq	$\boldsymbol{F}_{L3}$, Laws' L5R5/R5L5 filter
F17	Laws	Adapthisteq	$\boldsymbol{F}_{L4}$, Laws' E5E5 filter
F18	Laws	Adapthisteq	$\boldsymbol{F}_{L5}$, Laws' E5S5/S5E5 filter
F19	Laws	Adapthisteq	$\boldsymbol{F}_{L6}$, Laws' E5R5/R5E5 filter
F20	Laws	Adapthisteq	$\boldsymbol{F}_{L7}$, Laws' S5S5 filter
F21	Laws	Adapthisteq	$\boldsymbol{F}_{L8}$, Laws' S5R5/R5S5 filter
F22	Laws	Adapthisteq	$\boldsymbol{F}_{L9}$, Laws' R5R5 filter

Table 9.2: DME classes used to train the fluid+layer classifier.

Identifier	Class	Color
C1	Fluid	
C2	NFL	
C3	GCL-IPL	
C4	INL	
C5	OPL	
C6	ONL	
C7	ISE-OS	
C8	RPE	

9.2.5 DME Training Classes

We defined a set of classes for our fluid+layer classifier. These classes are listed in Table 9.2. Using the manual segmentation from Section 9.2.2 as a guideline, we then derived the true classes for each training image.

9.2.6 Simultaneous Feature and Weight Selection

We next used the weighted SFFS method proposed in Step 4 of Section 8.3 to select the features and weights most appropriate for fluid and layer classification. We applied the ten-fold cross-validation method [212] during feature selection and adjusted parameters for the criterion function until we achieved a desired classification result. Descriptions of our criterion function parameters are as follows:

- *Maximum Iterations*: The maximum number of weighted features that can be added to the set $\boldsymbol{v}'$. Fewer iterations may lead to inaccurate classifications, while too many iterations may result in overfitting.

- *Required Features*: A set of features that must be selected when using SFFS. In cases where the SFFS method converges to an undesirable local minimum, we can force features to be included within the selected set. Thus, rather than starting $\boldsymbol{v}'$ as a null set, we include these features from the onset of SFFS.

- *Possible Weights*: The set of possible weight values, $\boldsymbol{a}$, for the features. While more weight values or finer weight increments may lead to better results, this increases the computational complexity for classifier training.

- *Classes*: The set of possible classes, $\boldsymbol{C}$, for a given classifier. We may add or remove classes to achieve the desired results. For example, removing the *fluid* class allows for the detection of continuous layers. In other cases where only

a single class is of interest, it may be beneficial to add other classes to $\boldsymbol{C}$ in order to prevent false positive classifications.

- *Criterion Classes*: The set of classes $\boldsymbol{C}' \subseteq \boldsymbol{C}$ to be evaluated using the criterion function. This may be desired when certain classes take precedence over others.

- *Classifier Function*: We considered the nearest neighbor classifier function with two possible classifier functions: the *minimum weighted distance function* from Equation (8.27), and the *minimum weighted negative Gaussian function* defined by

$$\hat{c} = \phi(\boldsymbol{v}) = \left\{ C_k \in \boldsymbol{C} \mid \underset{k}{\operatorname{argmin}} \left[1 - \exp\left(-\frac{1}{2} \left[\boldsymbol{\sigma}_k^{inv} \circ \boldsymbol{\omega} \circ (\boldsymbol{v} - \boldsymbol{\mu}_k) \right] \right. \right. \right.$$
$$\left. \left. \left. \left[\boldsymbol{\sigma}_k^{inv} \circ \boldsymbol{\omega} \circ (\boldsymbol{v} - \boldsymbol{\mu}_k) \right]^T \right) \right]^{\frac{1}{2}} \right\}, \quad (9.1)$$

  where $\boldsymbol{\sigma}_k^{inv} \in \mathbb{R}^{1 \times L'}$ is the reciprocal of the standard deviation of the training feature vectors for class C_k and is defined by

$$\boldsymbol{\sigma}_k^{inv}[l] = \left(\frac{1}{T_k - 1} \sum_{t=1}^{T_k} \left(\boldsymbol{V}_k[t, l] - \boldsymbol{\mu}_k[l] \right)^2 \right)^{-\frac{1}{2}}, \quad l = 1 \ldots L. \quad (9.2)$$

- *Criterion Expression*: The function $E(\cdot)$ used to evaluate classification error. We based our criterion functions on various combinations of the number of true positives (N_{TP}), false positives (N_{FP}), true negatives (N_{TN}), false negatives (N_{FN}), as well as the sensitivity and specificity [242] of a given class. Only the classes specified in *Criterion Classes* were used in the criterion function to calculate error.

The criterion function parameters used to generate the optimal classifier are listed in Table 9.3. As shown in Table 9.3, we added an additional fluid and NFL classifier

Table 9.3: Parameters of the criterion function used in the weighted sequential forward feature selection method to generate the fluid + retinal layer classifier.

Parameter	**Classifier**		
	Fluid+Layers	Fluid	NFL
Maximum iterations	10	10	20
Required features	none	F01	F10
Criterion classes	C1-C5	C1	C2
Classifier function	Gaussian	Distance	Distance
Possible weights	0, 0.1, 0.2, . . . , 1		
Classes	C1-C8		
Criterion expression	$\left(1 - \frac{\text{sensitivity} + \text{specificity}}{2}\right)$		

to improve the fluid classification and NFL/GCL segmentation, respectively. The results for these additional classifiers were integrated into the fluid+layer classifier in that any pixels categorized as the "NFL" by the NFL classifier took precedence over the class determined by the fluid+layer classifier. Additionally, any clusters classified as "fluid" by the fluid classifier that partially overlapped with fluid clusters identified by the fluid+layer classifier also overrode the fluid+layer classification.

9.2.7 DME Training Classifier Results

The selected features and weights for the classifiers in Table 9.3 are shown in Figure 9.4 and listed in Table 9.4. Figure 9.5 shows an example training image with the manual (true) class assignments (Figure 9.5B), and the automatic class assignments generated by the fluid+layer, fluid, and NFL classifiers integrated together (Figure 9.5C). Note that in Figure 9.5C, the outer retinal layers were not optimized for accuracy since the intraretinal layers took precedence in terms of generating accurate classification estimates.

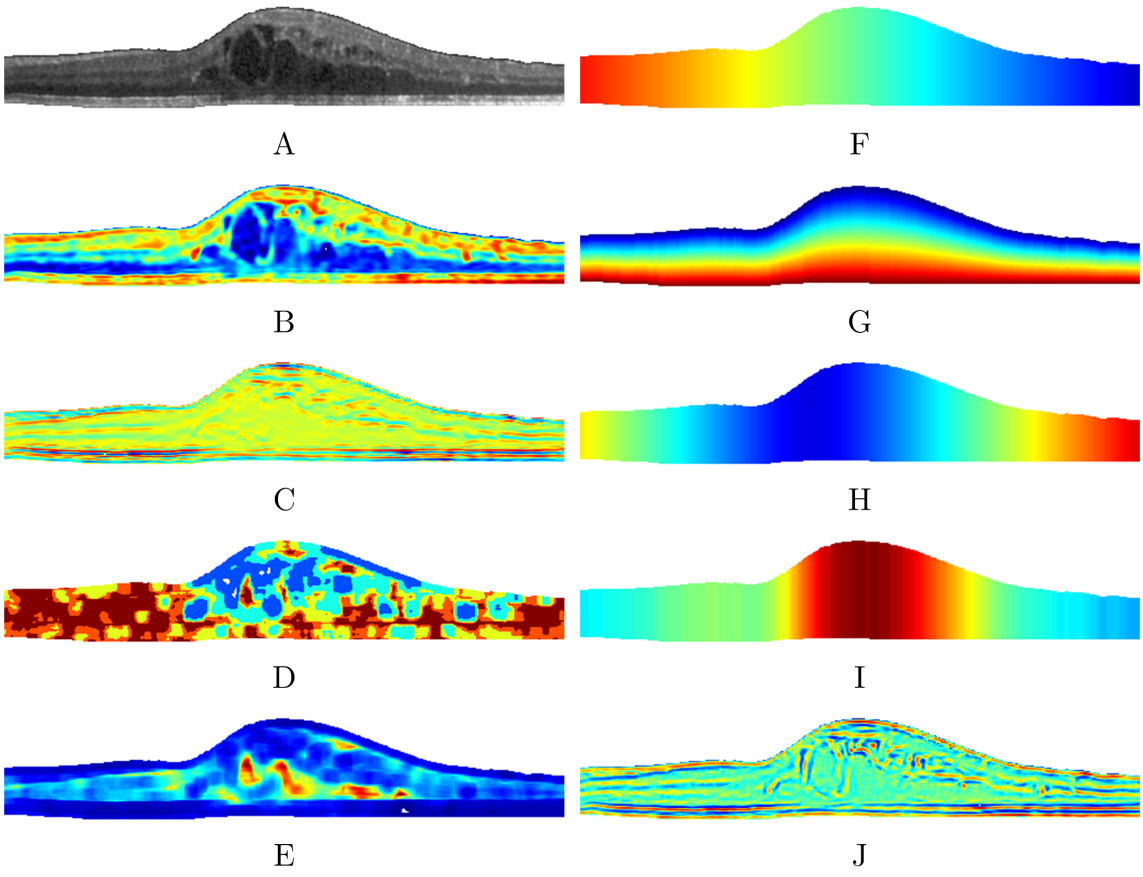

FIGURE 9.4: Visual example of the DME features selected for the fluid+layer classifier. (A) An example flattened SD-OCT training image of the retina region only, and (B-J) features for A corresponding to F01, F04, F07, F09, F10, F11, F12, F13, and F15 in Table 9.1, respectively.

9.3 Automatic Classification-Based GTDP Segmentation Algorithm

We next leveraged the classification results in Section 9.2 to create a fully automatic GTDP segmentation algorithm for identifying fluid-filled regions and seven retinal layers on SD-OCT images with DME. An outline of the algorithm is shown in Figure 9.1 (right) and explained in detail in the following subsections.

Table 9.4: Selected features and weights for the DME classifiers. The features are listed in the order that they were selected.

Fluid+Layer		Fluid		NFL	
Feature	Weight	Feature	Weight		
F11	1.6	F01	1.0	F11	1.1
F13	0.8	F13	0.3	F12	0.6
F01	0.8	F11	0.4	F10	0.6
F15	0.6	F12	0.1	F15	0.4
F10	0.4	F19	0.7	F07	0.3
F12	0.4	F10	0.3	F01	0.2
F09	0.4	F14	0.2	F09	0.3
F07	0.3	F16	0.8	F06	0.2
F04	0.6	F06	0.2	F05	0.3
		F21	0.3	F19	0.1
		F17	0.1	F22	0.1

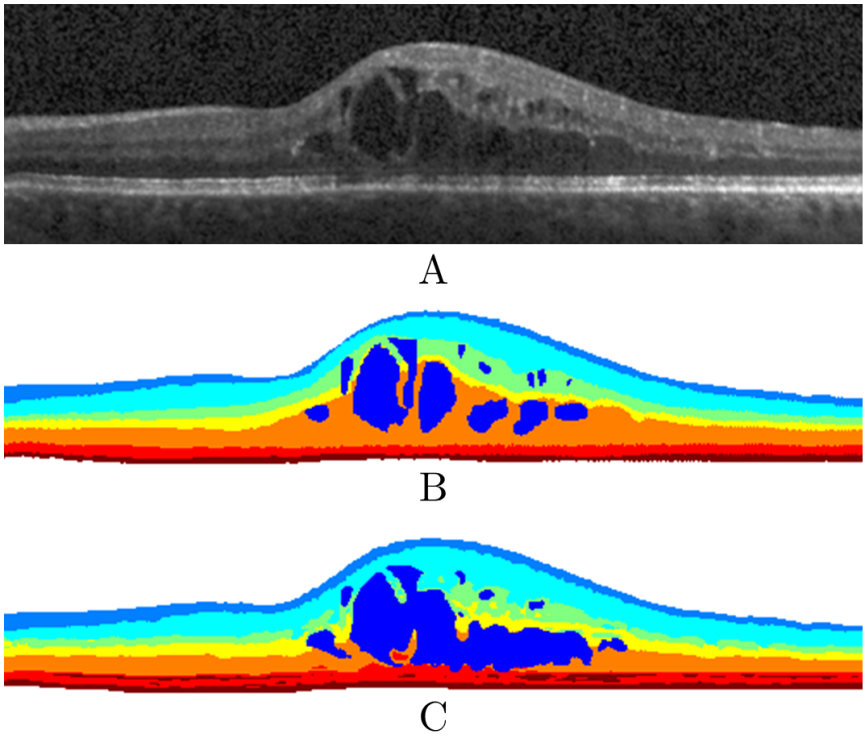

FIGURE 9.5: Example KR-based classification. (A) An example flattened SD-OCT training image with DME, (B) manual classification results, and (C) automatic classification results using the fluid+layer, fluid, and NFL classifiers integrated together.

9.3.1 Flattening and GTDP Segmentation of the Retina

In order to flatten the retina, we first use our previously validated segmentation algorithm described in Chapter 7 to generate pilot estimates of BM. This is achieved by extracting the NFL-OPL and ISE-RPE hyper-reflective complexes as described in Section 5.3.2 and assigning the lower boundary of the ISE-RPE complex as BM. As in Chapter 7 and Section 9.2.3, we downsample the images to an axial and lateral resolution of 6.7 and 13.4 µm/pixel, respectively.

After obtaining BM estimates across all B-scans, we perform linear interpolation across B-scans to estimate any missing BM boundaries, and we extrapolate any missing A-scans within each B-scan. Next, we remove any outliers by computing the BM difference across B-scans and finding errors greater than three standard deviations above the mean. Values within these regions are replaced with linearly interpolated values. The 2D layer boundary map of BM is filtered using a Gaussian mask 0.5×0.5 mm in size with a standard deviation of 0.25 mm. Columns in each image are then vertically shifted until the pilot estimate of BM is completely flattened. Finally, we use the validated GTDP segmentation algorithm from Chapter 7 to segment the ILM, OS/RPE, and BM boundaries.

9.3.2 Locating the Fovea

Identifying the location of the fovea on a volumetric macular scan allows us to gauge the location of the optic nerve and merged retinal layers. Upon segmenting the ILM and BM on all B-scans, we locate the fovea based on the calculated TRT. To do this, we first Gaussian filter the TRT using a window of 120 × 61.2 µm and standard deviation of 83.5 × 15.7 µm. We then narrow our search region to the central 3 mm of the volumetric macular scan and find all local minima with a depth greater than 7.74 µm. If the local minimum with the lowest TRT also resides closest to center of the volume, then we assign that location as the fovea. Otherwise, we create a

summed voxel projection (SVP) by summing pixels ranging from the ILM to 19.35 µm below the ILM across all B-scans. As with the TRT, we smooth the SVP, locate minima, and compute distances from the fovea. Looking at the five minima closest to the center of the volume, we set the local minimum with the lowest intensity as the fovea.

9.3.3 Classification of Fluid and Retinal Layers

To classify the images, we perform the second order iterative Gaussian kernel regression method following Section 9.2.3. We then compute the features listed in Table 9.1. Finally, we classify the feature vectors using the weighted negative Gaussian function from Equation (9.1) for the fluid+layer classifier, and the weighted distance function from Equation (8.27) for the fluid and NFL classifiers. All resulting "NFL" classes determined by the NFL classifier then supersede the fluid+layer classifier results. Furthermore, any "fluid" clusters found by the fluid classifier that overlap with fluid determined by the fluid+layer classifier are added to the classified result.

9.3.4 GTDP Segmentation of Intraretinal Layers

We use the fluid and retinal classification estimates to segment the retinal layer boundaries using our GTDP framework. Rather than limiting the search region using these estimates, we instead modify the graph weights to reflect the classification result. This is done by generating a layer boundary image based on two adjacent layers. For example, we create the NFL/GCL boundary image by taking the gradient of an image containing the NFL and GCL-IPL classification results. This extracts the boundary between the two layers, which we then dilate using a disk with a radius 7.74

$\times$ 13.4 µm in size. To segment the NFL/GCL, we calculate graph weights following

$$\begin{aligned}\omega_{ab} =& \text{LinNorm}(-g_a^{LD} - g_b^{LD},\ 0,\ 1) + \\ & \text{LinNorm}(-i_a - i_b,\ 0,\ 0.5) + \\ & \text{LinNorm}(-c_a^{23} - c_b^{23},\ 0,\ 0.5)\ +\ \omega_{min},\end{aligned} \tag{9.3}$$

where c_n^{23} is the value at node n of the boundary image generated for classes C2 and C3 (the NFL and GCL-IPL). The search region is then limited to the region between the ILM and ISM/ISE boundaries, with the exception of A-scans within 1 mm of the foveal region. For these A-scans, the bottom boundary is limited to 23.22 µm below the top boundary.

For the OPL/ONL, INL/OPL, and IPL/INL layer boundaries, weights are calculated following Equations 9.4 - 9.6, respectively. Search regions are then limited by the NFL/GCL and ISM/ISE to segment the OPL/ONL, from 7.74 µm below the NFL/GCL to the OPL/ONL to segment the INL/OPL, and from half the distance between the NFL/GCL and INL/OPL to the INL/OPL to segment the IPL/INL boundary.

$$\begin{aligned}\omega_{ab} =& \text{LinNorm}(-g_a^{LD} - g_b^{LD},\ 0,\ 1) + \\ & \text{LinNorm}(-c_a^{56} - c_b^{56},\ 0,\ 0.5)\ +\ \omega_{min},\end{aligned} \tag{9.4}$$

$$\begin{aligned}\omega_{ab} =& \text{LinNorm}(-g_a^{DL} - g_b^{DL},\ 0,\ 1) + \\ & \text{LinNorm}(d_{ab},\ 0,\ 0.1) + \\ & \text{LinNorm}(-c_a^{45} - c_b^{45},\ 0,\ 0.5)\ +\ \omega_{min},\end{aligned} \tag{9.5}$$

$$\begin{aligned}\omega_{ab} =& \text{LinNorm}(-g_a^{LD} - g_b^{LD},\ 0,\ 1) + \\ & \text{LinNorm}(d_{ab},\ 0,\ 0.1) + \\ & \text{LinNorm}(-c_a^{34} - c_b^{34},\ 0,\ 0.5)\ +\ \omega_{min},\end{aligned} \tag{9.6}$$

While search region limitation is still an integral step within the algorithm, ad hoc rules are significantly reduced with the addition of the classification weights. Finally, after the segmentation is complete, we unflatten the fluid and layer boundaries to map them back onto the original image.

9.4 Results

Figure 9.6 shows qualitative results of our fully automatic segmentation algorithm for DME pathology. These images were not part of the training dataset and were thus not used to tune algorithm parameters. Figures 9.6A,C,E show images with significant fluid buildup, moderate amounts of fluid, and no fluid, respectively, and Figures 9.6B,D,F are their corresponding segmentation results.

9.5 Summary

We implemented a fully automatic algorithm to classify fluid-filled regions and segment retinal layer boundaries on SD-OCT images with DME pathology. This was accomplished by jointly using the KR-based classification and GTDP segmentation frameworks. The qualitative results are encouraging, and validation of this algorithm is part of our ongoing work. Accurate identification of fluid and retinal layer boundaries on SD-OCT images containing DME pathology is extremely important, as it facilitates the stratification of patients based on disease mechanisms. This will ultimately enable physicians to provide personalized therapies to patients for improved vision outcomes.

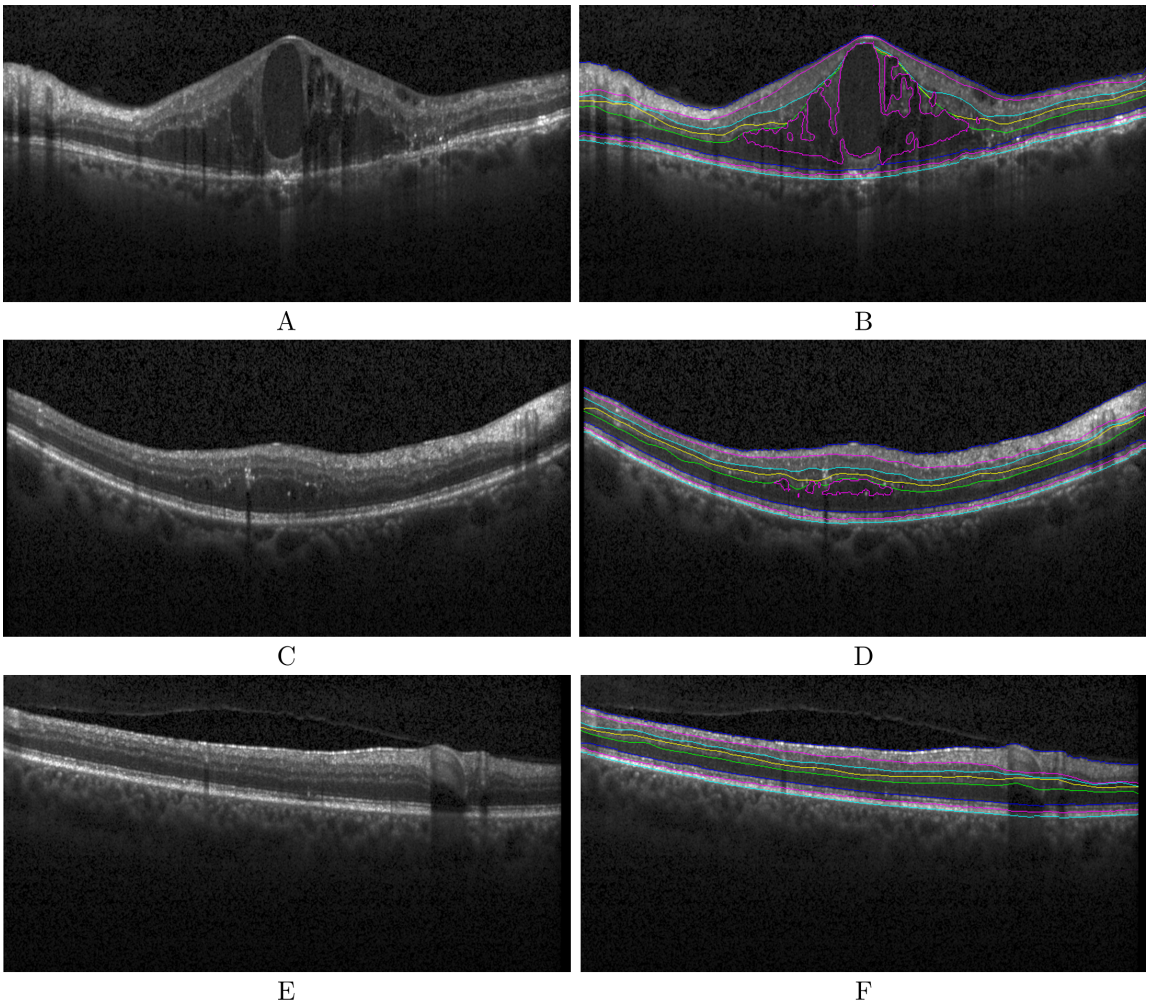

FIGURE 9.6: Qualitative results for the classification of fluid and the segmentation of eight SD-OCT retinal layer boundaries on SD-OCT images of eyes with DME. (A) An image with significant fluid buildup, and (B) its segmentation result. (C) An image with a small amount of fluid, and (D) its segmentation result. (E) An image with no visible DME pathology, and (F) its segmentation result.

10

DOCTRAP Software

We developed a MATLAB-based software called *Duke's Optical Coherence Tomography Retinal Analysis Program* (DOCTRAP) to facilitate automatic and semi-automatic GTDP segmentation for quantitative ophthalmic research (Figure 10.1). Features of the DOCTRAP software include:

- Automatic segmentation of retinal layers and fluid-filled regions on SD-OCT images (Figure 10.2), photoreceptors on AOSLO images, and RPE cells on confocal microscopy images with parallel processing capabilities.
- Manual segmentation and/or correction of layer boundaries, closed-contours, and foci with customizable marking options.
- Automatically generated and customizable SVP and layer thickness maps with export options.
- Tools for quantitative analysis and image review, including measurement rulers, automatic and/or manual specification of image dimensions, marking of the fovea, region-of-interest display, and a comments box.

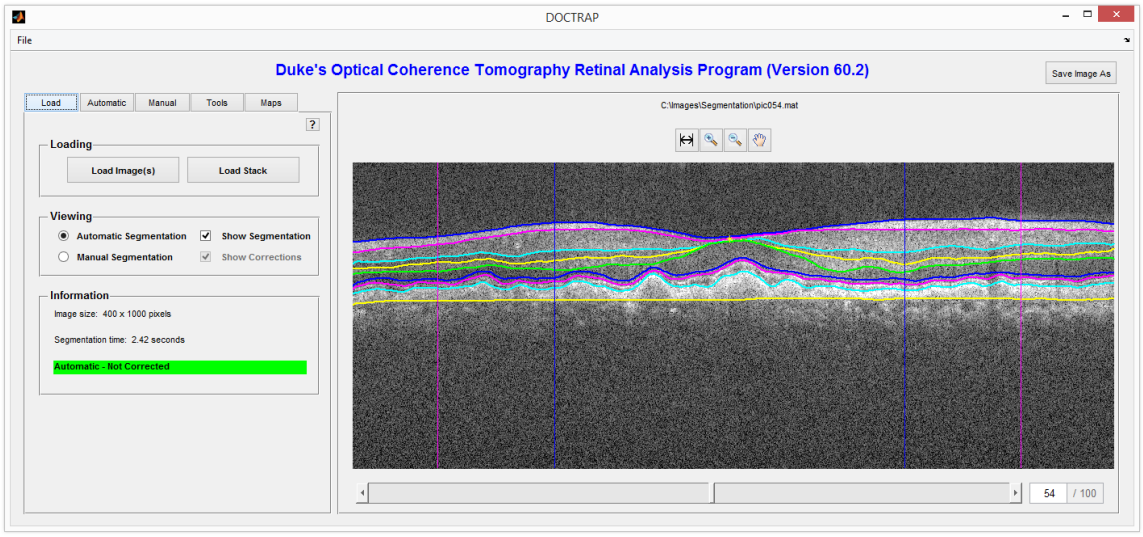

FIGURE 10.1: Screenshot of Duke's Optical Coherence Tomography Retinal Analysis Program (DOCTRAP) for automatic and semi-automatic segmentation using the GTDP algorithm.

Using our DOCTRAP software, we were able to apply our GTDP segmentation algorithms to a variety of clinical applications, including:

- study of the dynamics of human foveal development after premature birth [243],
- macular findings for healthy full-term newborns observed by handheld SD-OCT [244, 245],
- assessment of cystoid macular edema in retinopathy of prematurity [246],
- assessment of the differences in choroidal thickness and choroid visualization using inverted versus upright SD-OCT [247],
- study of the maturation of the human fovea and correlation of retinal layers on SD-OCT with findings in histology [248],
- quantify changes in intraretinal hyper-reflective foci distribution and its correlation with AMD disease progression [249],

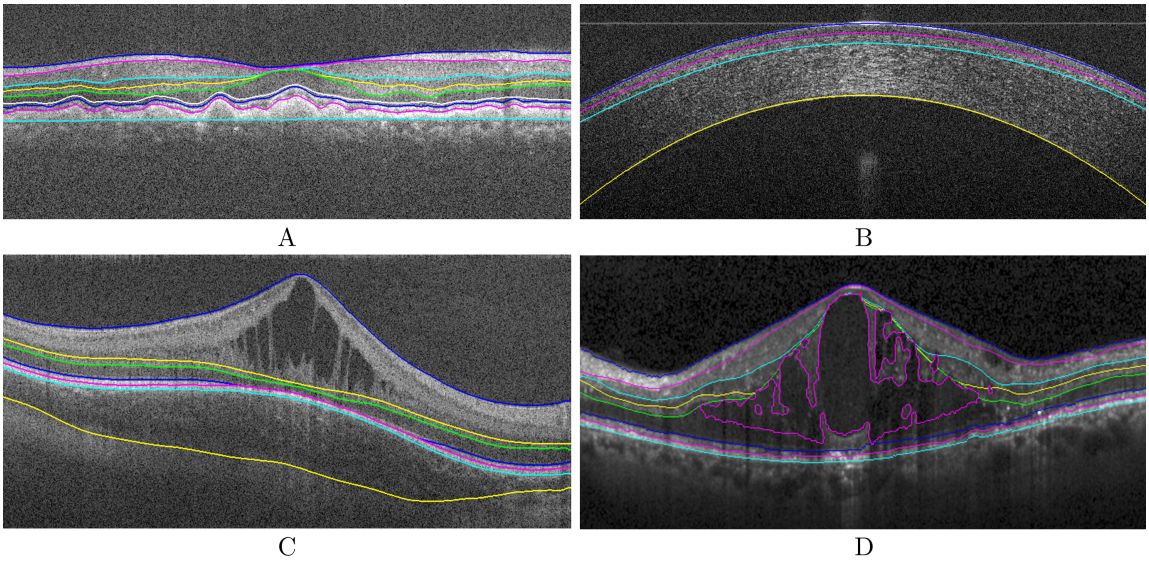

FIGURE 10.2: DOCTRAP segmentation of anatomical and pathological SD-OCT images of the eye. (A) Nine retinal layer boundaries segmented for an eye with non-neovascular AMD (white line is the external limiting membrane), (B) Four corneal layer boundaries segmented, (C) seven layer boundaries segmented for a pediatric eye with edema (bottom yellow line is the CSJ), noting the ISE layer which is not yet fully developed, and (D) eight retinal layer boundaries and fluid-filled regions (magenta) segmented for an eye with DME.

- speckle variance imaging of distinct retinal capillary beds [250],
- study of choroid development in preterm and term infants using SD-OCT [251],
- correction of ocular shape in retinal OCT and study of its effect on current clinical measures [252],
- creation of quantitative OCT biomarkers for the classification of eyes with and without intermediate AMD [253], and
- characterization of the choroid-scleral junction (CSJ) and suprachoroidal layer using enhanced-depth imaging OCT [254].

References

[1] S.L. Polyak. *The Retina: The Anatomy and the Histology of the Retina in Man, Ape and Monkey, Including the Consideration of Visual Functions, the History of Physiological Optics, and the Histological Laboratory Technique*. University of Chicago Press, 1941.

[2] C. A. Puliafito, M. R. Hee, C. P. Lin, E. Reichel, J. S. Schuman, J. S. Duker, J. A. Izatt, E. A. Swanson, and J. G. Fujimoto. Imaging of macular diseases with optical coherence tomography. *Ophthalmology*, 102(2):217–229, Feb 1995.

[3] N. M. Bressler. Early detection and treatment of neovascular age-related macular degeneration. *J Am Board Fam Pract*, 15(2):142–152, 2002.

[4] L. A. Yannuzzi, M. D. Ober, J. S. Slakter, R. F. Spaide, Y. L. Fisher, R. W. Flower, and R. Rosen. Ophthalmic fundus imaging: today and beyond. *Am. J. Ophthalmol.*, 137(3):511–524, Mar 2004.

[5] D. Huang, E. A. Swanson, C. P. Lin, J. S. Schuman, W. G. Stinson, W. Chang, M. R. Hee, T. Flotte, K. Gregory, and C. A. Puliafito. Optical coherence tomography. *Science*, 254(5035):1178–1181, Nov 1991.

[6] R. Leitgeb, C. Hitzenberger, and A. Fercher. Performance of fourier domain vs. time domain optical coherence tomography. *Opt Express*, 11(8):889–894, Apr 2003.

[7] M. Choma, M. Sarunic, C. Yang, and J. Izatt. Sensitivity advantage of swept source and Fourier domain optical coherence tomography. *Opt Express*, 11 (18):2183–2189, Sep 2003.

[8] M. R. Hee, C. A. Puliafito, J. S. Duker, E. Reichel, J. G. Coker, J. R. Wilkins, J. S. Schuman, E. A. Swanson, and J. G. Fujimoto. Topography of diabetic macular edema with optical coherence tomography. *Ophthalmology*, 105(2): 360–370, Feb 1998.

[9] T. Otani, S. Kishi, and Y. Maruyama. Patterns of diabetic macular edema with optical coherence tomography. *Am. J. Ophthalmol.*, 127(6):688–693, Jun 1999.

[10] J. D. Ding, L. V. Johnson, R. Herrmann, S. Farsiu, S. G. Smith, M. Groelle, B. E. Mace, P. Sullivan, J. A. Jamison, U. Kelly, O. Harrabi, S. S. Bollini, J. Dilley, D. Kobayashi, B. Kuang, W. Li, J. Pons, J. C. Lin, and C. Bowes Rickman. Anti-amyloid therapy protects against retinal pigmented epithelium damage and vision loss in a model of age-related macular degeneration. *Proc Natl Acad Sci U.S.A.*, 108(28):E279–287, Jul 2011.

[11] J. Liang, D. R. Williams, and D. T. Miller. Supernormal vision and high-resolution retinal imaging through adaptive optics. *J Opt Soc Am A Opt Image Sci Vis*, 14(11):2884–2892, Nov 1997.

[12] H. Hofer, L. Chen, G. Y. Yoon, B. Singer, Y. Yamauchi, and D. R. Williams. Improvement in retinal image quality with dynamic correction of the eye's aberrations. *Opt Express*, 8(11):631–643, May 2001.

[13] A. Roorda, F. Romero-Borja, W. Donnelly Iii, H. Queener, T. Hebert, and M. Campbell. Adaptive optics scanning laser ophthalmoscopy. *Opt Express*, 10(9):405–412, May 2002.

[14] Y. Zhang, J. Rha, R. Jonnal, and D. Miller. Adaptive optics parallel spectral domain optical coherence tomography for imaging the living retina. *Opt Express*, 13(12):4792–4811, Jun 2005.

[15] R. J. Zawadzki, S. M. Jones, S. S. Olivier, M. Zhao, B. A. Bower, J. A. Izatt, S. Choi, S. Laut, and J. S. Werner. Adaptive-optics optical coherence tomography for high-resolution and high-speed 3D retinal in vivo imaging. *Opt Express*, 13(21):8532–8546, Oct 2005.

[16] D. Merino, C. Dainty, A. Bradu, and A. G. Podoleanu. Adaptive optics enhanced simultaneous en-face optical coherence tomography and scanning laser ophthalmoscopy. *Opt Express*, 14(8):3345–3353, Apr 2006.

[17] Y. Zhang, B. Cense, J. Rha, R. S. Jonnal, W. Gao, R. J. Zawadzki, J. S. Werner, S. Jones, S. Olivier, and D. T. Miller. High-speed volumetric imaging of cone photoreceptors with adaptive optics spectral-domain optical coherence tomography. *Opt Express*, 14(10):4380–4394, May 2006.

[18] S. A. Burns, R. Tumbar, A. E. Elsner, D. Ferguson, and D. X. Hammer. Large-field-of-view, modular, stabilized, adaptive-optics-based scanning laser ophthalmoscope. *J Opt Soc Am A Opt Image Sci Vis*, 24(5):1313–1326, May 2007.

[19] M. Pircher, R. J. Zawadzki, J. W. Evans, J. S. Werner, and C. K. Hitzenberger. Simultaneous imaging of human cone mosaic with adaptive optics enhanced scanning laser ophthalmoscopy and high-speed transversal scanning optical coherence tomography. *Opt Lett*, 33(1):22–24, Jan 2008.

[20] M. Mujat, R. D. Ferguson, N. Iftimia, and D. X. Hammer. Compact adaptive optics line scanning ophthalmoscope. *Opt Express*, 17(12):10242–10258, Jun 2009.

[21] C. Torti, B. Povazay, B. Hofer, A. Unterhuber, J. Carroll, P. K. Ahnelt, and W. Drexler. Adaptive optics optical coherence tomography at 120,000 depth scans/s for non-invasive cellular phenotyping of the living human retina. *Opt Express*, 17(22):19382–19400, Oct 2009.

[22] M. Mujat, R. D. Ferguson, A. H. Patel, N. Iftimia, N. Lue, and D. X. Hammer. High resolution multimodal clinical ophthalmic imaging system. *Opt Express*, 18(11):11607–11621, May 2010.

[23] R. D. Ferguson, Z. Zhong, D. X. Hammer, M. Mujat, A. H. Patel, C. Deng, W. Zou, and S. A. Burns. Adaptive optics scanning laser ophthalmoscope with integrated wide-field retinal imaging and tracking. *J Opt Soc Am A Opt Image Sci Vis*, 27(11):A265–277, Nov 2010.

[24] A. Dubra and Y. Sulai. Reflective afocal broadband adaptive optics scanning ophthalmoscope. *Biomed Opt Express*, 2(6):1757–1768, Jun 2011.

[25] R. S. Jonnal, O. P. Kocaoglu, Q. Wang, S. Lee, and D. T. Miller. Phase-sensitive imaging of the outer retina using optical coherence tomography and adaptive optics. *Biomed Opt Express*, 3(1):104–124, Jan 2012.

[26] J. Carroll, M. Neitz, H. Hofer, J. Neitz, and D. R. Williams. Functional photoreceptor loss revealed with adaptive optics: an alternate cause of color blindness. *Proc Natl Acad Sci U.S.A.*, 101(22):8461–8466, Jun 2004.

[27] S. S. Choi, N. Doble, J. L. Hardy, S. M. Jones, J. L. Keltner, S. S. Olivier, and J. S. Werner. In vivo imaging of the photoreceptor mosaic in retinal dystrophies and correlations with visual function. *Invest Ophthalmol Vis Sci*, 47(5):2080–2092, May 2006.

[28] J. I. Wolfing, M. Chung, J. Carroll, A. Roorda, and D. R. Williams. High-resolution retinal imaging of cone-rod dystrophy. *Ophthalmology*, 113(6): 1019.e1, Jun 2006.

[29] R. C. Baraas, J. Carroll, K. L. Gunther, M. Chung, D. R. Williams, D. H. Foster, and M. Neitz. Adaptive optics retinal imaging reveals S-cone dystrophy in tritan color-vision deficiency. *J Opt Soc Am A Opt Image Sci Vis*, 24(5): 1438–1447, May 2007.

[30] J. L. Duncan, Y. Zhang, J. Gandhi, C. Nakanishi, M. Othman, K. E. Branham, A. Swaroop, and A. Roorda. High-resolution imaging with adaptive optics in patients with inherited retinal degeneration. *Invest Ophthalmol Vis Sci*, 48(7): 3283–3291, Jul 2007.

[31] S. S. Choi, R. J. Zawadzki, M. A. Greiner, J. S. Werner, and J. L. Keltner. Fourier-domain optical coherence tomography and adaptive optics reveal nerve fiber layer loss and photoreceptor changes in a patient with optic nerve drusen. *J Neuroophthalmol*, 28(2):120–125, Jun 2008.

[32] J. Carroll, S. S. Choi, and D. R. Williams. In vivo imaging of the photoreceptor mosaic of a rod monochromat. *Vision Res*, 48(26):2564–2568, Nov 2008.

[33] M. K. Yoon, A. Roorda, Y. Zhang, C. Nakanishi, L. J. Wong, Q. Zhang, L. Gillum, A. Green, and J. L. Duncan. Adaptive optics scanning laser ophthalmoscopy images in a family with the mitochondrial DNA T8993C mutation. *Invest Ophthalmol Vis Sci*, 50(4):1838–1847, Apr 2009.

[34] J. Carroll, R. C. Baraas, M. Wagner-Schuman, J. Rha, C. A. Siebe, C. Sloan, D. M. Tait, S. Thompson, J. I. Morgan, J. Neitz, D. R. Williams, D. H. Foster, and M. Neitz. Cone photoreceptor mosaic disruption associated with Cys203Arg mutation in the M-cone opsin. *Proc Natl Acad Sci U.S.A.*, 106 (49):20948–20953, Dec 2009.

[35] S. Ooto, M. Hangai, A. Sakamoto, A. Tsujikawa, K. Yamashiro, Y. Ojima, Y. Yamada, H. Mukai, S. Oshima, T. Inoue, and N. Yoshimura. High-resolution imaging of resolved central serous chorioretinopathy using adaptive optics scanning laser ophthalmoscopy. *Ophthalmology*, 117(9):1800–1809, Sep 2010.

[36] S. Ooto, M. Hangai, K. Takayama, A. Sakamoto, A. Tsujikawa, S. Oshima, T. Inoue, and N. Yoshimura. High-resolution imaging of the photoreceptor layer in epiretinal membrane using adaptive optics scanning laser ophthalmoscopy. *Ophthalmology*, 118(5):873–881, May 2011.

[37] S. Ooto, M. Hangai, K. Takayama, N. Arakawa, A. Tsujikawa, H. Koizumi, S. Oshima, and N. Yoshimura. High-resolution photoreceptor imaging in idiopathic macular telangiectasia type 2 using adaptive optics scanning laser ophthalmoscopy. *Invest Ophthalmol Vis Sci*, 52(8):5541–5550, Jul 2011.

[38] D. Merino, J. L. Duncan, P. Tiruveedhula, and A. Roorda. Observation of cone and rod photoreceptors in normal subjects and patients using a new generation adaptive optics scanning laser ophthalmoscope. *Biomed Opt Express*, 2(8): 2189–2201, Aug 2011.

[39] Y. Kitaguchi, S. Kusaka, T. Yamaguchi, T. Mihashi, and T. Fujikado. Detection of photoreceptor disruption by adaptive optics fundus imaging and Fourier-domain optical coherence tomography in eyes with occult macular dystrophy. *Clin Ophthalmol*, 5:345–351, 2011.

[40] R. F. Spaide and C. A. Curcio. Anatomical correlates to the bands seen in the outer retina by optical coherence tomography: literature review and model. *Retina (Philadelphia, Pa.)*, 31(8):1609–1619, Sep 2011.

[41] E. J. Fernandez, B. Hermann, B. Povazay, A. Unterhuber, H. Sattmann, B. Hofer, P. K. Ahnelt, and W. Drexler. Ultrahigh resolution optical coherence tomography and pancorrection for cellular imaging of the living human retina. *Opt Express*, 16(15):11083–11094, Jul 2008.

[42] J. Y. Lee, S. J. Chiu, P. P. Srinivasan, J. A. Izatt, C. A. Toth, S. Farsiu, and G. J. Jaffe. Fully automatic software for retinal thickness in eyes with diabetic macular edema from images acquired by cirrus and spectralis systems. *Invest. Ophthalmol. Vis. Sci.*, 54(12):7595–7602, Nov 2013.

[43] I. C. Han and G. J. Jaffe. Evaluation of artifacts associated with macular spectral-domain optical coherence tomography. *Ophthalmology*, 117(6):1177–1189, Jun 2010.

[44] H. Ishikawa, D. M. Stein, G. Wollstein, S. Beaton, J. G. Fujimoto, and J. S. Schuman. Macular segmentation with optical coherence tomography. *Invest Ophthalmol Vis Sci*, 46(6):2012–2017, Jun 2005.

[45] D. Cabrera Fernandez, H. M. Salinas, and C. A. Puliafito. Automated detection of retinal layer structures on optical coherence tomography images. *Opt Express*, 13(25):10200–10216, Dec 2005.

[46] M. Haeker, M. Sonka, R. Kardon, V. A. Shah, X. Wu, and M. D. Abràmoff. Automated segmentation of intraretinal layers from macular optical coherence tomography images. *Proc SPIE*, 6512:651214–651214–11, Mar 2007.

[47] S. Farsiu, S. J. Chiu, J. A. Izatt, and C. A. Toth. Fast detection and segmentation of drusen in retinal optical coherence tomography images. *Proc SPIE*, 6844:68440D–68440D–12, Feb 2008.

[48] M. K. Garvin, M. D. Abramoff, R. Kardon, S. R. Russell, X. Wu, and M. Sonka. Intraretinal layer segmentation of macular optical coherence tomography images using optimal 3-D graph search. *IEEE Trans Med Imaging*, 27(10):1495–1505, Oct 2008.

[49] A. M. Bagci, M. Shahidi, R. Ansari, M. Blair, N. P. Blair, and R. Zelkha. Thickness profiles of retinal layers by optical coherence tomography image segmentation. *Am J Ophthalmol*, 146(5):679–687, Nov 2008.

[50] A. Yazdanpanah, G. Hamarneh, B. R. Smith, and M. V. Sarunic. Intra-retinal Layer Segmentation in Optical Coherence Tomography Using an Active Contour Approach. In G. Yang, D. Hawkes, D. Rueckert, A. Noble, and C. Taylor, editors, *Medical Image Computing and Computer-Assisted Intervention MICCAI 2009*, volume 5762 of *Lecture Notes in Computer Science*, pages 649–656. Springer Berlin Heidelber, 2009. ISBN 978-3-642-04270-6.

[51] J. A. Eichel, A. K. Mishra, P. W. Fieguth, D. A. Clausi, and K. K. Bizheva. A Novel Algorithm for Extraction of the Layers of the Cornea. In *Computer and Robot Vision, 2009. CRV '09. Canadian Conference on*, pages 313–320, May 2009.

[52] T. Fabritius, S. Makita, M. Miura, R. Myllyla, and Y. Yasuno. Automated segmentation of the macula by optical coherence tomography. *Opt Express*, 17 (18):15659–15669, Aug 2009.

[53] M. K. Garvin, M. D. Abramoff, X. Wu, S. R. Russell, T. L. Burns, and M. Sonka. Automated 3-D intraretinal layer segmentation of macular spectral-domain optical coherence tomography images. *IEEE Trans Med Imaging*, 28 (9):1436–1447, Sep 2009.

[54] A. Mishra, A. Wong, K. Bizheva, and D. A. Clausi. Intra-retinal layer segmentation in optical coherence tomography images. *Opt Express*, 17(26):23719–23728, Dec 2009.

[55] K. Lee, M. Niemeijer, M. K. Garvin, Y. H. Kwon, M. Sonka, and M. D. Abramoff. Segmentation of the optic disc in 3-D OCT scans of the optic nerve head. *IEEE Trans Med Imaging*, 29(1):159–168, Jan 2010.

[56] S. J. Chiu, X. T. Li, P. Nicholas, C. A. Toth, J. A. Izatt, and S. Farsiu. Automatic segmentation of seven retinal layers in SDOCT images congruent with expert manual segmentation. *Opt Express*, 18(18):19413–19428, Aug 2010.

[57] S. J. Chiu, J. A. Izatt, R. V. O'Connell, K. P. Winter, C. A. Toth, and S. Farsiu. Validated automatic segmentation of AMD pathology including drusen and geographic atrophy in SD-OCT images. *Invest. Ophthalmol. Vis. Sci.*, 53(1): 53–61, Jan 2012.

[58] A. Yazdanpanah, G. Hamarneh, B. R. Smith, and M. V. Sarunic. Segmentation of intra-retinal layers from optical coherence tomography images using an active contour approach. *IEEE Trans Med Imaging*, 30(2):484–496, Feb 2011.

[59] K. A. Vermeer, J. van der Schoot, H. G. Lemij, and J. F. de Boer. Automated segmentation by pixel classification of retinal layers in ophthalmic OCT images. *Biomed Opt Express*, 2(6):1743–1756, Jun 2011.

[60] J. Tokayer, A. Ortega, and D. Huang. Sparsity-based retinal layer segmentation of optical coherence tomography images. In *Image Processing (ICIP), 2011 18th IEEE International Conference on*, pages 449–452, Sept 2011.

[61] Q. Yang, C. A. Reisman, K. Chan, R. Ramachandran, A. Raza, and D. C. Hood. Automated segmentation of outer retinal layers in macular OCT images of patients with retinitis pigmentosa. *Biomed Opt Express*, 2(9):2493–2503, Sep 2011.

[62] Y. Y. Liu, M. Chen, H. Ishikawa, G. Wollstein, J. S. Schuman, and J. M. Rehg. Automated macular pathology diagnosis in retinal OCT images using multi-scale spatial pyramid and local binary patterns in texture and shape encoding. *Med Image Anal*, 15(5):748–759, Oct 2011.

[63] D. Cabrera DeBuc. A Review of Algorithms for Segmentation of Retinal Image Data Using Optical Coherence Tomography. In P. G. Ho, editor, *Image Segmentation*, Lecture Notes in Computer Science. InTech, 2011. ISBN 978-953-307-228-9.

[64] R. Kafieh, H. Rabbani, and S. Kermani. A Review of Algorithms for Segmentation of Optical Coherence Tomography from Retina. *J Med Signals Sens*, 3 (1):45–60, Jan 2013.

[65] J. Novosel, K. A. Vermeer, G. Thepass, H. G. Lemij, and L. J. van Vliet. Loosely coupled level sets for retinal layer segmentation in optical coherence tomography. In *Biomedical Imaging (ISBI), 2013 IEEE 10th International Symposium on*, pages 1010–1013, April 2013.

[66] E. H. Sohn, J. J. Chen, K. Lee, M. Niemeijer, M. Sonka, and M. D. Abramoff. Reproducibility of diabetic macular edema estimates from SD-OCT is affected by the choice of image analysis algorithm. *Invest Ophthalmol Vis Sci*, 54(6): 4184–4188, Jun 2013.

[67] A. Lang, A. Carass, M. Hauser, E. S. Sotirchos, P. A. Calabresi, H. S. Ying, and J. L. Prince. Retinal layer segmentation of macular OCT images using boundary classification. *Biomed Opt Express*, 4(7):1133–1152, Jul 2013.

[68] M. K. Garvin, K. Lee, T. L. Burns, M. D. Abramoff, M. Sonka, and Y. H. Kwon. Reproducibility of SD-OCT-based ganglion cell-layer thickness in glaucoma using two different segmentation algorithms. *Invest Ophthalmol Vis Sci*, 54 (10):6998–7004, Oct 2013.

[69] B. J. Antony, M. D. Abramoff, M. M. Harper, W. Jeong, E. H. Sohn, Y. H. Kwon, R. Kardon, and M. K. Garvin. A combined machine-learning and graph-based framework for the segmentation of retinal surfaces in SD-OCT volumes. *Biomed Opt Express*, 4(12):2712–2728, 2013.

[70] E. Garcia-Martin, L. E. Pablo, J. Gazulla, A. Vela, J. M. Larrosa, V. Polo, M. L. Marques, and J. Alfaro. Retinal segmentation as noninvasive technique to demonstrate hyperplasia in ataxia of Charlevoix-Saguenay. *Invest Ophthalmol Vis Sci*, 54(10):7137–7142, 2013.

[71] P. P. Srinivasan, S. J. Heflin, J. A. Izatt, V. Y. Arshavsky, and S. Farsiu. Automatic segmentation of up to ten layer boundaries in sd-oct images of the

mouse retina with and without missing layers due to pathology. *Biomed Opt Express*, 5(2):348–365, Feb 2014.

[72] Y. Cha and J. Han. High-Accuracy Retinal Layer Segmentation for Optical Coherence Tomography Using Tracking Kernels Based on Gaussian Mixture Models. *Selected Topics in Quantum Electronics, IEEE Journal of*, 20(2), 2014.

[73] X. Liu, M. Shen, S. Huang, L. Leng, D. Zhu, and F. Lu. Repeatability and Reproducibility of Eight Macular Intra-Retinal Layer Thicknesses Determined by an Automated Segmentation Algorithm Using Two SD-OCT Instruments. *PLoS ONE*, 9(2):e87996, 2014.

[74] L. Duan, M. Yamanari, and Y. Yasuno. Automated phase retardation oriented segmentation of chorio-scleral interface by polarization sensitive optical coherence tomography. *Opt Express*, 20(3):3353–3366, Jan 2012.

[75] V. Kajić, M. Esmaeelpour, B. Považay, D. Marshall, P. L. Rosin, and W. Drexler. Automated choroidal segmentation of 1060 nm OCT in healthy and pathologic eyes using a statistical model. *Biomed Opt Express*, 3(1):86–103, Jan 2012.

[76] T. Torzicky, M. Pircher, S. Zotter, M. Bonesi, E. Gotzinger, and C. K. Hitzenberger. Automated measurement of choroidal thickness in the human eye by polarization sensitive optical coherence tomography. *Opt Express*, 20(7):7564–7574, Mar 2012.

[77] L. Zhang, K. Lee, M. Niemeijer, R. F. Mullins, M. Sonka, and M. D. Abramoff. Automated segmentation of the choroid from clinical SD-OCT. *Invest Ophthalmol Vis Sci*, 53(12):7510–7519, Nov 2012.

[78] J. Tian, P. Marziliano, M. Baskaran, T. A. Tun, and T. Aung. Automatic segmentation of the choroid in enhanced depth imaging optical coherence tomography images. *Biomed Opt Express*, 4(3):397–411, Mar 2013.

[79] S. Lee, N. Fallah, F. Forooghian, A. Ko, K. Pakzad-Vaezi, A. B. Merkur, A. W. Kirker, D. A. Albiani, M. Young, M. V. Sarunic, and M. F. Beg. Comparative analysis of repeatability of manual and automated choroidal thickness measurements in nonneovascular age-related macular degeneration. *Invest Ophthalmol Vis Sci*, 54(4):2864–2871, Apr 2013.

[80] D. A. Sim, P. A. Keane, H. Mehta, S. Fung, J. Zarranz-Ventura, M. Fruttiger, P. J. Patel, C. A. Egan, and A. Tufail. Repeatability and reproducibility of choroidal vessel layer measurements in diabetic retinopathy using enhanced depth optical coherence tomography. *Invest Ophthalmol Vis Sci*, 54(4):2893–2901, Apr 2013.

[81] L. Duan, Y. J. Hong, and Y. Yasuno. Automated segmentation and characterization of choroidal vessels in high-penetration optical coherence tomography. *Opt Express*, 21(13):15787–15808, Jul 2013.

[82] H. Lu, N. Boonarpha, M. T. Kwong, and Y. Zheng. Automated segmentation of the choroid in retinal optical coherence tomography images. *Conf Proc IEEE Eng Med Biol Soc*, 2013:5869–5872, 2013.

[83] D. Alonso-Caneiro, S. A. Read, and M. J. Collins. Automatic segmentation of choroidal thickness in optical coherence tomography. *Biomed Opt Express*, 4 (12):2795–2812, 2013.

[84] F. A. Almobarak, N. O'Leary, A. S. Reis, G. P. Sharpe, D. M. Hutchison, M. T. Nicolela, and B. C. Chauhan. Automated Segmentation of Optic Nerve Head Structures with Optical Coherence Tomography. *Invest Ophthalmol Vis Sci*, Jan 2014.

[85] F. Larocca, S. J. Chiu, R. P. McNabb, A. N. Kuo, J. A. Izatt, and S. Farsiu. Robust automatic segmentation of corneal layer boundaries in SDOCT images using graph theory and dynamic programming. *Biomed Opt Express*, 2(6): 1524–1538, Jun 2011.

[86] W. Du, X. Tian, and Y. Sun. A novel edge tracking approach for cornea in optical coherence tomography anterior chamber images. *Conf Proc IEEE Eng Med Biol Soc*, 2013:1434–1437, 2013.

[87] S. J. Chiu, C. A. Toth, C. Bowes Rickman, J. A. Izatt, and S. Farsiu. Automatic segmentation of closed-contour features in ophthalmic images using graph theory and dynamic programming. *Biomed Opt Express*, 3(5):1127–1140, May 2012.

[88] D. C. Fernandez. Delineating fluid-filled region boundaries in optical coherence tomography images of the retina. *IEEE Trans Med Imaging*, 24:929–945, Aug 2005.

[89] C. Ahlers, C. Simader, W. Geitzenauer, G. Stock, P. Stetson, S. Dastmalchi, and U. Schmidt-Erfurth. Automatic segmentation in three-dimensional analysis of fibrovascular pigmentepithelial detachment using high-definition optical coherence tomography. *Br J Ophthalmol*, 92(2):197–203, Feb 2008.

[90] G. Quellec, K. Lee, M. Dolejsi, M. K. Garvin, M. D. Abramoff, and M. Sonka. Three-dimensional analysis of retinal layer texture: identification of fluid-filled regions in SD-OCT of the macula. *IEEE Trans Med Imaging*, 29(6):1321–1330, Jun 2010.

[91] X. Chen, M. Niemeijer, L. Zhang, K. Lee, M. D. Abramoff, and M. Sonka. Three-dimensional segmentation of fluid-associated abnormalities in retinal OCT: probability constrained graph-search-graph-cut. *IEEE Trans Med Imaging*, 31(8):1521–1531, Aug 2012.

[92] M. Fadzil Abdul Kadir, S. Tsuruoka, H. Takase, H. Kawanaka, F. Okuyama, Y. Uji, H. Matsubara, and H. Yagami. Automatic extraction of retinal disease area for optical coherence tomography image using regional statistic. *Global Journal on Technology*, 1, 2012.

[93] D. Xu, A. Yuan, P. K. Kaiser, S. K. Srivastava, R. P. Singh, J. E. Sears, D. F. Martin, and J. P. Ehlers. A novel segmentation algorithm for volumetric analysis of macular hole boundaries identified with optical coherence tomography. *Invest Ophthalmol Vis Sci*, 54(1):163–169, Jan 2013.

[94] M. Pilch, K. Stieger, Y. Wenner, M. N. Preising, C. Friedburg, E. Meyer zu Bexten, and B. Lorenz. Automated segmentation of pathological cavities in optical coherence tomography scans. *Invest Ophthalmol Vis Sci*, 54(6):4385–4393, Jun 2013.

[95] S. Roychowdhury, D. D. Koozekanani, S. Radwan, and K. K. Parhi. Automated localization of cysts in diabetic macular edema using optical coherence tomography images. *Conf Proc IEEE Eng Med Biol Soc*, 2013:1426–1429, 2013.

[96] W. Ding, M. Young, S. Bourgault, S. Lee, D. A. Albiani, A. W. Kirker, F. Forooghian, M. V. Sarunic, A. B. Merkur, and M. F. Beg. Automatic detection of subretinal fluid and sub-retinal pigment epithelium fluid in optical coherence tomography images. *Conf Proc IEEE Eng Med Biol Soc*, 2013: 7388–7391, 2013.

[97] R. T. Smith, J. K. Chan, T. Nagasaki, U. F. Ahmad, I. Barbazetto, J. Sparrow, M. Figueroa, and J. Merriam. Automated detection of macular drusen using geometric background leveling and threshold selection. *Arch Ophthalmol*, 123 (2):200–206, Feb 2005.

[98] N. Lee, A. F. Laine, and R. T. Smith. A hybrid segmentation approach for geographic atrophy in fundus auto-fluorescence images for diagnosis of age-related macular degeneration. *Conf Proc IEEE Eng Med Biol Soc*, 2007:4965–4968, 2007.

[99] A. D. Mora, P. M. Vieira, A. Manivannan, and J. M. Fonseca. Automated drusen detection in retinal images using analytical modelling algorithms. *Biomed Eng Online*, 10:59, 2011.

[100] S. Tsantis, G. C. Kagadis, K. Katsanos, D. Karnabatidis, G. Bourantas, and G. C. Nikiforidis. Automatic vessel lumen segmentation and stent strut detection in intravascular optical coherence tomography. *Med Phys*, 39(1):503–513, Jan 2012.

[101] S. J. Chiu, Y. Lokhnygina, A. M. Dubis, A. Dubra, J. Carroll, J. A. Izatt, and S. Farsiu. Automatic cone photoreceptor segmentation using graph theory and dynamic programming. *Biomed Opt Express*, 4(6):924–937, Jun 2013.

[102] K. Y. Li and A. Roorda. Automated identification of cone photoreceptors in adaptive optics retinal images. *J Opt Soc Am A Opt Image Sci Vis*, 24(5): 1358–1363, May 2007.

[103] B. Xue, S. S. Choi, N. Doble, and J. S. Werner. Photoreceptor counting and montaging of en-face retinal images from an adaptive optics fundus camera. *J Opt Soc Am A Opt Image Sci Vis*, 24(5):1364–1372, May 2007.

[104] M. Pircher, J. S. Kroisamer, F. Felberer, H. Sattmann, E. Gotzinger, and C. K. Hitzenberger. Temporal changes of human cone photoreceptors observed in vivo with SLO/OCT. *Biomed Opt Express*, 2(1):100–112, 2011.

[105] K. Loquin, I. Bloch, K. Nakashima, F. Rossant, and M. Paques. Photoreceptor detection in in-vivo Adaptive Optics images of the retina: Towards a simple interactive tool for the physicians. In *Biomedical Imaging: From Nano to Macro, 2011 IEEE International Symposium on*, pages 191–194, March 2011.

[106] S. V. Patel, J. W. McLaren, J. J. Camp, L. R. Nelson, and W. M. Bourne. Automated quantification of keratocyte density by using confocal microscopy in vivo. *Invest. Ophthalmol. Vis. Sci.*, 40(2):320–326, Feb 1999.

[107] F. J. Sanchez-Marin. Automatic segmentation of contours of corneal cells. *Comput. Biol. Med.*, 29(4):243–258, Jul 1999.

[108] A. Ruggeri, E. Grisan, and J. Jaroszewski. A new system for the automatic estimation of endothelial cell density in donor corneas. *Br J Ophthalmol*, 89 (3):306–311, Mar 2005.

[109] M. E. Diaz, G. Ayala, R. Sebastian, and L. Martinez-Costa. Granulometric analysis of corneal endothelium specular images by using a germ-grain model. *Comput. Biol. Med.*, 37(3):364–375, Mar 2007.

[110] A. H. Karimi, A. Wong, and K. Bizheva. Automated detection and cell density assessment of keratocytes in the human corneal stroma from ultrahigh resolution optical coherence tomograms. *Biomed Opt Express*, 2(10):2905–2916, Oct 2011.

[111] J. A. Bondy and U. S. R. Murty. *Graph theory with applications*, volume 6. Elsevier Science Publishing Co., Inc., 1976.

[112] Edsger. W. Dijkstra. A note on two problems in connexion with graphs. *Numerische Mathematik*, 1:269–271, 1959.

[113] J. Shi and J. Malik. Normalized cuts and image segmentation. *Pattern Analysis and Machine Intelligence, IEEE Transactions on*, 22(8):888–905, Aug 2000.

[114] F. B. Zhan and C. E. Noon. Shortest path algorithms: an evaluation using real road networks. *Transportation Science*, 32(1):65–73, Feb 1998.

[115] R. E. Bellman. On a routing problem. *Quarterly of Applied Mathematics*, 16: 87–90, 1958.

[116] P. Elias, A. Feinstein, and C.E. Shannon. A note on the maximum flow through a network. *Information Theory, IRE Transactions on*, 2(4):117–119, Dec 1956.

[117] S. Warshall. A Theorm on Boolean Matrices. *J ACM*, 9(1):11–12, Jan 1962.

[118] L. R. Ford and D. R. Fulkerson. *Flows in networks*, volume 3. Princeton University Press, Princeton, NJ, USA, 1962.

[119] R. W. Floyd. Algorithm 97: Shortest Path. *Commun ACM*, 5(6):345, Jun 1962.

[120] C. A. Glasbey and M. J. Young. Maximum a posteriori estimation of image boundaries by dynamic programming. *J Roy Stat Soc C-App*, 51(2):209–221, Nov 2002.

[121] S. Timp and N. Karssemeijer. A new 2D segmentation method based on dynamic programming applied to computer aided detection in mammography. *Med Phys*, 31(5):958–971, May 2004.

[122] Z. Yan, B. J. Matuszewski, S. Lik-Kwan, and C. J. Moore. A Novel Medical Image Segmentation Method using Dynamic Programming. In *Medical Information Visualisation - BioMedical Visualisation, 2007. MediVis 2007. International Conference on*, pages 69–74, Jul 2007.

[123] S. Lu. Accurate and efficient optic disc detection and segmentation by a circular transformation. *IEEE Trans Med Imaging*, 30(12):2126–2133, Dec 2011.

[124] S. Farsiu, J. Christofferson, B. Eriksson, P. Milanfar, B. Friedlander, Shakouri. A, and R. Nowak. Statistical detection and imaging of objects hidden in turbid media using ballistic photons. *Appl Opt*, 46(23):5805–5822, Aug 2007.

[125] N. Otsu. A threshold selection method from gray-level histograms. *Systems, Man and Cybernetics, IEEE Transactions on*, 9(1):62–66, Jan 1979.

[126] R. C. Gonzalez and R. E. Woods. *Digital Image Processing (3rd Edition)*. Prentice-Hall, Upper Saddle River, NJ, USA, 2008.

[127] Age-Related Eye Disease Study Research Group. The Age-Related Eye Disease Study system for classifying age-related macular degeneration from stereoscopic color fundus photographs: the Age-Related Eye Disease Study Report Number 6. *Am J Ophthalmol*, 132(5):668–681, Nov 2001.

[128] A. Roorda and D. R. Williams. The arrangement of the three cone classes in the living human eye. *Nature*, 397(6719):520–522, Feb 1999.

[129] A. Dubra, Y. Sulai, J. L. Norris, R. F. Cooper, A. M. Dubis, D. R. Williams, and J. Carroll. Noninvasive imaging of the human rod photoreceptor mosaic using a confocal adaptive optics scanning ophthalmoscope. *Biomed Opt Express*, 2(7):1864–1876, Jul 2011.

[130] T. Y. Chui, H. Song, and S. A. Burns. Individual variations in human cone photoreceptor packing density: variations with refractive error. *Invest Ophthalmol Vis Sci*, 49(10):4679–4687, Oct 2008.

[131] T. Y. Chui, H. Song, and S. A. Burns. Adaptive-optics imaging of human cone photoreceptor distribution. *J Opt Soc Am A Opt Image Sci Vis*, 25(12): 3021–3029, Dec 2008.

[132] K. Y. Li, P. Tiruveedhula, and A. Roorda. Intersubject variability of foveal cone photoreceptor density in relation to eye length. *Invest Ophthalmol Vis Sci*, 51(12):6858–6867, Dec 2010.

[133] Y. Kitaguchi, K. Bessho, T. Yamaguchi, N. Nakazawa, T. Mihashi, and T. Fujikado. In vivo measurements of cone photoreceptor spacing in myopic eyes from images obtained by an adaptive optics fundus camera. *Jpn J Ophthalmol*, 51(6):456–461, 2007.

[134] A. Roorda and D. R. Williams. Optical fiber properties of individual human cones. *J Vis*, 2(5):404–412, 2002.

[135] O. P. Kocaoglu, S. Lee, R. S. Jonnal, Q. Wang, A. E. Herde, J. C. Derby, W. Gao, and D. T. Miller. Imaging cone photoreceptors in three dimensions and in time using ultrahigh resolution optical coherence tomography with adaptive optics. *Biomed Opt Express*, 2(4):748–763, 2011.

[136] D. H. Wojtas, B. Wu, P. K. Ahnelt, P. J. Bones, and R. P. Millane. Automated analysis of differential interference contrast microscopy images of the foveal cone mosaic. *J Opt Soc Am A Opt Image Sci Vis*, 25(5):1181–1189, May 2008.

[137] K. Loquin, I. Bloch, K. Nakashima, F. Rossant, P. Boelle, and M. Paques. Automatic Photoreceptor Detection in In-Vivo Adaptive Optics Retinal Images: Statistical Validation. In A. Campilho and M. Kamel, editors, *Image Analysis and Recognition*, volume 7325 of *Lecture Notes in Computer Science*, pages 408k–415. Springer Berlin Heidelberg, 2012.

[138] X. Liu, Y. Zhang, and D. Yun. An automated algorithm for photoreceptors counting in adaptive optics retinal images. *Proc SPIE*, 8419:84191Z–84191Z–5, 2012.

[139] R. Garrioch, C. Langlo, A. M. Dubis, R. F. Cooper, A. Dubra, and J. Carroll. Repeatability of in vivo parafoveal cone density and spacing measurements. *Optom Vis Sci*, 89(5):632–643, May 2012.

[140] D. S. Biggs and M. Andrews. Acceleration of iterative image restoration algorithms. *Appl Opt*, 36(8):1766–1775, Mar 1997.

[141] T. J. Holmes, S. Bhattacharyya, J. A. Cooper, D. Hanzel, V. Krishnamurthi, W. Lin, B. Roysam, D. H. Szarowski, and J. N. Turner. Light Microscopic Images Reconstructed by Maximum Likelihood Deconvolution. In J. B. Pawley, editor, *Handbook of Biological Confocal Microscopy*, pages 389–402. Springer US, 1995.

[142] R. J. Hanisch, R. L. White, and R. L. Gilliland. Deconvolution of hubble space telescope images and spectra. In P. A. Jansson, editor, *Deconvolution of images and spectra*. Courier Dover Publications, 2012.

[143] R. F. Cooper, A. M. Dubis, A. Pavaskar, J. Rha, A. Dubra, and J. Carroll. Spatial and temporal variation of rod photoreceptor reflectance in the human retina. *Biomed Opt Express*, 2(9):2577–2589, Sep 2011.

[144] A. Dubra and Z. Harvey. Registration of 2D Images from Fast Scanning Ophthalmic Instruments. In B. Fischer, B. Dawant, and C. Lorenz, editors, *Biomedical Image Registration*, volume 6204 of *Lecture Notes in Computer Science*, pages 60–71. Springer Berlin Heidelberg, 2010.

[145] K. Liang and S. L. Zeger. Longitudinal Data Analysis Using Generalized Linear Models. *Biometrika*, 73(1):13–22, 1986.

[146] N. M. Bressler. Age-related macular degeneration is the leading cause of blindness.. *JAMA*, 291(15):1900–1901, Apr 2004.

[147] A. A. Khanifar, A. F. Koreishi, J. A. Izatt, and C. A. Toth. Drusen ultrastructure imaging with spectral domain optical coherence tomography in age-related macular degeneration. *Ophthalmology*, 115(11):1883–1890, Nov 2008.

[148] N. Jain, S. Farsiu, A. A. Khanifar, S. Bearelly, R. T. Smith, J. A. Izatt, and C. A. Toth. Quantitative comparison of drusen segmented on SD-OCT versus drusen delineated on color fundus photographs. *Invest Ophthalmol Vis Sci*, 51 (10):4875–4883, Oct 2010.

[149] S. G. Schuman, A. F. Koreishi, S. Farsiu, S. H. Jung, J. A. Izatt, and C. A. Toth. Photoreceptor layer thinning over drusen in eyes with age-related macular degeneration imaged in vivo with spectral-domain optical coherence tomography. *Ophthalmology*, 116(3):488–496, Mar 2009.

[150] G. S. Hageman, P. J. Luthert, N. H. Victor Chong, L. V. Johnson, D. H. Anderson, and R. F. Mullins. An integrated hypothesis that considers drusen as biomarkers of immune-mediated processes at the RPE-Bruch's membrane interface in aging and age-related macular degeneration. *Prog Retin Eye Res*, 20(6):705–732, Nov 2001.

[151] D. Pauleikhoff, M. J. Barondes, D. Minassian, I. H. Chisholm, and A. C. Bird. Drusen as risk factors in age-related macular disease. *Am J Ophthalmol*, 109 (1):38–43, Jan 1990.

[152] Z. Yehoshua, P. J. Rosenfeld, G. Gregori, W. J. Feuer, M. Falcao, B. J. Lujan, and C. Puliafito. Progression of geographic atrophy in age-related macular degeneration imaged with spectral domain optical coherence tomography. *Ophthalmology*, 118(4):679–686, Apr 2011.

[153] S. Bearelly, F. Y. Chau, A. Koreishi, S. S. Stinnett, J. A. Izatt, and C. A. Toth. Spectral domain optical coherence tomography imaging of geographic atrophy margins. *Ophthalmology*, 116(9):1762–1769, Sep 2009.

[154] K. Rapantzikos, M. Zervakis, and K. Balas. Detection and segmentation of drusen deposits on human retina: potential in the diagnosis of age-related macular degeneration. *Med Image Anal*, 7(1):95–108, Mar 2003.

[155] M. Niemeijer, B. van Ginneken, S. R. Russell, M. S. Suttorp-Schulten, and M. D. Abramoff. Automated detection and differentiation of drusen, exudates, and cotton-wool spots in digital color fundus photographs for diabetic retinopathy diagnosis. *Invest Ophthalmol Vis Sci*, 48(5):2260–2267, May 2007.

[156] D. E. Freund, N. Bressler, and P. Burlina. Automated detection of drusen in the macula. In *Biomedical Imaging: From Nano to Macro, 2009. ISBI '09. IEEE International Symposium on*, pages 61–64, June 2009.

[157] C. Kose, U. Sevik, O. Gencalioglu, C. Ikibas, and T. Kayikicioglu. A statistical segmentation method for measuring age-related macular degeneration in retinal fundus images. *J Med Syst*, 34(1):1–13, Feb 2010.

[158] R. J. Zawadzki, A. R. Fuller, D. F. Wiley, B. Hamann, S. S. Choi, and J. S. Werner. Adaptation of a support vector machine algorithm for segmentation and visualization of retinal structures in volumetric optical coherence tomography data sets. *J Biomed Opt*, 12(4):041206, 2007.

[159] K. Yi, M. Mujat, B. H. Park, W. Sun, J. W. Miller, J. M. Seddon, L. H. Young, J. F. de Boer, and T. C. Chen. Spectral domain optical coherence tomography for quantitative evaluation of drusen and associated structural changes in non-neovascular age-related macular degeneration. *Br J Ophthalmol*, 93(2):176–181, Feb 2009.

[160] M. Szkulmowski, M. Wojtkowski, B. Sikorski, T. Bajraszewski, V. J. Srinivasan, A. Szkulmowska, J. J. Kaluzny, J. G. Fujimoto, and A. Kowalczyk. Analysis of posterior retinal layers in spectral optical coherence tomography images of the normal retina and retinal pathologies. *J Biomed Opt*, 12(4): 041207, 2007.

[161] Q. Yang, C. A. Reisman, Z. Wang, Y. Fukuma, M. Hangai, N. Yoshimura, A. Tomidokoro, M. Araie, A. S. Raza, D. C. Hood, and K. Chan. Automated layer segmentation of macular OCT images using dual-scale gradient information. *Opt Express*, 18(20):21293–21307, Sep 2010.

[162] G. Gregori, F. Wang, P. J. Rosenfeld, Z. Yehoshua, N. Z. Gregori, B. J. Lujan, C. A. Puliafito, and W. J. Feuer. Spectral domain optical coherence tomography imaging of drusen in nonexudative age-related macular degeneration. *Ophthalmology*, 118(7):1373–1379, Jul 2011.

[163] F. G. Schlanitz, C. Ahlers, S. Sacu, C. Schutze, M. Rodriguez, S. Schriefl, I. Golbaz, T. Spalek, G. Stock, and U. Schmidt-Erfurth. Performance of drusen detection by spectral-domain optical coherence tomography. *Invest Ophthalmol Vis SciW*, 51(12):6715–6721, Dec 2010.

[164] M. R. Hee, D. Huang, E. A. Swanson, and J. G. Fujimoto. Polarization-sensitive low-coherence reflectometer for birefringence characterization and ranging. *J Opt Soc Am B*, 9(6):903–908, Jun 1992.

[165] E. Gotzinger, M. Pircher, W. Geitzenauer, C. Ahlers, B. Baumann, S. Michels, U. Schmidt-Erfurth, and C. K. Hitzenberger. Retinal pigment epithelium segmentation by polarization sensitive optical coherence tomography. *Opt Express*, 16(21):16410–16422, Oct 2008.

[166] P. J. Patel, F. K. Chen, L. da Cruz, and A. Tufail. Segmentation error in Stratus optical coherence tomography for neovascular age-related macular degeneration. *Invest Ophthalmol Vis Sci*, 50(1):399–404, Jan 2009.

[167] P. A. Keane, S. Liakopoulos, R. V. Jivrajka, K. T. Chang, T. Alasil, A. C. Walsh, and S. R. Sadda. Evaluation of optical coherence tomography retinal thickness parameters for use in clinical trials for neovascular age-related macular degeneration. *Invest Ophthalmol Vis Sci*, 50(7):3378–3385, Jul 2009.

[168] S. Tatlipinar, S. M. Shah, P. A. Campochiaro, and Q. D. Nguyen. Intraobserver repeatability of automated versus adjusted optical coherence tomography measurements in patients with neovascular age-related macular degeneration. *Ophthalmologica*, 221(4):227–232, 2007.

[169] S. A. Zweifel, R. F. Spaide, C. A. Curcio, G. Malek, and Y. Imamura. Reticular pseudodrusen are subretinal drusenoid deposits. *Ophthalmology*, 117(2):303–312, Feb 2010.

[170] R. F. Spaide and C. A. Curcio. Drusen characterization with multimodal imaging. *Retina (Philadelphia, Pa.)*, 30(9):1441–1454, Oct 2010.

[171] R. F. Spaide, C. A. Curcio, and S. A. Zweifel. Drusen, an old but new frontier. *Retina (Philadelphia, Pa.)*, 30(8):1163–1165, Sep 2010.

[172] M. Fleckenstein, P. Charbel Issa, H. M. Helb, S. Schmitz-Valckenberg, R. P. Finger, H. P. Scholl, K. U. Loeffler, and F. G. Holz. High-resolution spectral domain-OCT imaging in geographic atrophy associated with age-related macular degeneration. *Invest Ophthalmol Vis Sci*, 49(9):4137–4144, Sep 2008.

[173] S. Sarks, S. Cherepanoff, M. Killingsworth, and J. Sarks. Relationship of Basal laminar deposit and membranous debris to the clinical presentation of early age-related macular degeneration. *Invest. Ophthalmol. Vis. Sci.*, 48(3):968–977, Mar 2007.

[174] S. A. Zweifel, Y. Imamura, T. C. Spaide, T. Fujiwara, and R. F. Spaide. Prevalence and significance of subretinal drusenoid deposits (reticular pseudodrusen) in age-related macular degeneration. *Ophthalmology*, 117(9):1775–1781, Sep 2010.

[175] B. J. Lujan, P. J. Rosenfeld, G. Gregori, F. Wang, R. W. Knighton, W. J. Feuer, and C. A. Puliafito. Spectral domain optical coherence tomographic imaging of geographic atrophy. *Ophthalmic Surg Lasers Imaging*, 40(2):96–101, 2009.

[176] C. B. Barber, D. P. Dobkin, and H. Huhdanpaa. The Quickhull Algorithm for Convex Hulls. *ACM Trans Math Softw*, 22(4):469–483, Dec 1996.

[177] L. V. Johnson, W. P. Leitner, A. J. Rivest, M. K. Staples, M. J. Radeke, and D. H. Anderson. The Alzheimer's A beta -peptide is deposited at sites of complement activation in pathologic deposits associated with aging and age-related macular degeneration. *Proc Natl Acad Sci U.S.A.*, 99(18):11830–11835, Sep 2002.

[178] R. F. Mullins, S. R. Russell, D. H. Anderson, and G. S. Hageman. Drusen associated with aging and age-related macular degeneration contain proteins common to extracellular deposits associated with atherosclerosis, elastosis, amyloidosis, and dense deposit disease. *FASEB J*, 14(7):835–846, May 2000.

[179] L. Wang, M. E. Clark, D. K. Crossman, K. Kojima, J. D. Messinger, J. A. Mobley, and C. A. Curcio. Abundant lipid and protein components of drusen. *PLoS ONE*, 5(4):e10329, 2010.

[180] M. A. Zarbin. Current concepts in the pathogenesis of age-related macular degeneration. *Arch Ophthalmol*, 122(4):598–614, Apr 2004.

[181] J. P. Sarks, S. H. Sarks, and M. C. Killingsworth. Evolution of soft drusen in age-related macular degeneration. *Eye (Lond)*, 8 (Pt 3):269–283, 1994.

[182] C. A. Curcio and C. L. Millican. Basal linear deposit and large drusen are specific for early age-related maculopathy. *Arch Ophthalmol*, 117(3):329–339, Mar 1999.

[183] C. A. Curcio, J. D. Messinger, K. R. Sloan, A. Mitra, G. McGwin, and R. F. Spaide. Human chorioretinal layer thicknesses measured in macula-wide, high-resolution histologic sections. *Invest Ophthalmol Vis Sci*, 52(7):3943–3954, Jun 2011.

[184] D. C. Hood, C. E. Lin, M. A. Lazow, K. G. Locke, X. Zhang, and D. G. Birch. Thickness of receptor and post-receptor retinal layers in patients with retinitis pigmentosa measured with frequency-domain optical coherence tomography. *Invest Ophthalmol Vis Sci*, 50(5):2328–2336, May 2009.

[185] S. Schmitz-Valckenberg, J. S. Steinberg, M. Fleckenstein, S. Visvalingam, C. K. Brinkmann, and F. G. Holz. Combined confocal scanning laser ophthalmoscopy and spectral-domain optical coherence tomography imaging of reticular drusen associated with age-related macular degeneration. *Ophthalmology*, 117(6): 1169–1176, Jun 2010.

[186] R. P. Finger, P. Charbel Issa, U. Kellner, S. Schmitz-Valckenberg, M. Fleckenstein, H. P. Scholl, and F. G. Holz. Spectral domain optical coherence tomography in adult-onset vitelliform macular dystrophy with cuticular drusen. *Retina (Philadelphia, Pa.)*, 30(9):1455–1464, Oct 2010.

[187] M. A. Grassi, J. C. Folk, T. E. Scheetz, C. M. Taylor, V. C. Sheffield, and E. M. Stone. Complement factor H polymorphism p.Tyr402His and cuticular Drusen. *Arch Ophthalmol*, 125(1):93–97, Jan 2007.

[188] P. Soille. *Morphological Image Analysis: Principles and Applications*. Springer-Verlag New York, Inc., Secaucus, NJ, USA, 2 edition, 2003.

[189] H. Takeda, S. Farsiu, and P. Milanfar. Kernel regression for image processing and reconstruction. *IEEE Trans Image Process*, 16(2):349–366, Feb 2007.

[190] L. Fang, S. Li, Q. Nie, J. A. Izatt, C. A. Toth, and S. Farsiu. Sparsity based denoising of spectral domain optical coherence tomography images. *Biomed Opt Express*, 3(5):927–942, May 2012.

[191] W. Gao, E. Tatrai, V. Olvedy, B. Varga, L. Laurik, A. Somogyi, G Somfai, and D. DeBuc. Investigation of changes in thickness and reflectivity from layered retinal structures of healthy and diabetic eyes with optical coherence tomography. *J Biomed Sci Eng*, 4:657–665, 2011.

[192] I. Krebs, E. Smretschnig, S. Moussa, W. Brannath, I. Womastek, and S. Binder. Quality and reproducibility of retinal thickness measurements in two spectral-domain optical coherence tomography machines. *Invest Ophthalmol Vis Sci*, 52(9):6925–6933, Aug 2011.

[193] M. Kakinoki, T. Miyake, O. Sawada, T. Sawada, H. Kawamura, and M. Ohji. Comparison of macular thickness in diabetic macular edema using spectral-domain optical coherence tomography and time-domain optical coherence tomography. *J Ophthalmol*, 2012:959721, 2012.

[194] F. M. Heussen, Y. Ouyang, E. C. McDonnell, R. Narala, H. Ruiz-Garcia, A. C. Walsh, and S. R. Sadda. Comparison of manually corrected retinal thickness measurements from multiple spectral-domain optical coherence tomography instruments. *Br J Ophthalmol*, 96(3):380–385, Mar 2012.

[195] M. R. Hee, C. A. Puliafito, C. Wong, J. S. Duker, E. Reichel, B. Rutledge, J. S. Schuman, E. A. Swanson, and J. G. Fujimoto. Quantitative assessment of macular edema with optical coherence tomography. *Arch Ophthalmol*, 113 (8):1019–1029, Aug 1995.

[196] J. Lammer, C. Scholda, C. Prunte, T. Benesch, U. Schmidt-Erfurth, and M. Bolz. Retinal thickness and volume measurements in diabetic macular edema: a comparison of four optical coherence tomography systems. *Retina (Philadelphia, Pa.)*, 31(1):48–55, Jan 2011.

[197] M. A. Ibrahim, Y. J. Sepah, R. C. Symons, R. Channa, E. Hatef, A. Khwaja, M. Bittencourt, J. Heo, D. V. Do, and Q. D. Nguyen. Spectral- and time-domain optical coherence tomography measurements of macular thickness in normal eyes and in eyes with diabetic macular edema. *Eye (Lond)*, 26(3): 454–462, Mar 2012.

[198] R. M. Cormack. A review of classification. *Journal of the Royal Statistical Society. Series A (General)*, 134(3):321–367, 1971.

[199] S. B. Kotsiantis. Supervised machine learning: a review of classification techniques. *Informatica*, 31(3):249–268, 2007.

[200] D. Ruppert and M. P. Wand. Multivariate locally weighted least squares regression. *The annals of statistics*, 22(3):1346–1370, 1994.

[201] P. C. Hansen. The truncated SVD as a method for regularization. *BIT Numerical Mathematics*, 27(4):534–553, 1987.

[202] X. G. Feng and P. Milanfar. Multiscale principal components analysis for image local orientation estimation. In *Signals, Systems and Computers, 2002. Conference Record of the Thirty-Sixth Asilomar Conference on*, pages 478–482, Nov 2002.

[203] R. M. Haralick, K. Shanmugam, and I. Dinstein. Textural Features for Image Classification. *Systems, Man and Cybernetics, IEEE Transactions on*, SMC-3 (6):610–621, Nov 1973.

[204] L. S. Davis, S. A. Johns, and J. K. Aggarwal. Pattern Analysis and Machine Intelligence, IEEE Transactions on. *Systems, Man and Cybernetics, IEEE Transactions on*, PAMI-1(3):251–259, July 1979.

[205] C. C. Gotlieb and H. E. Kreyszig. Texture descriptors based on co-occurrence matrices. *Computer Vision, Graphics, and Image Processing*, 51(1):70–86, 1990.

[206] G. Stockman and L. G. Shapiro. *Computer Vision*. Prentice Hall PTR, Upper Saddle River, NJ, USA, 2001.

[207] K. I. Laws. Textured image segmentation. Technical report, DTIC Document, 1980.

[208] A. Jain and D. Zongker. Feature selection: evaluation, application, and small sample performance. *Pattern Analysis and Machine Intelligence, IEEE Transactions on*, 19(2):153–158, Feb 1997.

[209] R. Kohavi and G. H. John. Wrappers for feature subset selection. *Artificial Intelligence*, 97(1-2):273–324, Feb 1997.

[210] I. Guyon and A. Elisseeff. An Introduction to Variable and Feature Selection. *J Mach Learn Res*, 3(1-2):1157–1182, 2003.

[211] F. Mosteller and J. W. Tukey. *Data analysis, including statistics*. Addison-Wesley, 1968.

[212] R. Kohavi. A Study of Cross-validation and Bootstrap for Accuracy Estimation and Model Selection. In *Proceedings of the 14th International Joint Conference on Artificial Intelligence - Volume 2*, IJCAI'95, pages 1137–1143, San Francisco, CA, USA, 1995.

[213] J. D. Rodriguez, A. Perez, and J. A. Lozano. Sensitivity Analysis of k-Fold Cross Validation in Prediction Error Estimation. *Pattern Analysis and Machine Intelligence, IEEE Transactions on*, 32(3):569–575, Mar 2010.

[214] S. Arlot and A. Celisse. A survey of cross-validation procedures for model selection. *Statist Surv*, 4:40–79, 2010.

[215] American Academy of Ophthalmology Retina Panel. Preferred Practice Pattern Guidelines. Diabetic Retinopathy. *Diabetes Care*, 2008.

[216] J. W. Yau, S. L. Rogers, R. Kawasaki, E. L. Lamoureux, J. W. Kowalski, T. Bek, S. J. Chen, J. M. Dekker, A. Fletcher, J. Grauslund, S. Haffner, R. F. Hamman, M. K. Ikram, T. Kayama, B. E. Klein, R. Klein, S. Krishnaiah, K. Mayurasakorn, J. P. O'Hare, T. J. Orchard, M. Porta, M. Rema, M. S. Roy, T. Sharma, J. Shaw, H. Taylor, J. M. Tielsch, R. Varma, J. J. Wang, N. Wang, S. West, L. Xu, M. Yasuda, X. Zhang, P. Mitchell, T. Y. Wong, and Meta-Analysis for Eye Disease (META-EYE) Study Group. Global prevalence and major risk factors of diabetic retinopathy. *Diabetes Care*, 35(3):556–564, Mar 2012.

[217] S. L. Robbins and R. S. Cotran. *Pathologic basis of disease*. Saunders, 1979.

[218] J. Pe'er, R. Folberg, A. Itin, H. Gnessin, I. Hemo, and E. Keshet. Upregulated expression of vascular endothelial growth factor in proliferative diabetic retinopathy. *Br J Ophthalmol*, 80(3):241–245, Mar 1996.

[219] M. J. Tolentino, D. S. McLeod, M. Taomoto, T. Otsuji, A. P. Adamis, and G. A. Lutty. Pathologic features of vascular endothelial growth factor-induced retinopathy in the nonhuman primate. *Am J Ophthalmol*, 133(3):373–385, Mar 2002.

[220] A. Bringmann, T. Pannicke, J. Grosche, M. Francke, P. Wiedemann, S. N. Skatchkov, N. N. Osborne, and A. Reichenbach. Mller cells in the healthy and diseased retina. *Prog Retin Eye Res*, 25(4):397–424, Jul 2006.

[221] A. Bringmann, A. Reichenbach, and P. Wiedemann. Pathomechanisms of cystoid macular edema. *Ophthalmic Res*, 36(5):241–249, 2004.

[222] A. Negi and M. F. Marmor. The resorption of subretinal fluid after diffuse damage to the retinal pigment epithelium. *Invest Ophthalmol Vis Sci*, 24(11): 1475–1479, Nov 1983.

[223] M. F. Marmor. Mechanisms of fluid accumulation in retinal edema. *Doc Ophthalmol*, 97(3-4):239–249, 1999.

[224] Early Treatment Diabetic Retinopathy Study Research Group. Treatment techniques and clinical guidelines for photocoagulation of diabetic macular edema. Early Treatment Diabetic Retinopathy Study Report Number 2. Early Treatment Diabetic Retinopathy Study Research Group. *Ophthalmology*, 94 (7):761–774, Jul 1987.

[225] E. T. Cunningham, A. P. Adamis, M. Altaweel, L. P. Aiello, N. M. Bressler, D. J. D'Amico, M. Goldbaum, D. R. Guyer, B. Katz, M. Patel, and S. D. Schwartz. A phase II randomized double-masked trial of pegaptanib, an anti-vascular endothelial growth factor aptamer, for diabetic macular edema. *Ophthalmology*, 112(10):1747–1757, Oct 2005.

[226] Diabetic Retinopathy Clinical Research Network, M. J. Elman, L. Paul Aiello, R. W. Beck, N. M. Bressler, S. B. Bressler, A. R. Edwards, F. L. Ferris III, S. M. Friedman, A. R. Glassman, K. M. Miller, I. U. Scott, C. R. Stockdale, and J. K. Sun. Randomized trial evaluating ranibizumab plus prompt or deferred laser or triamcinolone plus prompt laser for diabetic macular edema. *Ophthalmology*, 117(6):1064–1077, Jun 2010.

[227] P. Mitchell, F. Bandello, U. Schmidt-Erfurth, G. E. Lang, P. Massin, R. O. Schlingemann, F. Sutter, C. Simader, G. Burian, O. Gerstner, and A. Weichselberger. The RESTORE study: ranibizumab monotherapy or combined with laser versus laser monotherapy for diabetic macular edema. *Ophthalmology*, 118(4):615–625, Apr 2011.

[228] Diabetic Retinopathy Clinical Research Network, M. J. Elman, N. M. Bressler, H. Qin, R. W. Beck, F. L. Ferris, S. M. Friedman, A. R. Glassman, I. U. Scott, C. R. Stockdale, and J. K. Sun. Expanded 2-year follow-up of ranibizumab plus prompt or deferred laser or triamcinolone plus prompt laser for diabetic macular edema. *Ophthalmology*, 118(4):609–614, Apr 2011.

[229] D. V. Do, U. Schmidt-Erfurth, V. H. Gonzalez, C. M. Gordon, M. Tolentino, A. J. Berliner, R. Vitti, R. Ruckert, R. Sandbrink, D. Stein, K. Yang, K. Beckmann, and J. S. Heier. The DA VINCI Study: phase 2 primary results of VEGF Trap-Eye in patients with diabetic macular edema. *Ophthalmology*, 118 (9):1819–1826, Sep 2011.

[230] M. C. Gillies, J. M. Simpson, C. Gaston, G. Hunt, H. Ali, M. Zhu, and F. Sutter. Five-year results of a randomized trial with open-label extension of triamcinolone acetonide for refractory diabetic macular edema. *Ophthalmology*, 116 (11):2182–2187, Nov 2009.

[231] A. I. Kotsolis, E. Tsianta, M. Niskopoulou, P. Masaoutis, S. Baltatzis, and I. D. Ladas. Ranibizumab for diabetic macular edema difficult to treat with focal/grid laser. *Graefes Arch Clin Exp Ophthalmol*, 248(11):1553–1557, Nov 2010.

[232] Q. D. Nguyen, S. M. Shah, A. A. Khwaja, R. Channa, E. Hatef, D. V. Do, D. Boyer, J. S. Heier, P. Abraham, A. B. Thach, E. S. Lit, B. S. Foster, E. Kruger, P. Dugel, T. Chang, A. Das, T. A. Ciulla, J. S. Pollack, J. I. Lim, D. Eliott, D. Eliot, and P. A. Campochiaro. Two-year outcomes of the ranibizumab for edema of the mAcula in diabetes (READ-2) study. *Ophthalmology*, 117(11):2146–2151, Nov 2010.

[233] P. Massin, F. Bandello, J. G. Garweg, L. L. Hansen, S. P. Harding, M. Larsen, P. Mitchell, D. Sharp, U. E. Wolf-Schnurrbusch, M. Gekkieva, A. Weichselberger, and S. Wolf. Safety and efficacy of ranibizumab in diabetic macular edema (RESOLVE Study): a 12-month, randomized, controlled, double-masked, multicenter phase II study. *Diabetes Care*, 33(11):2399–2405, Nov 2010.

[234] D. J. Browning, M. M. Altaweel, N. M. Bressler, S. B. Bressler, and I. U. Scott. Diabetic macular edema: what is focal and what is diffuse? *Am J Ophthalmol*, 146(5):649–655, Nov 2008.

[235] A. Hunter, E. K. Chin, and D. G. Telander. Macular edema in the era of spectral-domain optical coherence tomography. *Clin Ophthalmol*, 7:2085–2089, 2013.

[236] Y. M. Helmy and H. R. Atta Allah. Optical coherence tomography classification of diabetic cystoid macular edema. *Clin Ophthalmol*, 7:1731–1737, 2013.

[237] B. L. Sikorski, G. Malukiewicz, J. Stafiej, H. Lesiewska-Junk, and D. Raczynska. The diagnostic function of OCT in diabetic maculopathy. *Mediators Inflamm.*, 2013:434560, 2013.

[238] S. Sonoda, T. Sakamoto, M. Shirasawa, T. Yamashita, H. Otsuka, and H. Terasaki. Correlation between reflectivity of subretinal fluid in OCT images and concentration of intravitreal VEGF in eyes with diabetic macular edema. *Invest. Ophthalmol. Vis. Sci.*, 54(8):5367–5374, Aug 2013.

[239] D. A. Sim, P. A. Keane, S. Fung, M. Karampelas, S. R. Sadda, M. Fruttiger, P. J. Patel, A. Tufail, and C. A. Egan. Quantitative analysis of diabetic macular ischemia using optical coherence tomography. *Invest Ophthalmol Vis Sci*, 55 (1):417–423, Jan 2014.

[240] S. Ghosh, P. Bansal, H. Shejao, R. Hegde, D. Roy, and S. Biswas. Correlation of morphological pattern of optical coherence tomography in diabetic macular

edema with systemic risk factors in middle aged males. *Int Ophthalmol*, Mar 2014.

[241] Y. Huang, R. P. Danis, J. W. Pak, S. Luo, J. White, X. Zhang, A. Narkar, and A. Domalpally. Development of a semi-automatic segmentation method for retinal OCT images tested in patients with diabetic macular edema. *PLoS ONE*, 8(12):e82922, 2013.

[242] D. G. Altman and J. M. Bland. Statistics Notes: Diagnostic tests 1: sensitivity and specificity. *BMJ*, 308(6943):1552, Jun 1994.

[243] R. S. Maldonado, R. V. O'Connell, N. Sarin, S. F. Freedman, D. K. Wallace, C. M. Cotten, K. P. Winter, S. Stinnett, S. J. Chiu, J. A. Izatt, S. Farsiu, and C. A. Toth. Dynamics of human foveal development after premature birth. *Ophthalmology*, 118(12):2315–2325, Dec 2011.

[244] M. T. Cabrera, R. S. Maldonado, C. A. Toth, R. V. O'Connell, B. B. Chen, S. J. Chiu, S. Farsiu, D. K. Wallace, S. S. Stinnett, G. M. Panayotti, G. K. Swamy, and S. F. Freedman. Subfoveal fluid in healthy full-term newborns observed by handheld spectral-domain optical coherence tomography. *Am J Ophthalmol*, 153(1):167–175, Jan 2012.

[245] M. T. Cabrera, R. V. O'Connell, C. A. Toth, R. S. Maldonado, D. Tran-Viet, M. J. Allingham, S. J. Chiu, S. Farsiu, G. M. Maradiaga Panayotti, G. K. Swamy, and S. F. Freedman. Macular findings in healthy full-term Hispanic newborns observed by hand-held spectral-domain optical coherence tomography. *Ophthalmic Surg Lasers Imaging Retina*, 44(5):448–454, 2013.

[246] R. S. Maldonado, R. O'Connell, S. B. Ascher, N. Sarin, S. F. Freedman, D. K. Wallace, S. J. Chiu, S. Farsiu, M. Cotten, and C. A. Toth. Spectral-domain optical coherence tomographic assessment of severity of cystoid macular edema in retinopathy of prematurity. *Arch Ophthalmol*, 130(5):569–578, May 2012.

[247] P. Lin, P. S. Mettu, D. L. Pomerleau, S. J. Chiu, R. Maldonado, S. Stinnett, C. A. Toth, S. Farsiu, and P. Mruthyunjaya. Image inversion spectral-domain optical coherence tomography optimizes choroidal thickness and detail through improved contrast. *Invest Ophthalmol Vis Sci*, 53(4):1874–1882, Apr 2012.

[248] L. Vajzovic, A. E. Hendrickson, R. V. O'Connell, L. A. Clark, D. Tran-Viet, D. Possin, S. J. Chiu, S. Farsiu, and C. A. Toth. Maturation of the human fovea: correlation of spectral-domain optical coherence tomography findings with histology. *Am J Ophthalmol*, 154(5):779–789, Nov 2012.

[249] J. G. Christenbury, F. A. Folgar, R. V. O'Connell, S. J. Chiu, S. Farsiu, and C. A. Toth. Progression of intermediate age-related macular degeneration with

proliferation and inner retinal migration of hyperreflective foci. *Ophthalmology*, 120(5):1038–1045, May 2013.

[250] H. C. Hendargo, R. Estrada, S. J. Chiu, C. Tomasi, S. Farsiu, and J. A. Izatt. Automated non-rigid registration and mosaicing for robust imaging of distinct retinal capillary beds using speckle variance optical coherence tomography. *Biomed Opt Express*, 4(6):803–821, Jun 2013.

[251] T. A. Moreno, R. V. O'Connell, S. J. Chiu, S. Farsiu, M. T. Cabrera, R. S. Maldonado, D. Tran-Viet, S. F. Freedman, D. K. Wallace, and C. A. Toth. Choroid development and feasibility of choroidal imaging in the preterm and term infants utilizing SD-OCT. *Invest Ophthalmol Vis Sci*, 54(6):4140–4147, Jun 2013.

[252] A. N. Kuo, R. P. McNabb, S. J. Chiu, M. A. El-Dairi, S. Farsiu, C. A. Toth, and J. A. Izatt. Correction of ocular shape in retinal optical coherence tomography and effect on current clinical measures. *Am J Ophthalmol*, 156(2):304–311, Aug 2013.

[253] S. Farsiu, S. J. Chiu, R. V. O'Connell, F. A. Folgar, E. Yuan, J. A. Izatt, and C. A. Toth. Quantitative classification of eyes with and without intermediate age-related macular degeneration using optical coherence tomography. *Ophthalmology*, 121(1):162–172, Jan 2014.

[254] G. Yiu, P. Pecen, N. Sarin, S. J. Chiu, S. Farsiu, P. Mruthyunjaya, and C. A. Toth. Characterization of the choroid-scleral junction and suprachoroidal layer in healthy individuals on enhanced-depth imaging optical coherence tomography. *JAMA Ophthalmol*, 132(2):174–181, Feb 2014.

Biography

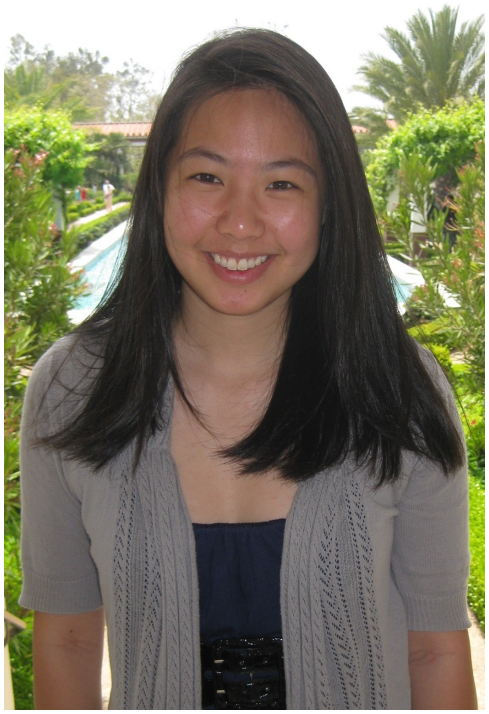

Stephanie J. Chiu was born on July 5, 1985 in Monroe, Wisconsin and grew up in Worthington, Ohio. For her undergraduate education, Stephanie majored in Biomedical Engineering at Duke University in Durham, North Carolina and received her Bachelor of Science in Engineering degree in 2007. She then worked for two years as a Software Development Engineer in Test at Microsoft Corporation in Redmond, Washington. Returning to Duke for graduate school, Stephanie was awarded the Duke Fitzpatrick Institute for Photonics John T. Chambers Scholarship in 2010 and the Duke Eye Center Residents and Fellows Day Best Research Presentation from 2010-2012. She received her Doctor of Philosophy degree in Biomedical Engineering at Duke University in 2014 after authoring 19 peer-reviewed journal papers, 3 submitted journal papers, 34 conference presentations, 3 patent applications, and 1 book chapter.

Peer-Reviewed Journal Publications

First-Author

- J.Y. Lee*, S.J. Chiu*, P.P. Srinivasan, J.A. Izatt, C.A. Toth, S. Farsiu, and G.J. Jaffe, "Fully automatic software for retinal thickness in eyes with diabetic macular edema from images acquired by Cirrus and Spectralis systems," Investigative Ophthalmology & Visual Science, vol. 54, no. 12, pp. 7595-7602, Nov. 2013. *co-first author

- S.J. Chiu, Y.V. Lokhnygina, A.M. Dubis, A. Dubra, J. Carroll, J.A. Izatt, and S. Farsiu, "Automatic cone photoreceptor segmentation using graph theory and dynamic programming," Biomedical Optics Express, vol. 4, no. 6, pp. 924-937, Jun. 2013.

- S.J. Chiu, C.A. Toth, C. Bowes Rickman, J.A. Izatt, and S. Farsiu, "Automatic segmentation of closed-contour features in ophthalmic images using graph theory and dynamic programming," Biomedical Optics Express, vol. 3, no. 5, pp. 1127-1140, Apr. 2012.

- S.J. Chiu, J.A. Izatt, R.V. OConnell, K.P. Winter, C.A. Toth, and S. Farsiu, "Validated automatic segmentation of AMD pathology including drusen and geographic atrophy in SDOCT images," Investigative Ophthalmology & Visual Science, vol. 53, no. 1, pp. 53-61, Jan. 2012.

- S.J. Chiu, X.T. Li, P. Nicholas, C.A. Toth, J.A. Izatt, and S. Farsiu, "Automatic segmentation of seven retinal layers in SDOCT images congruent with expert manual segmentation," Optics Express, vol. 18, no. 18, pp. 19413-19428, Aug. 2010.

Co-Author

- G. Li, S. Farsiu, S.J. Chiu, P. Gonzalez, E. Ltjen-Drecoll, D.R. Overby, W.D. Stamer, "Pilocarpine-induced dilation of Schlemm's canal and prevention of lumen collapse at elevated intraocular pressures in living mice," accepted to Investigative Ophthalmology & Visual Science, 2014.

- G. Yiu, P. Pecen, N. Sarin, S.J. Chiu, S. Farsiu, A. Proia, P. Mruthyunjaya, and C.A. Toth, "Characterization of the choroid-scleral junction and suprachoroidal layer in healthy subjects on enhanced-depth imaging optical coherence tomography," JAMA Ophthalmology, vol. 132, no. 2, pp. 174-181, Feb. 2014.

- S. Farsiu, S.J. Chiu, R.V. OConnell, E. Yuan, F. Folgar, J.A. Izatt, and C.A. Toth, "Quantitative classification of eyes with and without intermediate age-

related macular degeneration using optical coherence tomography," Ophthalmology, vol. 121, no. 1, pp. 162-172, Jan. 2014.

- M.T. Cabrera, C.A. Toth, R.S. Maldonado, D. Tran-Viet, M.J. Allingham, S.J. Chiu, S. Farsiu, G.M. Maradiaga Panayotti, G.K. Swamy, and S.F. Freedman, "Macular findings in healthy full term Hispanic newborns observed by handheld spectral domain optical coherence tomography," Ophthalmic Surgery, Lasers and Imaging Retina, vol. 44, no. 5, pp. 448-454, Sep. 2013.

- A.N. Kuo, R.P. McNabb, S.J. Chiu, M.A. El-Dairi, S. Farsiu, C.A. Toth, and J.A. Izatt, "Correction of ocular shape in retinal optical coherence tomography and effect on current clinical measures," American Journal of Ophthalmology, vol. 156, no. 2, pp. 304-311, Aug. 2013.

- T.A. Moreno, R.V. OConnell, S.J. Chiu, S. Farsiu, M.T. Cabrera, R.S. Maldonado, D. Tran-Viet, S.F. Freedman, D.K. Wallace, and C.A. Toth, "Choroid development and feasibility of choroidal imaging in the preterm and term infants utilizing SDOCT," Investigative Ophthalmology & Visual Science, vol. 54, no. 6, pp. 4140-4147, Jun. 2013.

- H.C. Hendargo, R. Estrada, S.J. Chiu, C. Tomasi, S. Farsiu, and J.A. Izatt, "Automated non-rigid registration and mosaicing for robust imaging of distinct retinal capillary beds using speckle variance optical coherence tomography," Biomedical Optics Express, vol. 4, no. 6, pp. 803-821, Jun. 2013.

- J.G. Christenbury, F.A. Folgar, R.V. O'Connell, S.J. Chiu, S. Farsiu, and C.A. Toth, "Progression of intermediate age-related macular degeneration with proliferation and inner retinal migration of hyperreflective foci," Ophthalmology, vol. 120, no. 5, pp. 1038-1045, Jan. 2013.

- L. Vajzovic, A. Hendrickson, R.V. OConnell, L.A. Clark, D. Tran-Viet, D. Possin, S.J. Chiu, S. Farsiu, and C.A. Toth, "Maturation of the human fovea: correlation of spectral-domain optical coherence tomography findings with histology," American Journal of Ophthalmology, vol. 154, no. 5, pp. 779-789, Nov. 2012.

- P. Lin, P.S. Mettu, D.L. Pomerleau, S.J. Chiu, R. Maldonado, S. Stinnett, C. Toth, S. Farsiu, and P. Mruthyunjaya, "Image inversion spectral-domain optical coherence tomography optimizes choroidal thickness and detail through improved contrast," Investigative Ophthalmology & Visual Science, vol. 53, no. 4, pp. 1874-1882, Mar. 2012.

- R.S. Maldonado, R. OConnell, S.B. Ascher, N. Sarin, S.F. Freedman, D.K. Wallace, S.J. Chiu, S. Farsiu, M. Cotten, and C.A. Toth, "Spectral-domain optical coherence tomographic assessment of severity of cystoid macular edema

in retinopathy of prematurity," Archives of Ophthalmology, vol. 130, no. 5, pp. 569-578, May, 2012.

- M.T. Cabrera, R.S. Maldonado, C.A. Toth, R.V. O'Connell, B. Chen, S.J. Chiu, S. Farsiu, D.K. Wallace, S.S. Stinnett, G.M. Maradiaga Panayotti, G.K. Swamy, and S.F. Freedman, "Subfoveal fluid in healthy full-term newborns observed by handheld spectral-domain optical coherence tomography," American Journal of Ophthalmology, vol. 153, no. 1, pp. 167-175.e3, Jan. 2012.

- R.S. Maldonado, R.V. OConnell, N. Sarin, S.F. Freedman, D.K. Wallace, M.C. Cotten, K.P. Winter, S.Stinnett, S.J. Chiu, J. A. Izatt, S. Farsiu, and C. A. Toth, "Dynamics of human foveal development after premature birth," American Academy of Ophthalmology, vol. 118, no. 12, pp. 2315-2325, Dec. 2011.

- F. LaRocca, S.J. Chiu, R.P. McNabb, A.N. Kuo, J.A. Izatt, and S. Farsiu, "Robust automatic segmentation of corneal layer boundaries in SDOCT images using graph theory and dynamic programming," Biomedical Optics Express, vol. 2, no. 6, pp. 1524-1538, Jun. 2011.

Conference Presentations

First-Author

- S.J. Chiu, A.M. Dubis, A. Dubra, J. Carroll, J.A. Izatt, and S. Farsiu,"Automatic segmentation of photoreceptors in AOSLO images using graph theory and dynamic programming," poster presentation at the ARVO Annual Meeting, Seattle, WA, May 2013.

- S.J. Chiu, A.M. Dubis, R.F. Cooper, A. Dubra, J. Carroll, J.A. Izatt, and S. Farsiu, "Validated automatic segmentation of photoreceptors in adaptive optics scanning ophthalmoscope images," podium presentation at the SPIE Photonics West BiOS Conference on Ophthalmic Technologies XXIII, San Francisco, CA, Feb. 2013.

- S.J. Chiu, P.S. Mettu, G.J. Jaffe, C.A. Toth, J.A. Izatt, and S. Farsiu, "Automatic segmentation of cysts in retinal SDOCT images using graph theory and dynamic programming," poster presentation at the ARVO Annual Meeting, Fort Lauderdale, FL, May 2012.

- S.J. Chiu, A. Mittal, C.B. Rickman, C.A. Toth, J.A. Izatt, and S. Farsiu, "Automatic segmentation of closed-contour features in ocular images using graph theory and dynamic programming," podium presentation at the SPIE Photonics West BiOS Conference on Ophthalmic Technologies XXII, San Francisco, CA, Jan. 2012.

- S.J. Chiu, S.G. Schuman, C.A. Toth, J.A. Izatt, and S. Farsiu, "Automated segmentation of retinal layers in SDOCT images with age-related macular degeneration pathology," poster presentation at the ARVO Annual Meeting, Fort Lauderdale, FL, May 2011.
- S.J. Chiu, J.Y. Choi, F. LaRocca, A.N. Kuo, C.A. Toth, J.A. Izatt, and S. Farsiu, "Automated segmentation of SDOCT images from multiple ophthalmic applications congruent with expert manual segmentation," podium presentation at the SPIE Photonics West BiOS Conference on Ophthalmic Technologies XXI, San Francisco, CA, Jan. 2011.
- S.J. Chiu, X.T. Li, P. Nicholas, C.A. Toth, J.A. Izatt, and S. Farsiu, "Automated segmentation of seven retinal layers in SDOCT congruent with expert manual segmentation," poster presentation at the ARVO Annual Meeting, Fort Lauderdale, FL, May 2010.

Co-Author

- D.L. Cunefare, A.V. Arshavsky, L. Fang, S.J. Chiu, C.A. Toth, A.N. Kuo, J.A. Izatt, and S. Farsiu, "Novel publically available denoising algorithm improves the performance of automated ophthalmic segmentation algorithms," podium presentation at the SPIE Photonics West BiOS Conference on Ophthalmic Technologies XXIV, San Francisco, CA, Feb. 2014.
- M.D. Twa, K. Schulle, S.J. Chiu, C.A. Toth, J.A. Izatt, S. Farsiu, and D.A. Bernsten, "Determination of macular choroidal thickness from automated and manual segmentation of optical coherence tomography imaging," presentation at the American Academy of Optometry Annual Meeting, Seattle, WA, Nov. 2013.
- G. Yiu, N. Sarin, S.J. Chiu, S. Stinnett, S. Farsiu, S. Fekrat, and C.A. Toth, "Choroidal thickness in age-related macular degeneration as measured by semi-automated segmentation of the choroid in enhanced-depth imaging optical coherence tomography," poster presentation at the ARVO Annual Meeting, Seattle, WA, May 2013.
- V. Manjunath, G. Yiu, S.J. Chiu, S. Stinnett, S. Farsiu, and T. Mahmoud, "Effect of focal laser and anti-VEGF therapy on choroidal thickness in diabetic macular edema as measured by enhanced-depth imaging optical coherence tomography," poster presentation at the ARVO Annual Meeting, Seattle, WA, May 2013.
- E.L. Yuan, F.A. Folgar, S.J. Chiu, S. Farsiu, and C.A. Toth, "One-year macular volume change of the neurosensory retina in intermediate AMD by SDOCT semi-automated segmentation," poster presentation at the ARVO Annual Meeting, Seattle, WA, May 2013.

- M. Stem, M. Hussain, M. Chan, S.J. Chiu, P. Srinivasan, J.M. Sundstrom, T.W. Gardner, S. Farsiu, R. Pop-Busui, and R. M. Shtein, "Structural changes in the retina and cornea during diabetic neuropathy," poster presentation at the ARVO Annual Meeting, Seattle, WA, May 2013.

- L. Vajzovic, A.M. Dubis, R. OConnell, T.A. Moreno, S.J. Chiu, S.F. Freedman, S. Farsiu, and C.A. Toth, "Retinal photoreceptor development and maturation in preterm and term infants," poster presentation at the ARVO Annual Meeting, Seattle, WA, May 2013.

- H.C. Hendargo, T.B. DuBose, R. Estrada, S.J. Chiu, S. Farsiu, and J.A. Izatt, "Image acquisition and processing methods for artifact-reduced imaging and differentiation of retinal capillary beds using speckle variance optical coherence tomography," podium presentation at the SPIE Photonics West BiOS Conference on OCT and Coherence Domain Optical Methods in Biomedicine XVII, San Francisco, CA, Feb. 2013.

- C.A. Toth, R.V. O'Connell, F.A. Folgar, S.J. Chiu, and S. Farsiu, "Change in Abnormal Retinal Pigment Epithelium-Drusen Complex Volume in AMD vs. Control Eyes," poster presentation at the American Academy of Ophthalmology Annual Meeting, Chicago, IL, Nov. 2012.

- A.M. Dubis, T.A. Moreno, R.V. O'Connell, S.J. Chiu, S. Farsiu, M.T. Cabrera, R.S. Maldonado, D. Tran-Viet, and C.A. Toth, "Photoreceptor and choroid development assessed with handheld SDOCT," Journal of Vision, vol. 12, no. 14, pp. 38, Dec. 2012.

- J.V. Migacz, Z. Moustafa, S.J. Chiu, T. Moreno, P. Hahn, R.V. OConnell, S. Farsiu, C.A. Toth, and J.A. Izatt. "Surgical instrument tracking image guidance for intraoperative OCT," poster presentation at the ARVO Annual Meeting, Fort Lauderdale, FL, May 2012.

- S. Farsiu, R.V. OConnell, S.J. Chiu, K.P. Winter, L.A. Clark, D. Tran-Viet, A2A SDOCT Study Group, J.A. Izatt, and C.A. Toth, "Comprehensive atlas of RPE-drusen complex thickness maps for classification of eyes with and without intermediate AMD," poster presentation at the ARVO Annual Meeting, Fort Lauderdale, FL, May 2012.

- J.Y. Lee, S. Farsiu, P. Srinivasan, S.J. Chiu, J.A. Izatt, C.A. Toth, and G.J. Jaffe, "Automatic segmentation of diabetic macular edema in spectral domain optical coherence tomography," poster presentation at the ARVO Annual Meeting, Fort Lauderdale, FL, May 2012.

- S. Schuman, R.V. OConnell, S. Farsiu, S.J. Chiu, G.B. Hubbard, W.T. Wong, T.S. Hwang, S.K. Srivastava, E.Y. Chew, and C.A. Toth, "Drusen area versus

retinal pigment epithelium-drusen complex volume in intermediate age-related macular degeneration," poster presentation at the ARVO Annual Meeting, Fort Lauderdale, FL, May 2012.

- R.V. OConnell, F.A. Folgar, J.G. Christenbury, S.J. Chiu, S. Farsiu, and C.A. Toth, "Optical coherence tomography hyperreflective foci increase in quantity and central foveal density in intermediate age-related macular degeneration," poster presentation at the ARVO Annual Meeting, Fort Lauderdale, FL, May 2012.

- L. Mutapcic, A.E. Hendrickson, L.A. Clark, R. OConnell, S.J. Chiu, S. Farsiu, and C.A. Toth, "Anatomic correlation of the spectral domain optical coherence tomography findings in human foveal development," podium presentation at the ARVO Annual Meeting, Fort Lauderdale, FL, May 2012.

- M.T. Cabrera, R.V. OConnell, C.A. Toth, R.S. Maldonado, D. Tran-Viet, J.J. Allingham, S.J. Chiu, S. Farsiu, G.M. Maradiaga Panayotti, G.K. Swamy, and S.F. Freedman, "Subfoveal fluid in healthy full term newborns observed by hand-held spectral domain optical coherence tomography," poster presentation at the AAPOS Annual Meeting, San Antonio, TX, Mar. 2012.

- J.V. Migacz, P. Hahn, R.V. O'Connell, C. Thomas, Z. Moustafa, C. Wang, S.J. Chiu, L. Dai, C.A. Toth, and J.A. Izatt, "Instrument tip-tracking ophthlamic intrasurgical SDOCT," podium presentation at the SPIE Photonics West BiOS Conference on OCT and Coherence Domain Optical Methods in Biomedicine XVI, San Francisco, CA, Jan. 2012.

- C.A. Toth, R.V. O'Connell, S.J. Chiu, S.G. Schuman, J.A. Izatt, T. Hwang, W.T. Wong, S.K. Srivastava, G.B. Hubbard, E.Y. Chew, M. Harrington, and S. Farsiu, "Semiautomated quantification of retinal pigment epitheliumdrusen complex volume from spectral domain OCT in aged adult eyes with and without intermediate AMD," poster presentation at the American Academy of Ophthalmology Annual Meeting, Orlando, FL, Nov. 2011.

- F. LaRocca, S.J. Chiu, A.N. Kuo, J.A. Izatt, and S. Farsiu, "Robust automatic segmentation of corneal layer boundaries in OCT images using graph theory and dynamic programming," poster presentation at the ARVO Annual Meeting, Fort Lauderdale, FL, May 2011.

- X. Song, R. Estrada, S.J. Chiu, A. Dhalla, C.A. Toth, J.A. Izatt, and S. Farsiu, "Segmentation-based registration of retinal optical coherence tomography images with pathology," poster presentation at the ARVO Annual Meeting, Fort Lauderdale, FL, May 2011.

- R. OConnell, R.S. Maldonado, R. Choudhary, S.J. Chiu, S.F. Freedman, D.K. Wallace, S. Farsiu, and C.A. Toth, "SDOCT characteristics of the choroid in

premature neonatal eyes differ from those in adult eyes," poster presentation at the ARVO Annual Meeting, Fort Lauderdale, FL, May 2011.

- R.S. Maldonado, M.T. Cabrera, C.A. Toth, B.B. Chen, R.V. OConnel, S.J. Chiu, S. Farsiu, D.K. Wallace, and S.F. Freedman, "Foveal morphologic characteristics in full-term neonates by spectral domain optical coherence tomography (SD OCT)," podium presentation at the ARVO Annual Meeting, Fort Lauderdale, FL, May 2011.

- X.T. Li, S.J. Chiu, P. Nicholas, C.A. Toth, J.A. Izatt, and S. Farsiu, "Segmentation of ophthalmic optical coherence tomography images using graph cuts," in Proceedings of SPIE, Vol. 7550, Ophthalmic Technologies XX, pp. 75501O, Mar. 2010.

- N. Jain, A.A. Khanifar, S. Farsiu, S. Bearelly, S.J. Chiu, K.P. Winter, J.A. Izatt, and C.A. Toth, "Qualitative comparison of segmented drusen delineated on color fundus photography," podium presentation at the ARVO Annual Meeting, Fort Lauderdale, FL, May, 2009.

- C.A. Toth, S. Farsiu, S.J. Chiu, A.A. Khanifar, and J.A. Izatt, "Automatic drusen segmentation and characterization in spectral domain optical coherence tomography (SDOCT) images of AMD eyes," podium presentation at the ARVO Annual Meeting, Fort Lauderdale, FL, May, 2008.

- S. Farsiu, S.J. Chiu, J.A. Izatt, and C.A. Toth, "Fast detection and segmentation of drusen in retinal optical coherence tomography images," in Proceedings of SPIE, Vol. 6844, Ophthalmic Technologies XVIII, pp. 68440D, Feb. 2008.

- B.A. Bower, S.J. Chiu, E. Davies, A.M. Davis, R.J. Zawadski, A.R. Fuller, D.F. Wiley, J.A. Izatt, and C.A. Toth, "Development of quantitative diagnostic observables for age-related macular degeneration using spectral domain OCT," in Proceedings of SPIE, Vol. 6426, Ophthalmic Technologies XVII, pp. 64260W, Mar. 2007.

Book Chapter

- M.D. Robinson, S.J. Chiu, C.A. Toth, J.A. Izatt, J.Y. Lo, and S. Farsiu, "New applications of super-resolution in medical imaging," in Super-Resolution Imaging, 1st ed. P. Milanfar, Ed., Boca Raton: CRC Press, 2010, ch. 13, pp. 383-412.

Patent Applications

- S. Farsiu, S.J. Chiu, and J.A. Izatt, "Segmentation and identification of closed-contour features in images using graph theory and quasi-polar transform," International Patent Application No. PCT/US14/13243, filed Jan. 27, 2014.
- J.A. Izatt, C.A. Toth, S. Farsiu, P. Hahn, Y.K. Tao, J. Ehlers, J. Migacz, and S.J. Chiu, "Imaging and visualization systems, instruments, and methods using optical coherence tomography," W.O. Patent No. 2,012,100,030, filed Jan. 19, 2012, and U.S. Patent Application No. 13/353,612, filed Jan. 19, 2012.
- S. Farsiu, S.J. Chiu, C.A. Toth, J.A. Izatt, X.T. Li, P.C. Nicholas, "Segmentation and identification of layered structures in images," U.S. Patent Application No. 13/010,448, filed Jan. 20, 2011.

Fellowships and Awards

- Best Research Presentation at the Duke Eye Center Annual Residents and Fellows Day (2010, 2011, and 2012)
- National Eye Institute Travel Grant Award (2011)
- Third Best Research Poster at the Duke Fitzpatrick Institute for Photonics Annual Meeting (2010)
- Duke Fitzpatrick Institute for Photonics John T. Chambers Scholar (2010)

Peer-Review Service

- IEEE Transactions on Image Processing
- IEEE Transactions on Medical Imaging
- Optics Express
- Medical Image Analysis
- Ophthalmic Research
- Biomedical Optics Express